An optofluidic lens biochip and an x-ray readable blood pressure microsensor: versatile tools for *in vitro* and *in vivo* diagnostics

by

Mayurachat Ning Gulari

A dissertation submitted in partial fulfillment
of the requirements for the degree of
Doctor of Philosophy
(Macromolecular Science and Engineering)
in The University of Michigan
2015

Doctoral Committee:

Associate Professor Nikolaos Chronis, Chair
Professor Katsuo Kurabayashi
Professor Edgar Meyhofer
Associate Professor James Riddell IV
Emeritus Professor Kensall D. Wise

To my mother, Jongluck Thamniyomsak

ACKNOWLEDGMENTS

I am grateful to my research advisor, Professor Nikos Chronis for guiding me through my years in grad school. His patience, understanding, and valuable advice are the reasons I can get through my PhD years. I always look to him as a perfect man who is both an artist and a scientist. An advice from him that I will never forget was "*Live the way you want to live and enjoy it to the fullest*". I would like to thank my committee, Professor James Riddell who gave me a great opportunity to be an intern at the University of Michigan Health System outpatient HIV clinic, the clinical Flow Cytometry lab and Hematology lab. I learned so much during my internship about not only the techniques of diagnosis in the hospital but also saw first hand the outstanding care he had for patients. I want to thank, Professor Katsuo Kurabayashi for his valuable advice on my research projects and as also for being my mentor for the Macro 800 lecture. I owe a debt of deep gratitude to Prof. Edgar Meyhofer. Even though, he told me that people call him "An old grumpy German" To me, he is always an exceptional teacher and a wonderful advisor. I thank him for his willingness to help and devote hours to teach and advise me. Last but not least, I also want to thank Prof. Kensall Wise, it was such a privilege to work for him for 10 years before he retired and now having him on my thesis committee. Working as process engineer in Prof. Wise's group, I worked closely with his PhD students and I got the courage and inspiration to go for my PhD degree from Prof. Wise and his PhD students. I benefited tremendously from their friendship and the knowledge we exchanged. I also want to

thank PhD students in the past years from 1996 – 2010 who worked in the Solid state or LNF cleanroom especially students who worked in Professor Kensall Wise, Khalill Najafi and Yogesh Gianchandani's group. They worked day and night with determination and goals. Each one of them inspired me to get PhD in one or another way. I want to thank my friends, Taisuke Kojima Seow Yuen Yee, Scott Zavada, Angelique Johnson, Stacey Tang, Razi-ul Haque, Christine Eun, Kyeongwoon Chung, Amar Basu, Joseph Potkay, Angelo Gaitas, Jae Yoong Cho, Tao Li, Weibin Zhu, Jay Mitchell, Naveen Gupta, Karthik Visvanathan, Venkatram Pepakayala, Siddharth Gaba, Vikram A. Thakar, Vikrant Gokhale, Mahdi Sadeghi, Seungdo An, Jun Tang, Xin Luo, Yutao Qin, Yushu Ma, Daniel Egert, Amrita Ray Chaudhury, Alex Alexandros Pantazis, Eleni Gourgou, Shinuo Weng, Xinyu Tan, Daphne Bazopoulou, Anurag Triphati, Mostafa Ghannad-Rezaie, Zeta (Tak For) Yu, Lap Man Lee, Zida Li, Xiang Li, Johanna Heureaux, Charles Chang Jiang and students in Prof. Kurabayashi's group, Prof. Lieu's group, and Prof. Fu's group for their friendship during my PhD year. My deepest thanks to Onnop Srivannavit, my friend who is always there for me. I would like to thank UM staff in ME department; Matt Navarre, Kelly Chantelois, Patty Freundl, and EECS staff; Dr. Dennis Grimard and LNF staff. I also want to thank MACRO program; Prof. Rick Laine, Prof. Richard Robertson, Nonna Hamilton and Adam Mael for their support throughout my PhD.

I want to thank my husband, Erdogan and my son, Deniz, for being so supportive and patient with me and lifting me up whenever I was down! I also want to thank my family, my father Montree Tuntayanupon, my brothers; Natthasak Tuntayanupon and Noppamongkhol Tuntayanupon, and sister Natsaran Paillard and her husband Nicolas Paillard. I love you all.

Above everything else I want to thank my mother, Jongluck Thamniyonsak, I thank you for your kindness and your hard work to bring up four children mostly by yourself. I know you

wished to see me graduate before you said your final good-bye. You are with me and I know I will see you again.

Table of Contents

List of Figures

List of tables

List of Appendices

ABSTRACT

Three different microfabricated devices were presented for use *in vivo* and *in vitro* diagnostic biomedical applications: an optofluidic-lens biochip, a hand held digital imaging system and an x-ray readable blood pressure sensor for monitoring restenosis.

An optofluidic biochip–termed the 'Microfluidic-based Oil-Immersion Lens' (mOIL) biochip were designed, fabricated and test for high-resolution imaging of various biological samples. The biochip consists of an array of high refractive index (n = 1.77) sapphire ball lenses sitting on top of an oil-filled microfluidic network of microchambers. The combination of the high optical quality lenses with the immersion oil results in a numerical aperture (NA) of 1.2 which is comparable to the high NA of oil immersion microscope objectives. The biochip can be used as an add-on-module to a stereoscope to improve the resolution from 10 microns down to 0.7 microns. It also has a scalable field of view (FOV) as the total FOV increases linearly with the number of lenses in the biochip (each lens has ~200 microns FOV).

By combining the mOIL biochip with a CMOS sensor, a LED light source in 3D printed housing, a compact (40 grams, 4cmx4cmx4cm) high resolution (~0.4 microns) hand held imaging system was developed. The applicability of this system was demonstrated by counting red and white blood cells and imaging fluorescently labelled cells. In blood smear samples, blood cells, sickle cells, and malaria-infected cells were easily identified.

To monitor restenosis, an x-ray readable implantable blood pressure sensor was developed. The sensor is based on the use of an x-ray absorbing liquid contained in a microchamber. The microchamber has a flexible membrane that is exposed to blood pressure. When the membrane deflects, the liquid moves into the microfluidic-gauge. The length of the microfluidic-gauge can be measured and consequently the applied pressure exerted on the diaphragm can be calculated. The prototype sensor has dimensions of 1x0.6x10mm and adequate resolution (19mmHg) to detect restenosis in coronary artery stents from a standard chest x-ray. Further improvements of our prototype will open up the possibility of measuring pressure drop in a coronary artery stent in a non-invasively manner.

CHAPTER 1

INTRODUCTION

1.1 Need for Point-of-Care (POC) Blood Testing

Doctors, often need to gather quantitative data by subscribing a variety of laboratory tests, most commonly blood tests, in order to make the correct diagnosis of a patient's condition and recommend the appropriate treatment. When additional laboratory tests are required, the patient may have to visit the hospital twice or more and wait several days until he/she receives the laboratory results and the necessary treatment. This process occurs routinely in the developed world. Blood tests are performed in the central laboratory of a hospital or a company such as LabCorp and can take up to one week to obtain results. Both doctors and patients have the same wish: lab tests should be fast and reliable. An ideal scenario would be to obtain the results at the first visit in the doctor's office.

In the developed world, high standards of living and longer life expectancies have led to higher levels of awareness and expectations of an individual's health. Higher expectations coupled with increased demands on individual time increases the value of fast and accurate diagnosis. The need for Point-Of-Care (POC), *in vitro* diagnostic tests for efficiency and low cost of the health care system is critical. Time and cost can be minimized if accurate diagnosis and evaluation of the patient's state of health can be made at the point of care in one visit.

Alternatively individual self-testing or self-monitoring of state of health and treatment reliably can also be a quantum leap forward in healthcare (**Figure 1.1**).

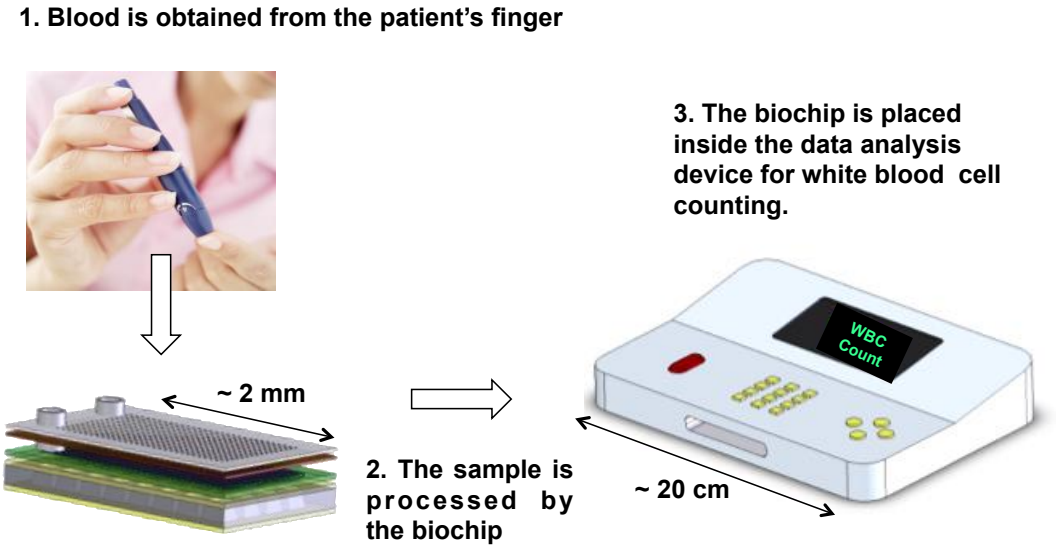

Figure 1.1: In vitro diagnostics, point of care self-testing/ self-monitoring approach using miniaturized Lab-On-Chip (LOC) systems

In the developing world diseases such as malaria, HIV, tuberculosis, tropical diseases and other infectious diseases (e.g. Ebola) are very common against a background of almost total lack of healthcare infrastructure and doctors. Patients living in low resource settings usually travel long distances by primitive means and if they are not diagnosed properly during the time they are seen by the doctor, a second visit may not be possible. Doctors who serve under these demanding conditions also have very minimal supplies and laboratory support. Thus in the low resource environments fast, low cost and accurate diagnosis is even more important than developed countries for saving lives.

Most promising solutions to some of the healthcare problems lies in combining vast amounts of cheap computing power, new microfabrication technologies for reducing instrument

size, cost and sample size, and our rapidly increasing knowledge of the biology of diseases and the functioning of human bodies at the cellular and molecular level. Computing power has followed Moore's law since 1970 which predicts that the transistor density of silicon electronics will double roughly every two years[1]. The advances in other electronic devices are also strongly related to Moore's law. The microprocessor price, the memory capacity or the number and size of pixels in digital cameras are improving at almost an exponential rate as well. A practical outcome of Moore's law is "smaller, cheaper and faster" electronics [2]. Developments in micro, and nano-fabrication technologies have made it possible to create 'smaller, cheaper and faster' electronics. Since the late 80's, MicroElectroMechanical System (MEMS) technology expanded tremendously as it adopted standard semiconductor manufacturing processes such as silicon bulk micromachining and surface micromachining[3]. Just like transistors, batch fabrication of thousands of mechanical elements has become possible (for example, cantilevered beams, springs, and mass elements). Other examples of commercialized MEMS devices include actuators, accelerometers, pressure sensors, resonators, pumps, gyroscopes and micro-optical switches [4][5][6][7][8]. Microfabrication has also been used to create non-electronic microstructures, such as microchannels, micromixers and microlenses, opening up unlimited opportunities in other applications, e.g. miniaturized Lab-On-Chip (LOC) systems –also known as micro Total Analysis Systems (μTAS).

LOC systems provide an unique technological platform to separate, synthesize, analyse and characterize minute amounts of chemical and biological specimens, while achieving equivalent or even higher performance than their larger counterparts[6]. Numerous LOC systems have been developed to perform sample handling steps in an integrated process some examples of which are separation and analysis with micro gas chromatography [7] and

electrophoresis[8], DNA sequencing from parallel synthesis on microchips[9], insulin and glucose sensing[10], HIV viral load testing [11], LOC applications for cell analysis[12] and more recently whole organism studies of *C elegans* [13].

In point-of–care (POC) applications, clinical diagnostic devices need to perform rapid analyses, be less labor intensive, work with very small samples, and operate without the help of trained healthcare personnel [14][15]. These requirements favor microdevices over bench-top equipment tests in centralized laboratories. Same capabilities also make microdevices desirable in cases where providing timely care to patients is critical, for instance in the emergency room, in the battlefield or in low resource environments. An example of a POC device for rapid blood analysis can make a very significant difference under these conditions.

Blood is the most important biological fluid that contains evidence of all the diseases the individual has and therefore is used for diagnosis. Blood supplies oxygen and nutrition to every organ every twenty seconds and takes away waste from them. The ability to analyse the chemistry of blood, determine the presence of pathogens present in blood and count number/concentration of the different types of cells present in blood provide a wealth of information about the patients state of health. From the proteins present one can detect metabolic syndrome, coronary artery disease, diabetes and inflammatory disorders that are the cause of heart disease or stroke[16]. Detection of rare circulating cells if possible can be used to find out about cancers that are not yet advanced enough to be physically detectable. Analysis of free circulating DNA can be used to detect the presence of bacteria, viruses, cancer and even sex of the unborn child[17].

Blood analysis, has two important components: blood preparation and detection. Depending on the application, blood preparation procedures involve cell lysing, cell separation, sorting, extraction of DNA, DNA amplification, etc.

While there have been many demonstrations of micro systems that can do complex biological and chemical manipulations of samples within a single microfluidic chip, in practice these on-chip systems cannot be operated without the support of bulky and expensive external components such as pumps, compressed air and external switches to actuate fluid and most of the time need bulky external optical microscopes and detectors [18][19][20][21]. In the laboratory setting, various types of optical microscopy techniques such as fluorescence microscopy, bright-field microscopy, and confocal microscopy are commonly used for cellular imaging. These microscopes provide high-resolution imaging enabled by the high numerical aperture (NA) of their objective lenses. In general high NA objective lenses have small fields of view (FOV) around ~ 100-1000 μm.

The detection methods used for measuring the number of specific cells of interest include electrical (e.g. capacitive, impedance), mass spectroscopy, optical imaging (e.g. conventional microscopy, holography, scanning-based, shadow, etc.). Optical detection has the advantage that it is a direct method and one can store the images if necessary for later analysis as opposed to an indirect method such as measuring capacitance of the cells passing between two electrodes. Optical detection with lenses puts a premium on the quality of the image obtained which is usually expressed in terms of its numerical aperture (NA). In addition to high NA lenses high sensitivity and resolution image recording devices such as CMOS&CCD sensors, photomultiplier tubes are the other important components of a good optical detection system.

Since the 1980s, a number of microfabricated microlens arrays have been developed [22]. Up until now, the best NAs reported in the literature for microlens arrays is 0.41[23] and ~ 0.5[24] in 2012. Typically, the microlens arrays or individual microlens sytems reported in the literature were part of a larger assembly containing dichroic mirrors, filters, relay optics, high quality collimated illuminating light sources and the systems were built on top of large optical tables. So far, no microfabricated microlens array has demonstrated high resolution imaging as a simple standalone point of care device. Our goal on this thesis was to develop an easy to use, optical imaging system with high NA and afterward move the optical setting from the large laboratory optical imaging bench to POC devices for use in in-vitro diagnostics (**Figure 1.2**).

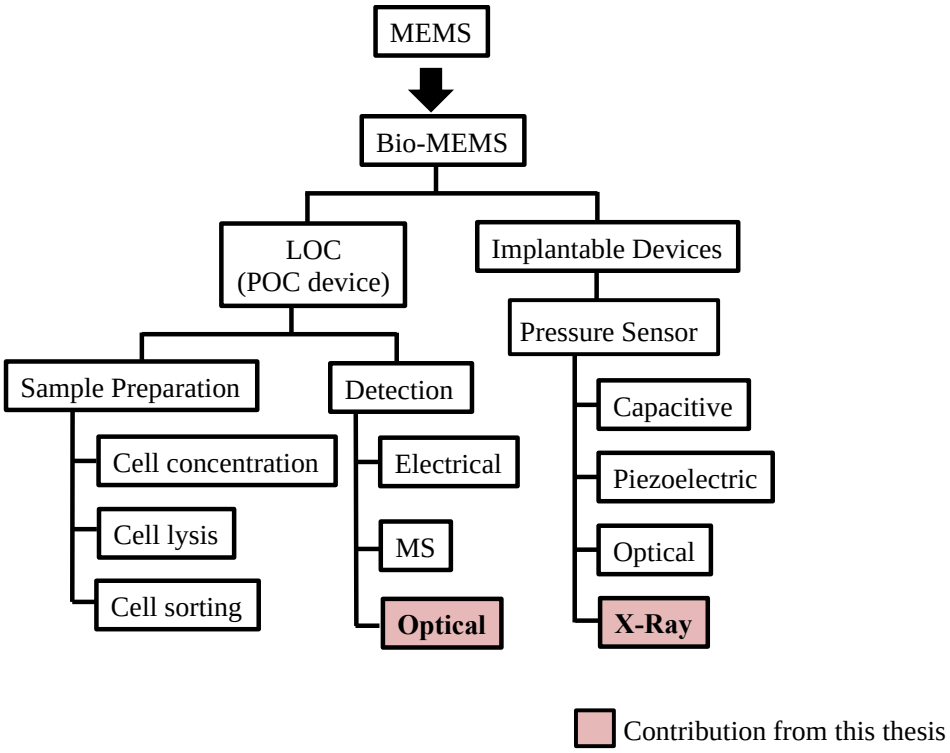

Figure 1.2: Two microfabricated devices that were developed during this thesis work; one is the optical imaging device for POC in-vitro diagnostics and another is an X-ray detectable pressure sensor.

1.2 Need for Implantable Pressure Sensors

The value of pressure in various organs (e.g. brain, eye, bladder, different arteries) is a demonstration of a patient's health and progression of disease. When the ability to regulate the pressure is lost, damage to the organ and death can occur.

Blood pressure is an especially important parameter linked to an individual's state of health. Currently the standard technique of measuring blood pressure with an arm cuff gives only the overall blood pressure and does not give information about specific areas. Because blood pressure changes due to physical activity, sleep, stress etc., establishment of a baseline level and observation of short-term spikes in blood pressure are not straightforward. Several

other noninvasive methods such as ultrasonic or electromagnetic radiation have been explored extensively; however, they do not provide accurate readout or pinpoint the specific region of the body[25]. At the present, accurate pressure monitoring at a specific location in a blood vessel is done by inserting a catheter with a pressure sensor wire. However, this invasive method is not suitable for long-term monitoring. A fully implantable pressure sensor which is small enough not to disturb the flow and biocompatible can eliminate repeated invasive measurements and risk of infection from catheters or wires as well as be used to monitor progression of treatment.

Fully implantable devices for long-term pressure monitoring must be small in size and weight, biocompatible and implanted with minimally invasive surgery. In addition they have to be aseptically fabricated, hermetically sealed, and have low power consumption for reliable long-term in *vivo* applications [26][27]. A number of different BioMEMS pressure sensors have been developed for monitoring different organs such as arterial or venous blood pressure[28][29][30][31], pulmonary artery blood pressure [32], intraocular pressure [33][34][35], intracranial pressure [27][36] and hydrocephalus actuation[37].

One very challenging area of interest in monitoring changes in blood pressure is in detection of stent restenosis in Coronary Artery Disease (CAD) patients fitted with stents. CAD disease effects 15.8 million people worldwide [38]. Blood flow through the arteries decreases due to narrowing of the arteries by deposition of plaque under the epithelial layer of the inner wall of arteries. Plaque deposits form in areas of turbulence and their deposition rate may accelerate with time. Thus, the heart has to work harder and pump at a higher pressure to maintain the required flow rate, which can in turn cause thrombosis in the arteries as well as enlargement of the heart. Plaque deposition in coronary arteries is a life-threatening problem because not enough blood flow to the heart muscles causes muscle tissue death, weakening the

heart in its ability to circulate blood to the rest of the body. Unfortunately the symptoms of blockage of the coronary arteries are not very obvious externally until there is a significant reduction in blood flow[39].

Originally inflatable balloons were used to open up the plugged locations. Later wire stents were developed and are inserted into the coronary arteries as a means of keeping the arteries open to deliver blood to the heart muscles (**Figure 1.3**) However, frequently restenosis occurs after the insertion of the stent. Restenosis is a problem with both bare metal stents and with drug-eluting stents[40]. This problem requires frequent monitoring of the state of restenosis. Current means of measuring the extent of restenosis is an invasive measurement of the pressure drop across the stent by inserting a pressure sensing thin wire through a fluid-filled catheter inserted either from the arm or the groin. However, even this invasive method suffers from shortcomings such as errors introduced by mechanical disturbances, turbulence due to the catheter and resonance effects [30].

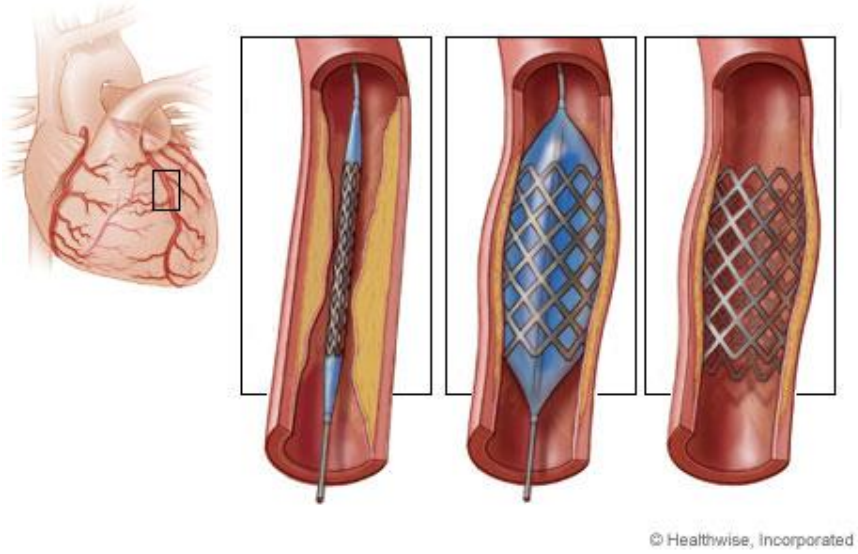

Figure 1.3: A stent: small expandable tube that insert into coronary artery and expanded by a small balloon during the angioplasty procedure [Taken from[41]]

In patients with chest pain, re-stenosis of moderate severity assessed by coronary angiography, evaluation and treatment is a challenge[42]. To date no implantable device has been made for measuring coronary arterial blood pressure. The main limitation is the size of the coronary arteries. The ventricles have a lumen of 4-6 cm, whereas coronary arteries have diameters of 2-4mm maximum. At the present, the two smallest pressure sensors commercially available are the CardioMEMS EndoSensor^{TM} ~5mmx30 mm [43][44] and the ISSYS sensor ~3mmx15mm[45] . These sensors monitor Abdominal Aortic Aneurysm graft pressures (AAA) and Congestive Heart Failure (CHF), respectively. Their typical footprint makes integration of such large devices impossible with coronary artery stents.

The simplest and most accurate means of measuring increase in plaque deposition through the stent is to determine the pressure drop across the stent.

The ideal pressure sensor for monitoring the state of coronary restenosis is [46] :

- sensitive to detect pressure drops on the order of 20 mmHg
- much smaller than the stent and the coronary arteries itself so as not to obstruct blood flow (max diameter~ 0.5mm)
- biocompatible,
- on the stent itself
- able to measure pressure passively
- able to be read non-invasively

Our second project in this thesis was to develop a proof-of-concept Bio-MEMS implantable pressure sensor for coronary artery stents that can be read in a novel way using simple chest x-ray imaging **(Figure 1.2)**.

1.3 Current Practices

1.3.1 Cell counting and Identification for In vitro Diagnostics

Flow cytometry (FC) is the current gold standard for in-vitro counting of the types of cells present in high concentrations in blood [47]. For example progression of treatment for HIV/AIDS is determined by the CD4 T lymphocyte counts [48][49]. FC provides an accurate and high-throughput automated measurement of cell populations at rates of up to 10,000 cells per second[50]. The FC principle of operation is based on measuring scattering by cells that are registered to a counter while flowing one by one through the focal point of imaging optics in single file in a stream of fluid (**Figure 1.4)**. The interaction of the laser lights with the cells leads to forward angle light scattering, the intensity of which is a measure of size. While FC is simple it can only differentiate between cells based on size. Different types of cells with the same refractive index difference with the carrier fluid will give similar signals. A specialized FC known as Fluorescence Activated Cell Sorting (FACS) is used for analyzing cell populations, counting and sorting cells of interest into two or more containers based on the fluorescent characteristics and the specific light scattering of each cell[51][52]. In this approach, antibodies conjugated to a fluorescent dye are used to bind to specific proteins on the cell membrane. When the labeled cells are passing through the light source of the correct excitation wavelength the dye is excited and gives off fluorescent light at a lower specific frequency and the presence of the cell of interest is detected. By using multiple fluorescent dyes, with similar excitation wavelengths (or multiple excitation wavelengths) but emissions at different wavelengths,

multiple types of cells or multiple properties of the same cell can be measured simultaneously[53]. Unfortunately, FACS instruments are expensive ($30,000 - $150,000), bulky, require filtered water, reasonable amount of electrical power, costly refrigerated reagents, and experienced technicians for operation and data analysis. Even for a single-purpose FACS instrument, the cost, electrical consumption and other operational requirements are similar to standard FACS. As a result, FACS systems are used only in centralized laboratories and in hospitals. Small health clinics in resource-limited settings typically cannot afford it. The cost limitation brings about a pressing need for a low cost instrument for resource limited settings. A portable low-cost POC device with low power requirements, needing minimal supplies and usable with no or minimal training is desirable/ideal for both resource-limited as well as resource-rich settings.

A few examples of other state of the art technologies for cell preparation, separation or sorting which could potentially be used for in-vitro diagnostic POC applications are 1) the Isoraft System which isolates rare cells in a viable manner for later growth and analysis[54], 2) the Silicon Biosystem which manipulates cells with dielectrophoresis in a varying electric field to sort cells according to their electrical properties[55], 3) Miltenyi biotech magnetic beads [56] and the Dynabeads cell sorting system in which magnetic microbeads functionalized with specific antibodies capture individual cells by binding to membrane proteins of cells of interest.

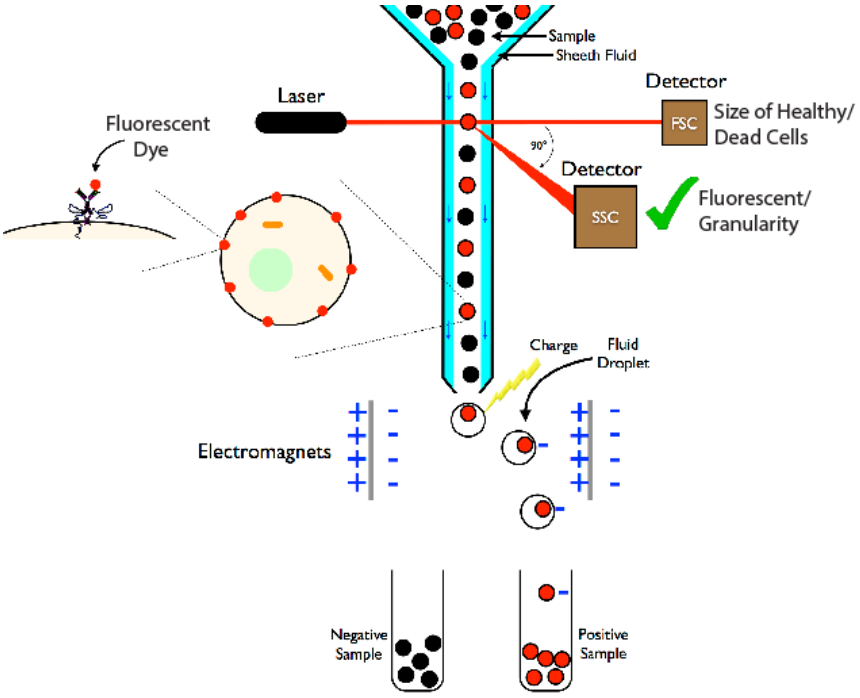

Figure 1.4: Mechanism of Fluorescence-Activated Cell Sorter (FACS) for counting and sorting cells. [adapted from [52]]

1.3.2 Monitoring in-stent restenosis through the Fractional Flow Reserve

The gold standard to detect coronary artery stenosis and in-stent restenosis is angiography and Fractional Flow Reserve (FFR). In angiography, the catheter (a thin hollow tube) is passed through an artery and moved up to the heart. X-ray images are taken to assist the positioning of the catheter. Once the catheter is in place, a radio-opaque contrast agent is injected directly into the coronary artery. By observing the X-ray images of the contrast agent in the artery, cardiologists can identify the stenosis position. When the stenosis is severe, percutaneous coronary intervention (PCI) is performed to open blocked coronary arteries so that arterial blood flow can be restored to the heart. Beyond percutaneous balloon angioplasty, coronary stents are now universally used in PCI procedures. The stent forces the narrow or blocked artery opens and physically keeps the artery from closing again.

Angiography accurately identifies the two extreme cases of stenosis: high degree stenosis and patent vessels. However, a large number of stenoses are intermediate grade, and their effect on myocardial perfusion cannot be assessed visually.

To address this shortcoming, cardiologists developed the Fractional Flow Reserve (FFR) system. The FFR is the ratio of the perfusion pressure after (distal, Pa) and before (Pa) a stenosis, measured during coronary angiography (FFR = Pa/Pb) **(Figure 1.5)**[57]. A minimally invasive surgery is performed to obtain FFR by passing a thin wire with a pressure transducer to measure the pressure at the proximal and distal ends of the stent. FFR-guided procedures with a threshold of FFR ≤0.75 or pressure drop of 25% or more, have reduced the rate of death, nonfatal myocardial infarction, and repeat revascularization[58]. FFR- guided stenting and optimal medical therapy has been found to be superior to best medical therapy alone and decreased the need for urgent repeat revascularization[40]. However, angiography is an invasive procedure with associated risk and costs approximately $13k per procedure[59].

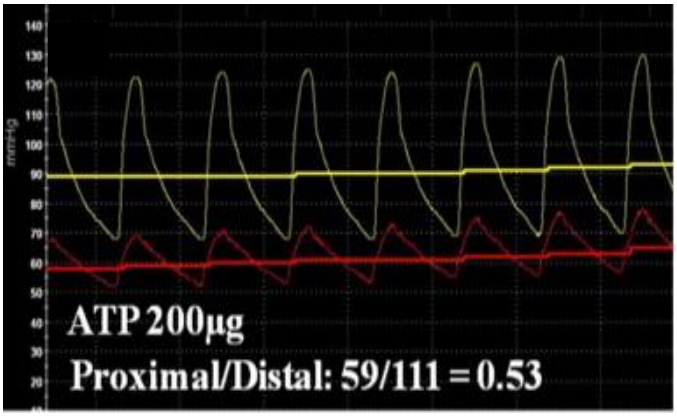

Figure 1.5: Plot of systolic and diastolic blood pressure vs time. Simultaneous pressure recordings during FFR monitoring by hyperemia induced with intra-arterial administration of 200µg of ATP. Yellow based line: pressure measured proximal to the stenosis. Red based line: pressure measured distal to the stenosis. FFR = 0.53 [Taken from [57]]

1.4 Thesis Objectives

This thesis has two main objectives:

1.4.1. Develop a Point-of-Care platform for high-resolution cell imaging and counting**.**

1.4.2. Develop a new class of X-Ray detectable pressure sensor.

1.5 Thesis Organization

The research work presented in this thesis has been organized in five chapters:

Chapter 2 – Literature Review

This chapter reviews various optical imaging methods used for POC and current implantable pressure sensor devices. The optical imaging methods are divided into two groups: lensless-imaging and lens-based microscopy. The lensless imaging methods are developed without any optical components to reduce the optical path and therefore can be very compact. Most of these methods obtain images by capturing diffraction pattern of an object on a CMOS sensor and use software algorithms to invert the information. The lens-based imaging methods are the typical techniques to acquire high-resolution images instantaneously. There are a few technologies that utilize off the shelf optical components for POC. Other chip-scale optical imaging methods (tunable and fixed microlens) are also briefly reviewed.

Chapter 3 – An Optofluidics Lens Array Microchip for High Resolution Stereo Microscopy

This chapter presents a simple-to-use, reusable and compact, micromachined module for imaging applications. This module – a Microfluidic-based Oil-Immersion Lens (μOIL) chip array can be used as an add-on module to transform any stereo microscope into a high resolution imaging system by simply putting the module on top of the sample. The μOIL chip consists of an

array of ball mini-lenses of excellent optical quality that are microfluidically connected and half immersed in oil.

Chapter 4 – A digital handheld optofluidic microscope for point of care diagnostics

This chapter presents a bright field and fluorescent imaging device that can be used as a generic platform for cell counting or visual disease diagnosis. It is a compact, lightweight and low cost instrument. The device consists of a μOIL array, a CMOS sensor and a LED light source. Adding excitation, emission filters and a condenser lens transforms the bright field setup to a fluorescence-mode μOIL microscope. The use of the μOIL imaging device is demonstrated by imaging and counting red blood cells (RBC) and human leukemic monocyte THP-1 cells in brightfield and stained THP-1 cells in fluorescent mode. The μOIL imaging device's resolution is 0.43μm and weighs less than 40 grams.

Chapter 5 – An implantable, X-Ray Based Blood Pressure Microsensor for Coronary In-Stent Restenosis Surveillance and Prevention

In this chapter, we demonstrate an X-ray addressable Blood Pressure (X-BP) microsensor. The X-BP has a column of radio-opaque liquid that changes its length with blood pressure. The X-BP allows for the non-invasive evaluation of the pressure drop across a stent and the fractional flow reserve (FFR) on radiographs. It can be used for periodic screening of coronary in-stent restenosis. The X-BP membrane was modelled and the x-ray Signal-to-Noise ratio (SNR) of different sensor dimensions was experimentally determined. The sensor was prototyped and tested under microscope and with radiographs. The sensor has a potential dynamic range of 0-200 mmHg and can reliably resolve the clinically important pressure drop of 20-25% across the dynamic range for an FFR value of 0.8 to 0.75 or less.

Chapter 6 – Conclusions and Future work

This chapter summarizes the work demonstrated in this thesis and presents future directions.

CHAPTER 2

LITERATURE REVIEW

The first part of this chapter presents various chip-scale microscopy technologies that have been used for cell counting, imaging or cell identification. They are compact, inexpensive and important lab-on-a-chip components for point-of-care medical systems. The second part of this chapter reviews various commercial and in-development implantable pressure sensor devices.

2.1 State of the art optical imaging technologies for in vitro diagnostics

Despite the improvement in accuracy and high-throughput, FACS still requires a complex and expensive set-up which limits their use beyond well-equipped laboratories. In the developing world, diagnostic technologies should meet the specifications set by World Health Organization for accessibility, specificity, ease to use, affordability, speed and robustness [60]. Researchers use microfacrication and/or microfluidic techniques to make very small, compact, mass-producible, low power, rapid analysis, high sensitivity medical diagnostic devices at low cost [61]. Some of the devices which are in the research stage today can potentially make a significant contribution in monitoring pathological conditions in the developed world as well as in resource-limited settings [62]. Research efforts towards low cost, compact imaging systems have been focused on utilizing microlenses [7–10] and microlens arrays [11–26] optofluidic microscope [27-28] or even tomographic imaging methods [29-30]. Significant amount of

research and development in the area of lab-on-a-chip scale imaging for diagnostics and POC systems has taken place in the past decade. These imaging devices can be divided into lensless and lens-based categories.

2.1.1 Lensless-Based Imaging

The lensless imaging systems are developed without imaging optical components so that optical path length is reduced to a minimum and the system becomes highly compact. There are three prominent lensless imaging techniques we will review.

2.1.1.1 Shadow Contact Imaging

An earlier application of this approach aimed to investigate the genetics, development, behavior and aging of the living organism (*Caenorhabditis elegans*) on a spaceflight[85]. The *C.elegans* in liquid media was placed on top of the CMOS video camera chip which was attached to the bottom of the sample chamber. When the sample chamber was illuminated by a LED light source from above (**Figure 2.1A**), the shadow of *C.elegans* was directly on a CMOS sensor with a resolution of 320 x 240 pixels. This research showed that the image resolution obtained in this manner was sufficient to identify and track the behavior of individual worms **Figure 2.1 B**).

Lensless shadow imaging techniques utilize spatially incoherent light, the number of cells in the sample was obtained simply by counting the diffraction pattern of each cell. Demirci *et al* [86][87][88] demonstrated this techniques called it "LUCAS"; a **L**ensless, **U**ltra wide-field **C**ell monitoring **A**rray platform based on **S**hadow imaging. They used LUCAS to image captured CD4+ T-lymphocytes for HIV point-of-care testing (**Figure 2.2(A)**). They made a microfluidic chip that was placed directly on a CCD imaging platform. When the light source is set up very far from the sample (~ 40 cm), the point white light source can be assumed to behave

like a planar light source. The white light emitted by a halogen lamp goes through a light guide reaching the captured cells. Shadows of the captured cells then are imaged by the CCD sensor. To capture $CD4^+$ cells they immobilized an anti-CD4+ antibody on the surface of their microfluidic chamber. Blood samples were flowed in by a syringe pump at the rate of 5μl/min for 2 minutes. CD4+ T-lymphocytes in blood were captured on the surface of microfluidic chip and imaged (**Figure 2.2(B)**).

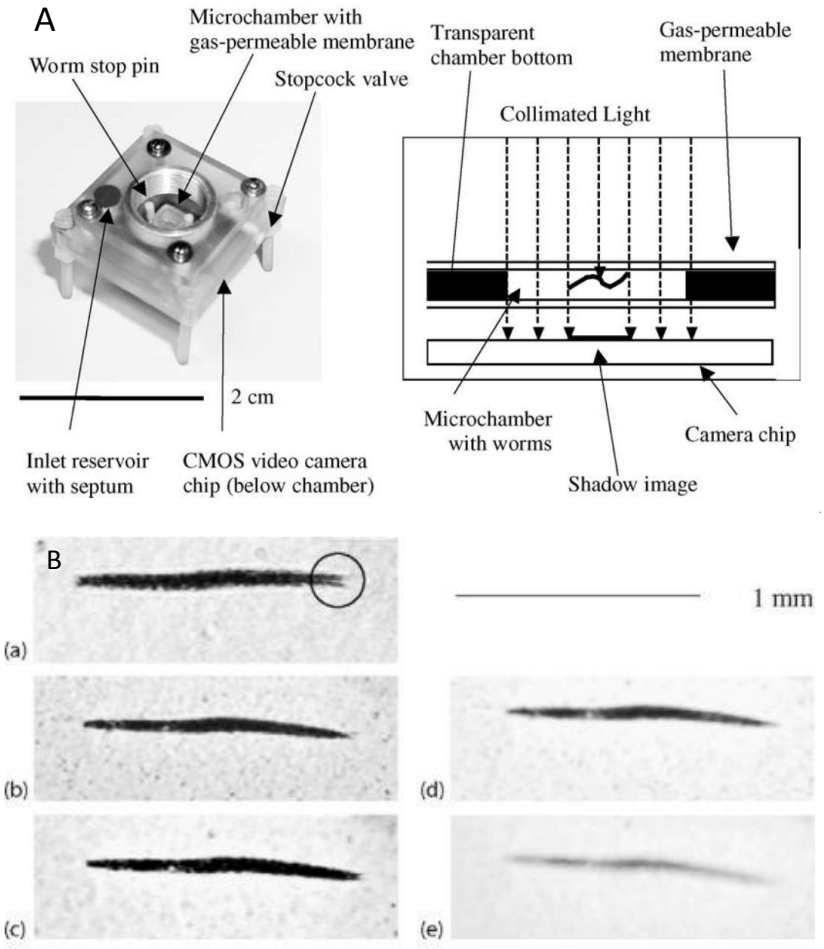

Figure 2.1: (A) Photograph and schematic diagram of the worm imager. Nematodes in a 500μm high microchamber are illuminated with an LED and cast a shadow onto a CMOS video camera chip attached at the bottom of the chamber. **(B)** Improvement of shadow image quality: (a) illumination with an infrared point source LED results in a split tail artifact (see circle) due to diffraction at the worm body (wavelength, 880 nm; LED distance, 23mm; video chip distance, 1 mm); (b) reduction of artifacts by decreasing the video chip distance to 0.3mm; (c) image quality

is still sufficient for LED distance reduced to 10mm; (d) reduction of image artifacts by illumination at 470nm (LED distance, 23mm; video chip distance, 0.3 mm); (e) further reduction of LED distance to 10.5mm introduces some blurring as the blue LED does not have point source characteristics. [Adapted from[85]]

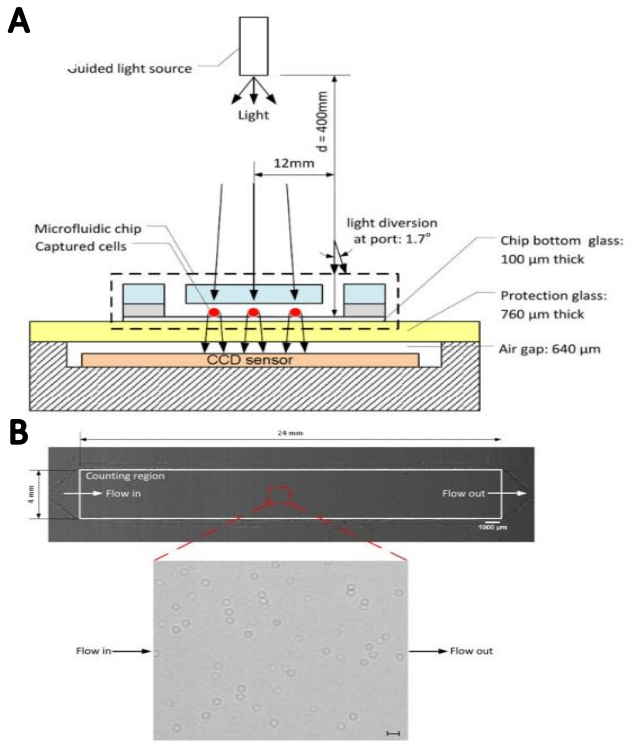

Figure 2.2: **(A)** Figure 1. A schematic view of the CCD imaging platform: (a) CCD imaging platform to detect the captured cells. When light is incident on the captured cells, cells diffract and transmit light. Shadows of the captured CD4+ T-lymphocytes generated by diffraction can be imaged by the CCD in one second. Image is obtained with the lensless CCD imaging platform. **(B)** Image taken with the lens-less CCD imaging platform and the shadow image of the cell in the microfluidic channel is shown. The image is obtained by diffraction. Scale bar, 100 µm. [Adapted from[86]]

In shadow/diffraction imaging technique, proper illumination plays a critical role in image quality obtained from the sample. Without the presence of optical components, a sufficient collimation of the light source is needed to create a sharp image on the sensor chip and

minimize blur. The distance between the image sensor and the sample also needs to be minimized to less than 1 μm (ideally) to reduce diffraction artifacts that compromise spatial resolution and image quality[89]. As a result, the microlens array and color filters on the sensor-chips have to be removed before placing the sample on top of the imaging sensor. The pixel size of the image sensor also affects the performance of the image quality (resolution). To increase image resolution and solve under-sampling effect, Yang group [90][81][91][92] demonstrated an optofluidics microscope (OFM) with mobilizes the sample (by flow or gravity) along the microfluidic channel. They patterned a thin film metallic aperture array directly on the CMOS sensor. Each aperture was aligned at the center of the pixel and therefore the shadow images of the sample was captured while flowing across the pinhole aperture **(Figure 2.3(A))**. Later, low resolution sequence of sample images were combined to construct a high resolution image with a resolution enhancement factor as high as 10. However, for this system to work properly the sample has to move along the imaging channel with a constant velocity. An example of imaging *C. elegans* is demonstrated in **Figure 2.3(B)**.

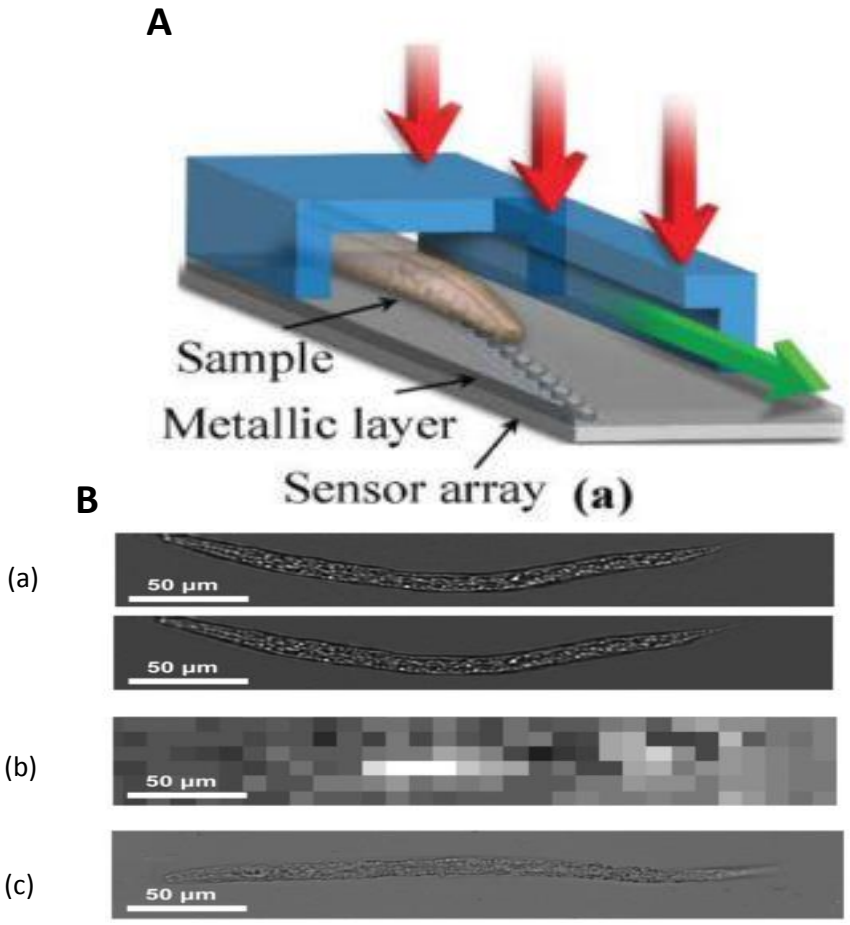

Figure 2.3: A) A schematic diagram of OFM. Green arrow shows flow direction, red arrows show illumination the apertures (white circles) are fabricated directly on top of the optoelectronic sensor and incorporated in an optofluidic channel (blue lines). **B)** Images of wild-type *C. elegans* L1 larvae. (a) Duplicate OFM images acquired by the two OFM arrays for the same *C. elegans*.(b) Direct projection image on a 9.9-µmpixel size CMOS sensor. (c) Conventional microscope image acquired with a 20x objective. [Adapted from[92]]

2.1.1.2 Lensless Holographic Imaging

In-line holography was invented by Gabor [93] in 1948. In his original setup, the sample is placed between a coherent light source and a photographic plate. The incident light is scattered by the sample and interferes with the undisturbed light forming a constructive and destructive interference pattern. The imaging process contains two steps: 1) record the interference pattern on the photographic plate such as the hologram. 2) reconstruct the object image with another light source.

Digital in-line holography (DILH) has regained the popularity due to the advances in CCD sensor technology. By adding a pinhole into the system, this technique can use a phase-contrast imaging to give both qualitative and quantitative information. In the set-up, the samples are illuminated with a spherical wavefront produced by focusing light or laser beam from a small (e.g. 1-μm) diameter pinhole. The focused light serves as a reference beam and the scattered light serves as the object beam. The CCD sensor array records the interference pattern produced by the superposition of the two wavefronts (the hologram). To obtain the image, the diffraction patterns produced is decoded with two major types of algorithms; interferometric and non-interferometric phase retrieval techniques[94]. A subsequent digital elaboration allows retrieving the volume information on the sample from a single 2D hologram. In this method, multiple focal planes can be achieved and captured mimicking the focus control of conventional optical microscopes. Ozcan *et al* [95][96][97][98][99] has been using this technique to demonstrate cell counting with a mobile phone camera.

One advantage of using holographic method is the intensity and phase information of the sample can be stored and then reconstructed simultaneously. However, using another light source

for reconstruction prevents real-time imaging. The disadvantage of DIHL is that it requires high precision alignment of the laser beam through ~1 μm diameter pinhole. Small particles or dust can easily block the pinhole preventing illumination by the laser. In line holography can not be used for fluorescent imaging.

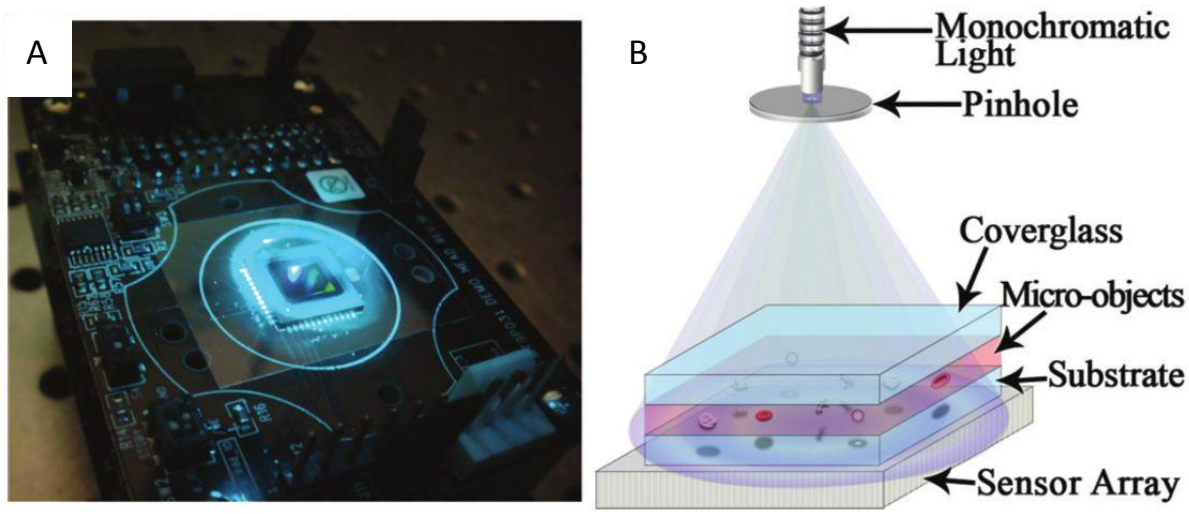

Figure 2.4: (A) Experiment apparatus under blue light illumination. **(B)** schematic diagram of the Holographic-LUCAS platform. [Adapted from[95]]

2.1.2 Lens-Based Imaging

2.1.2.1 Traditional Lens imaging

Traditional lens based imaging devices adapted microscope objective lenses or miniaturized optical lenses for obtaining imaging samples. Compound lens-based microscopes are bulky and have a relatively high cost, however they offere superior imaging quality compared to any of the lens-less techniques. Over the past several years, researchers have been working on reducing the size of lens-based microscopy, making it compact and suitable for specific tasks. In one example demonstrated in 2009 by Breslauer *et al* [100], critical optical components of a microscope were rearranged in a new configuration to fit to a mobile phone, making it suitable as a point-of-care device. The compact microscopy was operated in brightfield and fluorescence modes. The system was composed of a 20X wide field microscope eyepiece, a 0.85 NA 60 X and an Achromat objective (**Figure 2.5**). The setup showed ~180 μm diameter FOV and a magnification onto the camera at ~ 28X. The spatial resolution was estimated to be ~1.2μm.

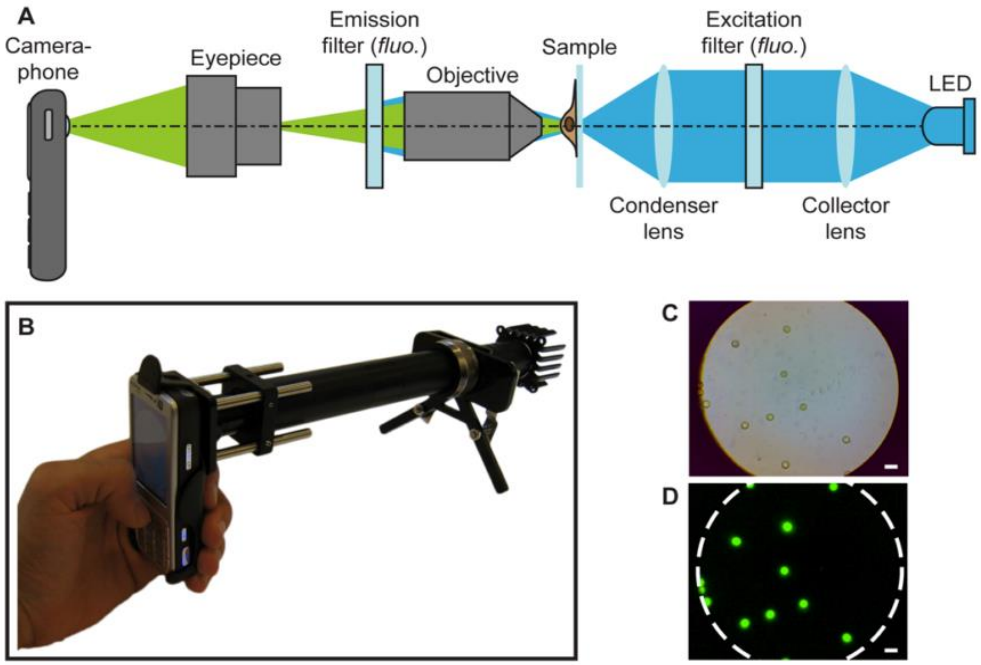

Figure 2.5: (A) Layout schematic of mobile phone microscope for fluorescence imaging. **(B)** prototype with filter and LED installed. The objective is in the optical tubing and the specimen is mounted near the metallic focusing knob. **(C)** Brightfield image of 6μm fluorescent beads **(D)** Fluorescent images of beads. Taken from [100]

In 2011, Schnitzer's group miniaturized each optical component such that they can be very compact, lightweight (1.9 gram), suitable to imaging a mice's brain. The miniaturized integrated fluorescence microscope was built based on mass-producible components (including simple LEDs and CMOS sensor) giving field of view (FOV) of 600 μm x 800 μm at 5X magnification (**Figure 2.6**) [101][102]. This microscope was capable of imaging and tracking of Ca^{2+} spiking in >200 Purkinje neurons across nine cerebellar microzones in the area across ~0.5 mm^2 of active mice's brain.

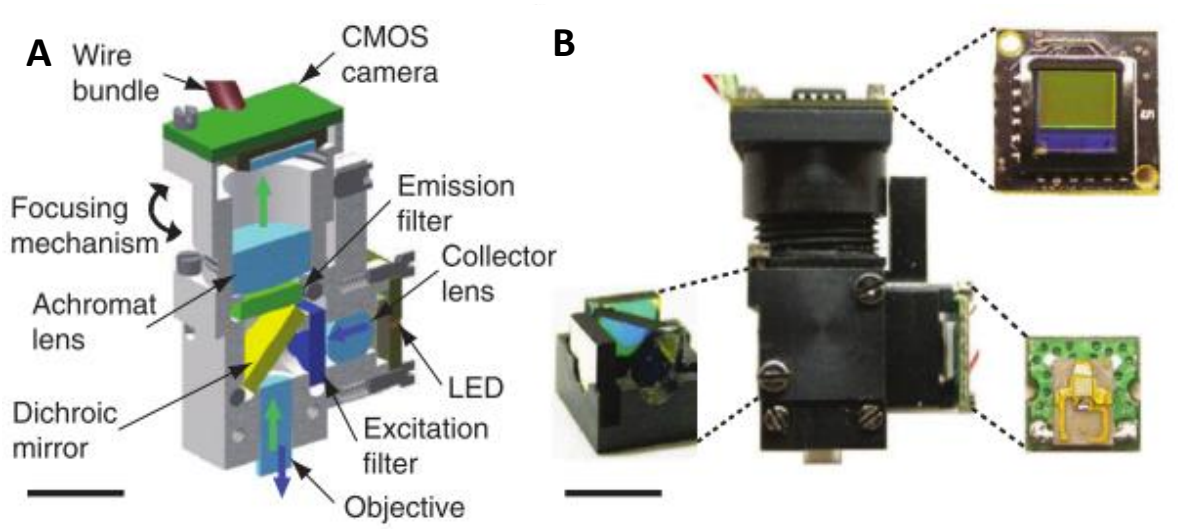

Figure 2.6: **(A)** Shown in cross-section, computer-assisted design of an integrated microscope,. Blue and green arrows mark illumination and emission pathways, respectively. **(B)** Image of an assembled integrated microscope. Insets, filter cube holding dichroic mirror and excitation and emission filters (bottom left), PCB holding the CMOS camera chip (top right) and PCB holding the LED illumination source (bottom right). The wire bundles for LED and CMOS boards are visible. Scale bars, 5 mm (a,b). Taken from [101]

Ozcan *et al.* [103][104] also demonstrated the use of a cell-phone for fluorescent imaging and sensing platform with an external lens for cell counting, detection of *E. coli*, several other applications. In one demonstration they used a Samsung Galaxy SII with a built-in lens which has a focal length of ~4mm. To increase the field of view to 0.2-1 cm^2 they added an extra lens with a focal length of 15 and reduced the magnification to 3.75. Using 2 of AA batteries, they demonstrated a compact imaging cytometry platform installed on a cell-phone for the measurement of concentration of red and white blood cells as well as hemoglobin concentration[105] (**Figure 2.7**). They also used the same set up to image fluorescently labelled

WBCs in diluted whole blood. During sample preparation, the sample is labelled with a quantum dot to increase the fluorescence signal.

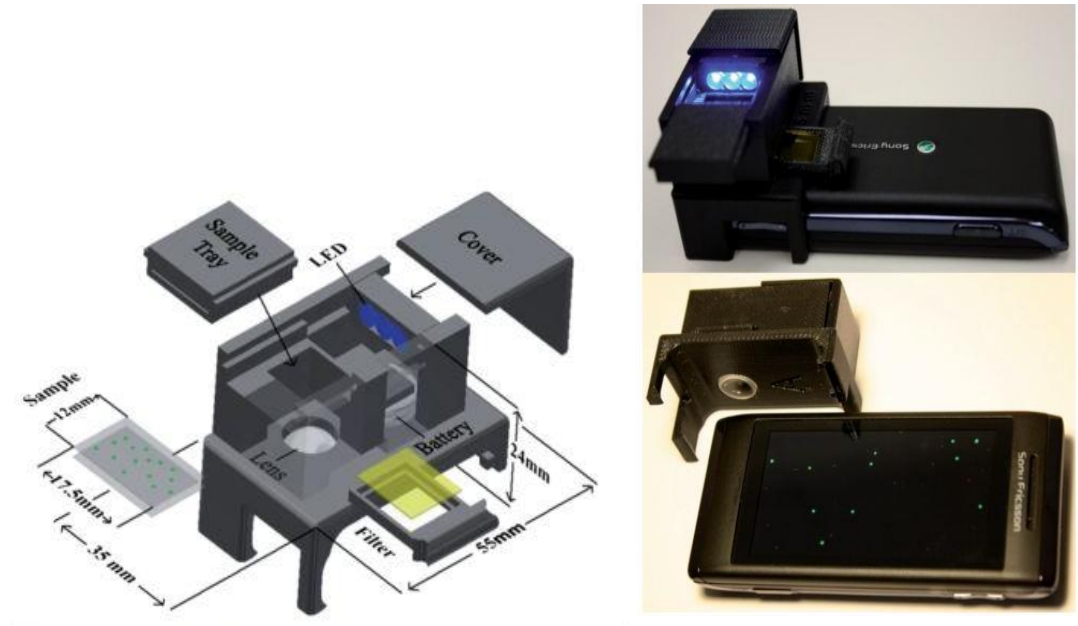

Figure 2.7: Left: Schematic diagram of the designed optical attachment for fluorescent imaging on a cell-phone. **Right:** Different views of the fluorescent imager prototype. This entire attachment to the cell-phone weighs ~28 g (~1 ounce) and has dimensions of 3.5 cm x 5.5 cm x 2.4 cm. This compact and lightweight unit can be repetitively attached and detached to the cell-phone body making its interface fairy user-friendly. [Adapted from[104]]

Table 2.1: Comparison different technique for devices propose for Point-of-Care

Methods	Measurements/Applications	Advantages	Disadvantages	Resolution
Microscope on mobile phone (2009) [100]		Connect to Mobile phone for cell imaging. Optical components are taken directly from a microscope	Expensive, Bulky	1.2 µm (Objective NA 0.85)
Optical lens on mobile phone (2011) [104]		Optical components are taken off the shelf Connected to Mobile phone to perform cell counting, Wide field of views (81mm2), low cost	Low resolution	20 µm but using algorithms to increase resolution to 10µm
Optofluidic Microscope (OFM) (2008) [106][107] [81]	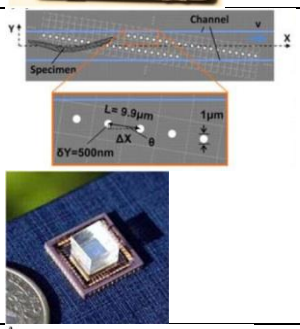	Chip scale, low cost, high resolution, for cell imaging	Sample needs to be in liquid and flow through each aperture, small FOV	1µm
Shadow imaging (2009) [86]	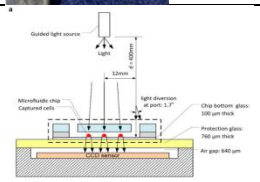	Chip scale, low cost, large FOV, for cells counting	Sample needs to contact or very close to CMOS chip. Require algorithms to decode diffraction patterns	Low resolution (N/A of NA)
Holographic microscopy (2009) [96][95][99]	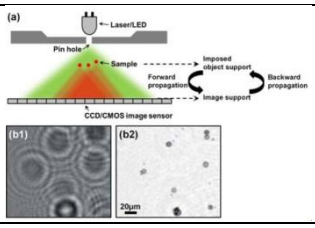	Chip scale, low cost, large FOV, for cells counting, high resolution	Require algorithms to decode diffraction patterns, require adjustment of light source through pinhole	1-2 µm

2.1.2.2 Microlens Based Imaging

Microlenses and microlens arrays can find use in applications such as sensing, medical diagnostics, lab-on-a-chip and point-of-care technologies. Microlenses can be categorized according to their focal lengths; fixed and tunable. The fixed focal length microlenses consist of a high refractive index material such as a polymer or glass. Fixed focal length microlenses are common in the new phone cameras. Advances in micromachining has enabled the development of microlenses, some of which can be "tuned" to achieve optical performance similar to the conventional objective lenses. The tunable microlenses require external pressure to change the radius of curvature of the liquid droplet lens and therefore adjust the focal length.

2.1.2.2.1 Fixed Focal Length Microlens Arrays

Although tunable microlens technique provides flexibility of focusing, it also requires external actuation source to change the focus of then lens focus increasing the level of complication. From a simplicity point microlenses might be a better solution for point-of-care applications[108]. Most of these microlens arrays are fabricated by micro machining methods [24], [64], [69], [109]–[112]. A few examples of different microfabrication techniques are reviewed below.

In 2003, Toshiyoshi et al[113] presented the design, fabrication and operation of an optical scanner array using photoresist reflow technique to form a microlens. They patterned a circular photoresist (260 μm diameter) and baked it on a hot plate at 150°C for 1 min. The resist was half melted and thermally transformed into a spherical microlens due to surface tension effect (**Figure 2.8**). The numerical aperture obtained from this microlens was 0.11 with 670μm focal length. This simple process was a great start on microfabricating photoresist based

microlenses. These lenses were typically had a low NA due to the small height to thickness ratio obtained using this technique.

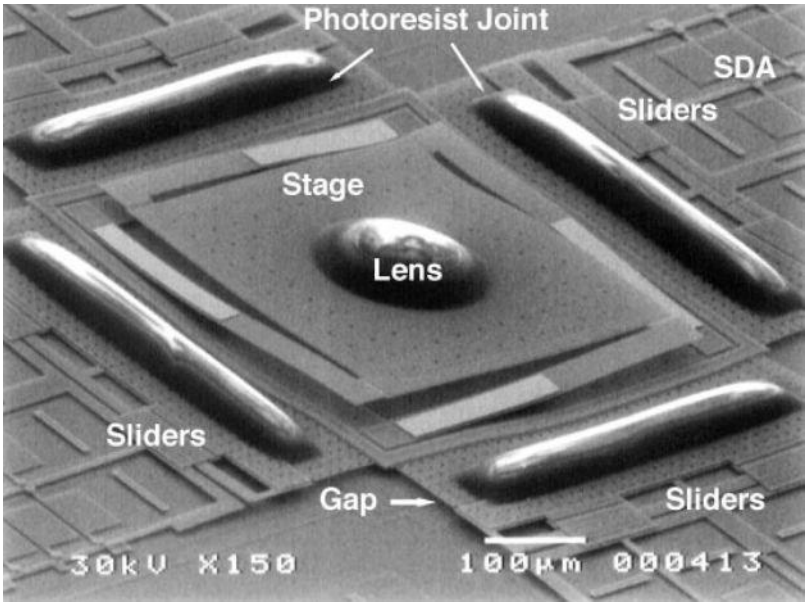

Figure 2.8: Prototype design of scamming lens. Taken from [113]

In 2005 Yuan et al [114] demonstrated the soft-lithography method to fabricate a high numerical aperture microlens in a hybrid photosensitive sol-gel glass. They used a photoresist master, PDMS as elastomeric replica molds and hybrid sol-gel glass as the end structure of a microlens array (MLAs). The sol-gel glass is a hybrid polymer composed of a Si-O-Si network incorporating UV curable polymeric groups. The photoresist master was fabricated using reflow method[113] thermally heating the photoresist at 160 °C for 30 minutes. The negative impression is formed by coating thick PDMS on the photoresist mold (**Figure 2.9**). After curing at 40 °C for 24 hr (or 90°C for 1 hr), the negative replica PDMS is peeled off the photoresist

master mold. Next, the PDMS mold is pressed on to the liquid sol-gel glass layer, which fills the microlens shaped depressions in the mold. The sol-gel glass precursor is solidified by exposing it to UV (365nm) for 30 minutes. Polymerized sol-gel glass is mostly silicon dioxide glass with a refractive index of 1.52 at 633 nm. The NA obtained from this method is ~ 0.3 to 0.5 from 20-232 μm diameter sol-gel MLAs. This technique has been commonly used in fabricating MLAs. Su-8 photosensitive polymer has also been used as microlens material replacing the sol-gel glass. The sol-gel material is now commercially available under commercial name ORMOCER polymers[115]. This technique is simple to implement however the quality of the microlenses can deteriorate due to the multiple use of the mold.

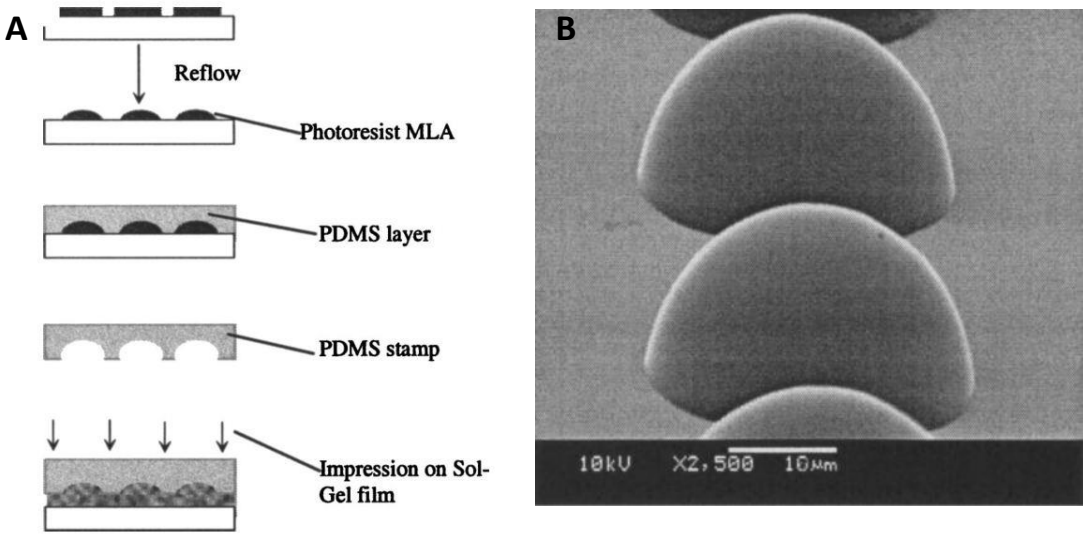

Figure 2.9: (A) Schematic of the soft-lithography of high NA MLA in sol-gel glass (B) SEM of fabricated sol-gel MLAs. [Adapted from [114]]

In 2009, Albero *et al*[116] reported a novel process for making hemispherical microlenses using HF/HNO_3 to isotropically wet etch of silicon.. By combining circular stirring

at an appropriate speed and random agitation while etching to uniformly distribute the catalyst (HF) to the opening active silicon area is the key to obtain uniform round high aspect ratio microlens master mold. Alberto et al also fabricated polymethyl methacrylate (PMMA) MLAs by hot embossing method. PMMA microlenses (refractive index of 1.49) created by this technique give NAs from 0.15 – 0.45 with a mask aperture diameter of 225 - 12 μm respectively (**Figure 2.10**). The smaller the mask diameter, the higher the aspect ratio of isotropic etching and better round curvature can be created. As a result, a smaller mask aperture diameter can produce a higher NA.

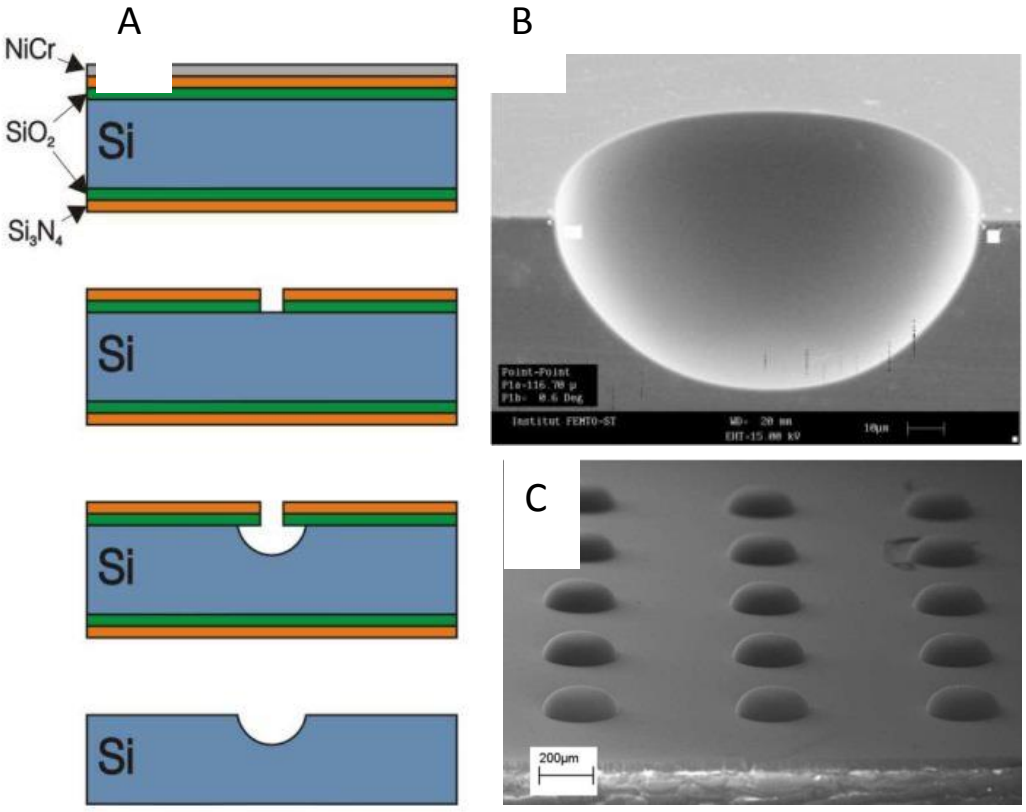

Figure 2.10: (A) Schematic of the isotropic wet etching in Silicon (Si) to create high NA master mold (B) SEM of almost perfectly isotropic mold from wet etching in the Si (C) Hot embossed of PMMA MLA with diameter of 262 μm. [Adapted from [116]]

Ink-jet printing technique is a serial process to fabricate MLAs[117], [118]. It is still an attractive technique due to the commercial drop-on-demand ink-jet printing systems available. The tool is simple to use and low cost relative to the conventional photolithography. The printing technique used a 50 μm diameter nozzle to deposit high numerical aperture UV curable polymer. As a result, the semi-spherical microlenses of up to 50 mm diameter can be produced in an array. An NA of 0.37 was reported [118] on sol-gel hybrid polymer (ORMOCER) of 29 μm diameter microlens with very short focal distances of 45-50 μm (**Figure 2.11**).

In 2011, Tripathi *et al* [24] proposed a fixed focus high NA arrays of doublet microlens approach. Their doublet microlens array consisted of glass microspheres trapped in PDMS using microfabrication and a fluidic assembly technique (**Figure 2.12**). They demonstrated magnified images of 1 and 2 μm patterns formed on a CCD sensor using a microlens array as shown in Figure 2.9 E,F. Their system demonstrated the highest NA obtained up to that time at NA=0.5 (**Table 2.1**)

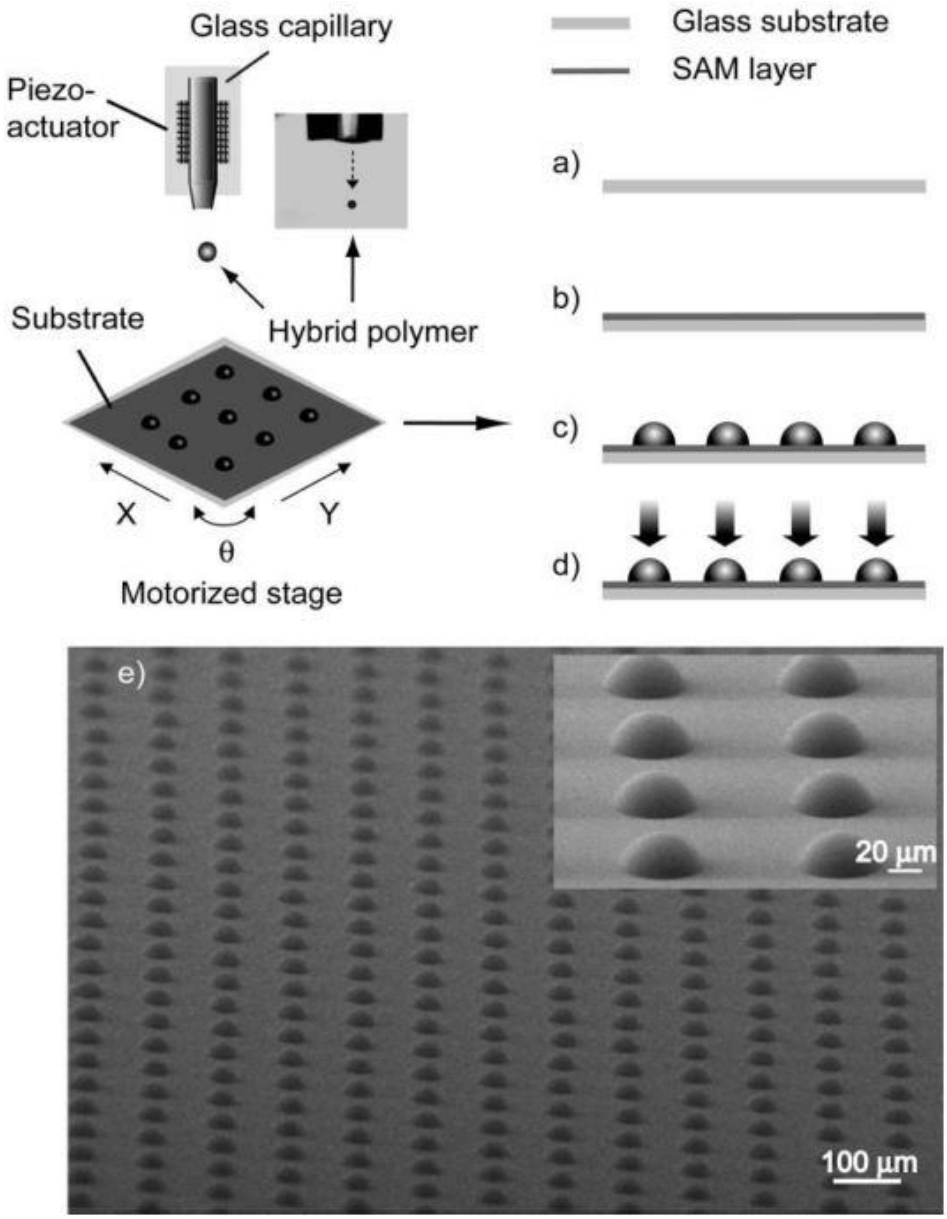

Figure 2.11: Schematic diagram of the dot-on-demand ink-jet printing to fabricate microlenses. (a) clean glass substrate, (b) treated glass substrate, (c) ink-jet printing of a hybrid polymer and pre-bake, (d) UV-exposure and post-exposure bake, (e) SEM of the 64x64 MLA and magnified image of MLA. The diameter and height of the microlens is about 53 and 18 mm, respectively. Adapted from [118]

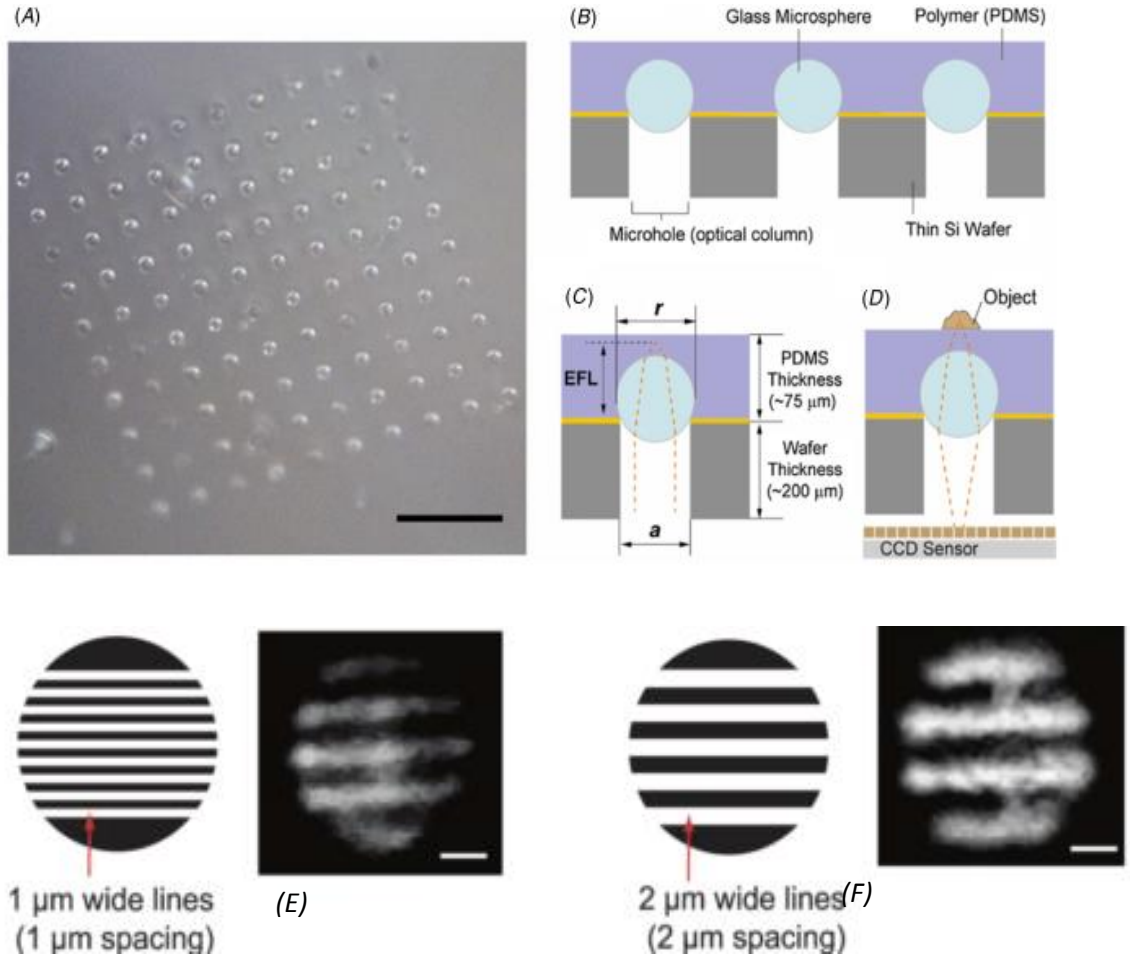

Figure 2.12: (A) Doublet microlens array. Scale bar:500 mm **(B)** A cross section schematic of the microlens array. **(C)** Collimated light beam is focused at a point right below PDMS surface. **(D)** Mechanism of image formation using the doublet microlens array. **(E,F)** Brightfield, transmission image of 1 and 2 mm line resolution patterns respectively using one of the doublet microlens arrays. Taken from[24]

2.1.2.2.2 Tunable Microlens Arrays

Over a decade, several research groups have been developing tunable microlenses [63], [65], [67], [74], [119]–[124]. One remarkable example of tunable liquid lens system that does not require complicated external control systems was demonstrated by Dong *et al* [65] in 2006. The tunable lens is made from a stimuli-responsive polymer hydrogel. They synthesized unique N-isopropylacrylamide (NIPAAm) temperature-sensitive hydrogel polymer and 2-(dimethylamino) ethyl methacrylate (DMAEMA) pH-sensitive hydrogel polymer. The hydrogel can instantaneously sense the presence of stimuli (ionic diffusion and surface tension, temperature or light), then change in volume and thus adjusting the focal length of the droplet within millisecond response times (**Figure 2.13**).

In 2009, Anurag and Chronis [78] presented a novel approach to microfabricate high numerical aperture polymer-based planar microlens array (MLA) (**Figure 2.9**). The microarrays consist of deformable elastomeric membranes of poly-dimethylsiloxane (PDMS) and polymer-filled photosensitive (SU-8) microchambers. When the PDMS membranes are pressurized (7.5-30 psi), they can expand up to 40-60 μm in diameter. The photosensitive SU-8 polymer in the microchambers is exposed to UV, crosslinked and become solid microlenses. They obtained numerical apertures as high as 0.3 from 60 μm diameter microlenses.

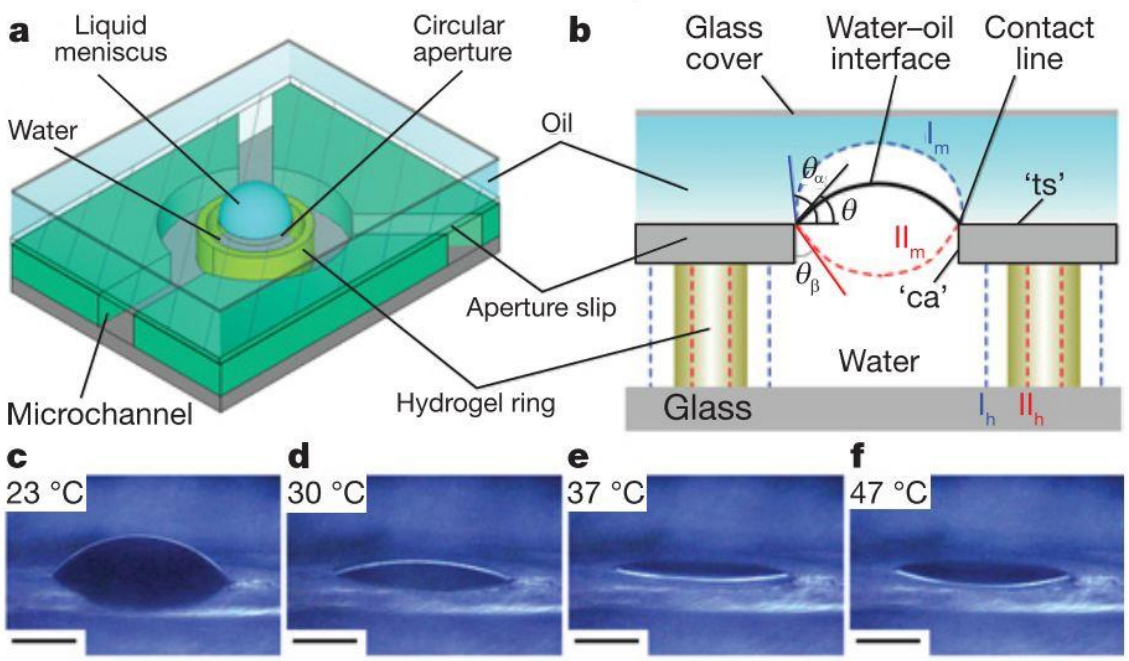

Figure 2.13: Smart microlens using a pinned liquid–liquid interface. a, The water–oil interface forms the liquid microlens. The microchannels allow the flow of fluids to the microlens structure. b, Tunable-focus mechanism. The hydrophilic sidewall and bottom surface ('ca') and hydrophobic top surface ('ts') of the aperture pin the water–oil meniscus along the contact line 'ca-ts'. The expansion and contraction of the hydrogel regulates the shape of the liquid meniscus by changing the angle θ of the pinned water–oil interface. The blue dashed lines show the expanded state of the hydrogel ring ('I_h') and the corresponding divergent microlens ('I_m') at $\theta=\theta_\alpha$. The red dashed lines show the contracted state of the hydrogel ring ('IIh') and the corresponding convergent microlens ('II_m') at $\theta = -90$ shape of the liquid microlens varies with local environmental temperature. shape of the liquid microlens varies with local environmental temperature. Scale bars, 1.0mm. [Taken from [65]]

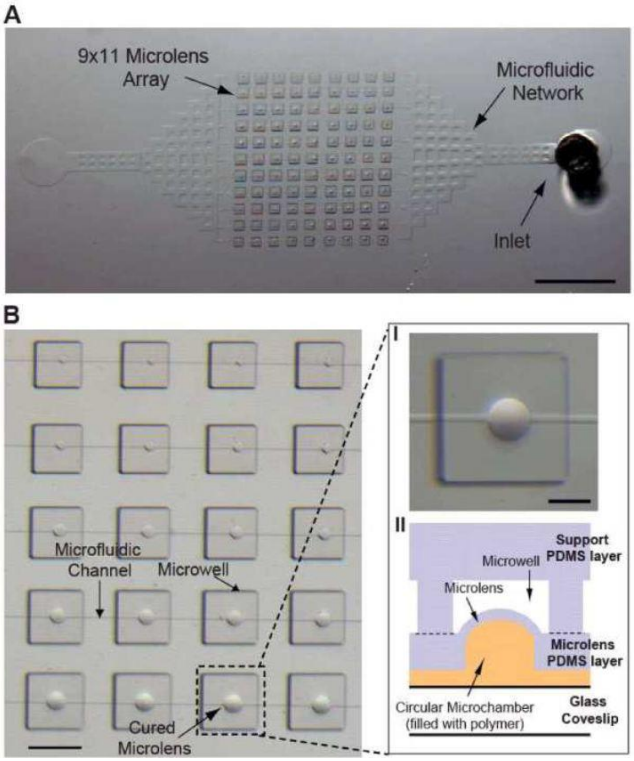

Figure 2.14: (A) A picture of a 9x11 PDMS-based, planar microlens array. The right inlet is used to fill up the microfluidic network with the UV curable polymer (the left inlet is not used in the depicted design). Scale bar, 1.5 mm. (B) A close-up view of 16 cured microlenses of different diameters. Each microlens sits beneath a square microwell. Scale bar, 200 µm. A magnified top view of a 60 µm in diameter microlens cured at 30 psi and a schematic diagram of its cross section are shown on the right (I and II respectively). Scale bar, 50 µm. [Taken from [78]]

Table 2.2: Comparisons of the performance of microlens

	Microlens diameter (μm)	NA	Materials	Focal length tenability	Reproducibility	Image formation
Photoresist Reflow (2003) [113]	260	0.11	Photoresist (AZ 4620) n=1.617	No	Variable	Additional lens
Polymer molded (2005) [114]	232	0.22	Sol-gel polymer n= 1.55	No	High	Additional lens
Planar microlens (2009) [78]	60	0.3	SU-8 n=1.605	Yes	High	Additional lens
Ink-jet printed (2011) [118]	50	0.37	Sol-gel polymer n= 1.55	No	Variable	Additional lens
Doublet microlenses (2011) [24]	56	0.5	Glass bead n=1.51	No	Dependent on microsphere variation	Standalone

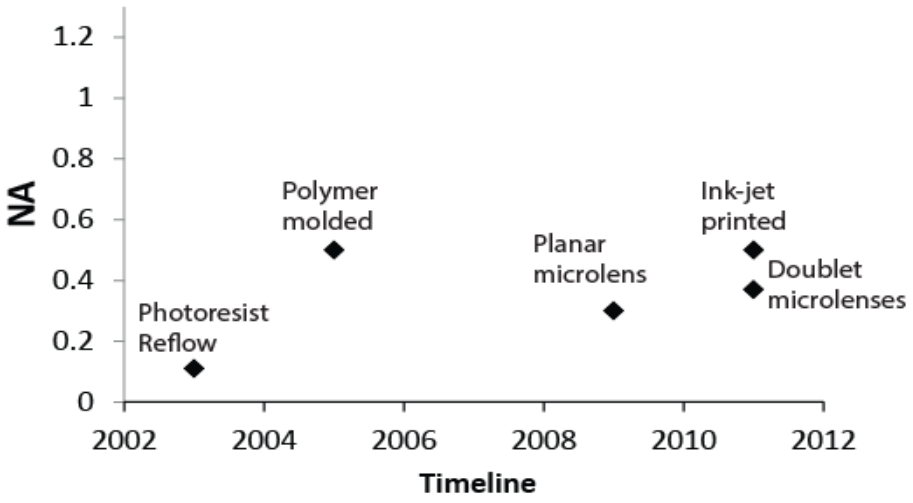

Figure 2.15: NA of microlens development over 10 years

2.2 Introduction (Implantable Pressure Sensor)

Blood pressure monitoring is required for several applications including the monitoring of critically ill patients with unstable cardiopulmonary status or patients on continuous infusions of vasoactive drugs[125]. Different types of MEMS sensors have been developed using different operating principles such as capacitive, piezoresistive, optical, etc. to measure blood pressure and pressure in other organs (e.g. eye, brain). For long term monitoring, wireless implantable sensors have been a preferred over wired systems due to a number of advantages such as ease of use, increased patient comfort, low risk of infection, low risk of damaged interconnects and therefore low risk of device failure[126]. Wireless telemetry can be either passive (RF based excitation and read out, optical read out) or active (integrated with circuit and battery). In this review section, we will be focusing on membrane-based MEMS sensors developed for blood pressure monitoring. Membrane deflection sensors can be integrated easily with telemetry electronics.

2.2.1 Commercial Implantable Blood Pressure Sensor based on Passive Telemetry: the CardioMEMS sensor

The smallest pressure sensors currently commercially available are the CardioMEMS EndoSensor^{TM}, a wireless implantable pressure sensor designed for monitoring blood pressure of patients with cardiovascular disease such as heart failure, abdominal aortic aneurysms (AAA) and hypertension. The device is implanted outside of the endovascular aneurysm repair site. The size is $\sim 0.23\ cm^3$ (5x30 mm), does not require any electronic or a battery and lifetime is greater than 3 years[44]. The concept of this device is shown in **Figure 2.16**. The sensor consists of a biocompatible inductor and capacitor circuit and measures changes in pressure by the changes in the resonant frequency of the LC circuit (LC tank). The inductor windings form a resonant

electrical circuit with the capacitor and are magnetically coupled with an external loop[43]. The sensor has a hermetically-sealed reference cavity and another flexible cavity, the flexible plate diaphragm of which deforms due to pressure from surroundings. The deformation of the diaphragm changes its capacitance and resonant frequency of the loop (RF), which results in changes in the response of the external loop. This passive telemetry based system has resonant frequencies in the 30-40 MHz range with Q-factors of ~50 and readout distance of ~20 cm. The fabrication of EndoSensor^{TM} uses standard MEMS methods.

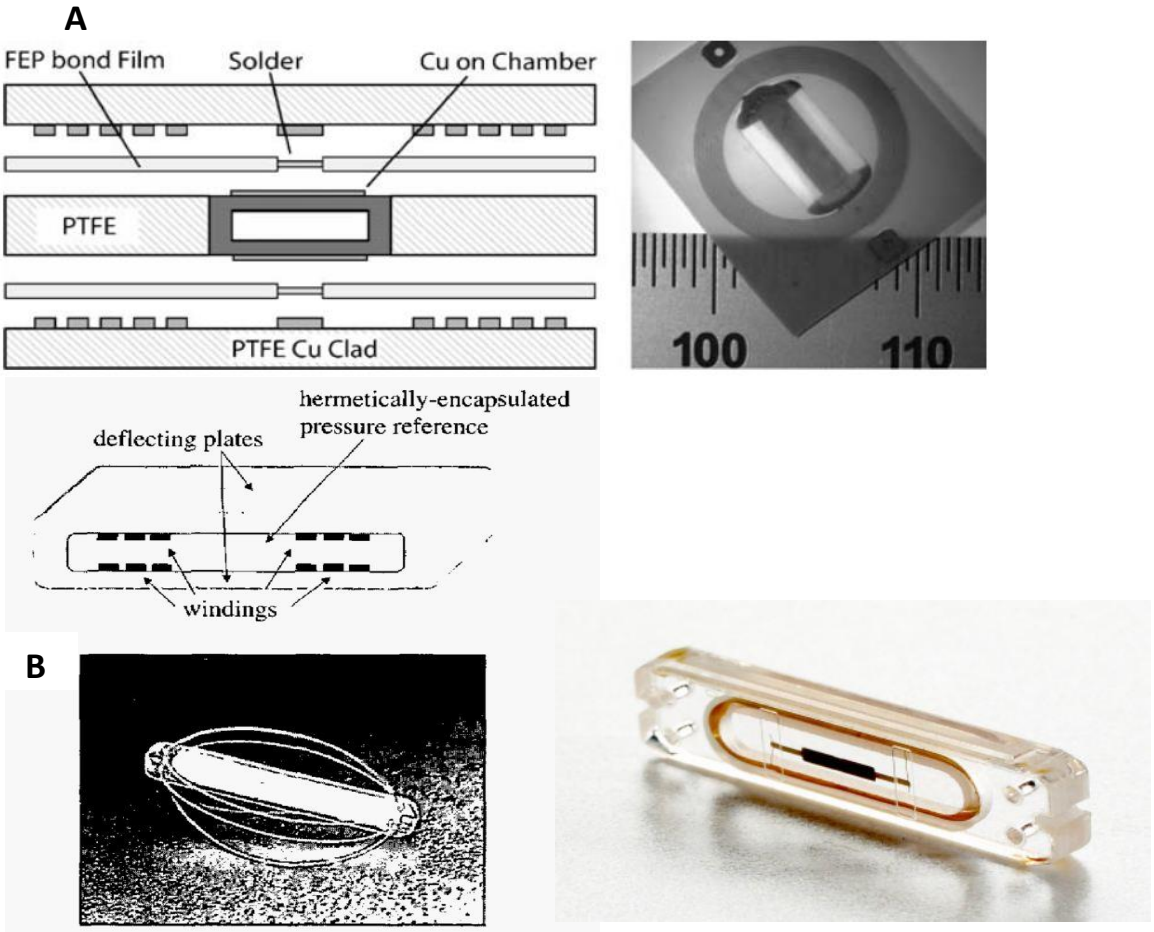

Figure 2.16: (A) The schematic cross-section of the CardioMEMS pressure sensor. (B) Fabricated sensor with ~ 5mm in width and 30mm in length

2.2.2 Implantable Blood Pressure Sensor based on Active Telemetry

DeHennis and Wise designed and fabricated an active telemetry implantable pressure sensor [29]. They developed a fully integrated 3μm BiCMOS circuit with arterial pressure sensor which consumes ~340 μW power and the capacitive sensor part is $2mm^3$ in size for monitoring the stenosed restriction in carotid artery. The sensor measures fractional flow reserve (FFR) in the arterial flow by comparing pressure differences of the two capacitive pressure sensors on each end of the sensor [127]. This concept of differential measurement is similar to ours with two different diaphragms registering different pressures. In their case capacitance changes due to pressure changes at both ends of the sensor result in differences in the LC oscillator resonant frequency which is read out by RF telemetry. The sensor had a resolution of 3 mm of Hg. The inductor antenna, pressure sensors and circuitry were fabricated with a combination of MEMS and BiCMOS methods (**Figure 2.17**). The capacitors were fabricated by anodic bonding of a silicon diaphragm and thin glass substrate, however, the lead tunnel is sealed using Si-Au eutectic reflow process. The fabrication of circuitry and antenna requires 22 lithography steps, 8 of them for the pressure sensor and 14 of them for the 3-μm BiCOMS circuitry and the antenna components. Overall dimensions of the DeHennis & Wise sensor match existing commercial sensors for Carotid artery and are too large for coronary arteries.

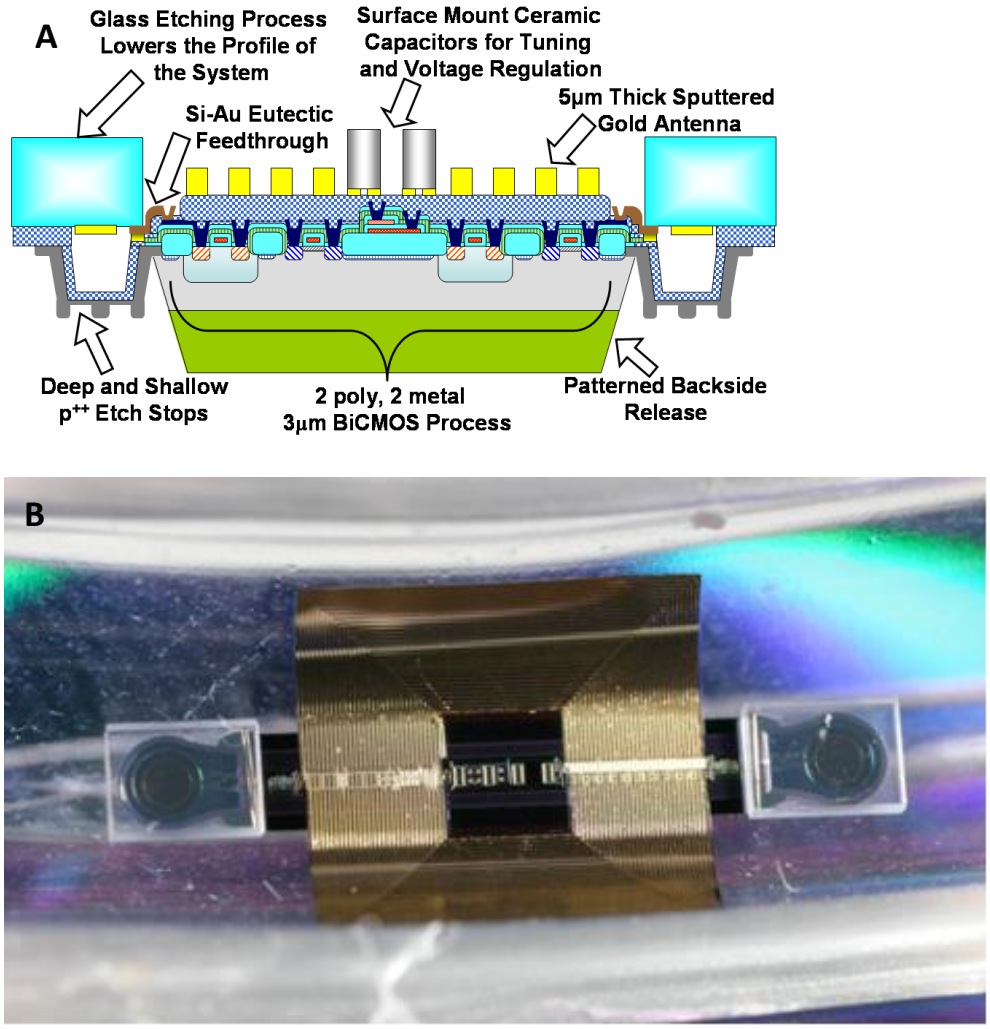

Figure 2.17: (A) Cross-section of final device with integrated 3 μm BiCMOS circuitry, capacitive pressure sensors and on chip antenna. (B) Photo of the released wireless system with two pressure sensors and telemetry readout circuit. Adapted from [29]

CHAPTER 3

An Optofluidics Lens Array Microchip: A Compact Module for High Resolution, Large Field of View Imaging

As mentioned previously point of care devices need to be portable and compact for carrying along, easy to use by untrained personnel, fast and accurate in providing the needed information to the doctor and be independent of external power or other utilities. These requirements also apply to optical POC systems. In this chapter we present the results of our efforts to make an optofluidic chip –termed the Microfluidic-based Oil-immersion Lenses (μOIL) chip which can become the heart of an optical imaging POC system.

3.1 Innovation

Resolution is the most important criteria for an optical imaging system. Our goal was to have submicron resolution with the simplest, cheapest and smallest optical system possible. To reach this goal we made a number of innovations. The first was combining high refractive index ball lens with index matching fluid in a microfluidic holder. This combination resulted in a high NA optical system. However, increasing NA leads to decreasing field of view (FOV). In order to achieve both high NA and a large FOV we made an array of high index ball lenses all of which could be imaged simultaneously with a CMOS sensor. Our final innovation was to make the whole optofluidic ball lens array smaller than a ten cents coin. The rest of this chapter describes how we achieved these goals.

3.2 Introduction

This chapter presents microfabricated, simple-to-use, reusable and optofluidic chip integrated with an array of 16 high refractive index ball lenses. The integrated chip –termed the μOIL chip - mimics the working principle of the front end of expensive, oil-immersion microscope objectives. The key element of the design is the integration of a microfluidic chip with an array of 16 liquid-immersed, high refractive index ball mini-lenses. The μOIL chip alone has a maximum numerical aperture of 1.2 and a magnification of 130X. It is attached directly to the sample of interest and then imaged under a standard micro stereoscope by simply adjusting the focus and/or the magnification of the stereo microscope. The purpose of using an add-on optical module is a solution to obtain high image resolution from stereomicroscope at low cost.

3.3 The μOIL Chip

Architecture of the μOIL chip. The μOIL chip consists of a 4x4 array of 1 mm in diameter ball mini-lenses. They are precisely seated on top of an array of 970 μm in diameter microwells, etched on a silicon chip (**Figure 3.1A & 3.1B**). We used the term 'ball mini-lenses' to indicate that they are small in size but they are not microfabricated. Those commercially available, ball mini-lenses are made of a high refractive index material (sapphire, refractive index 1.77, Edmund Optics, catalogue number 43-638) that greatly increases the numerical aperture (NA) of the system. They are half immersed in microscope oil, and half exposed to air. As a result, they act as doublet lenses, resembling the front end of a high-end, oil immersion microscope objective. We choose those mini-lenses as they have optical quality surface finish, tight tolerances (diameter, sphericity) and excellent broadband transmission. The silicon microwells are connected to each other through an open-air microfluidic network that distributes the oil uniformly to the entire array. The silicon chip is bonded to a thin glass substrate in order

to seal the bottom of the microwells. The dimensions of the various elements of the μOIL chip were chosen such as the focal plane of the ball mini-lenses is located at the bottom surface of the glass chip.

The sample, which typically sits on a transparent substrate (e.g. a microscope glass slide), is placed underneath the μOIL chip at a fixed distance from the ball mini-lens array. That distance is accurately defined by the thickness of a spacer. The spacer can be a thin photoresist film that is patterned on the bottom of the glass substrate or stacked glass chips (typically 100-300 μm thick) placed underneath each side of the μOIL chip. The latter option is recommended when a large field of view (FOV) is desired and high resolution is not that critical. When the sample/μOIL chip assembly is imaged through a stereoscope (**Figure 3.1C**), a high resolution and magnified image of the sample is obtained. Using an array of 16 ball lenses fully assembled on the μOIL chip (**Figure 3.1B**), one can observe simultaneously multiple areas of interests.

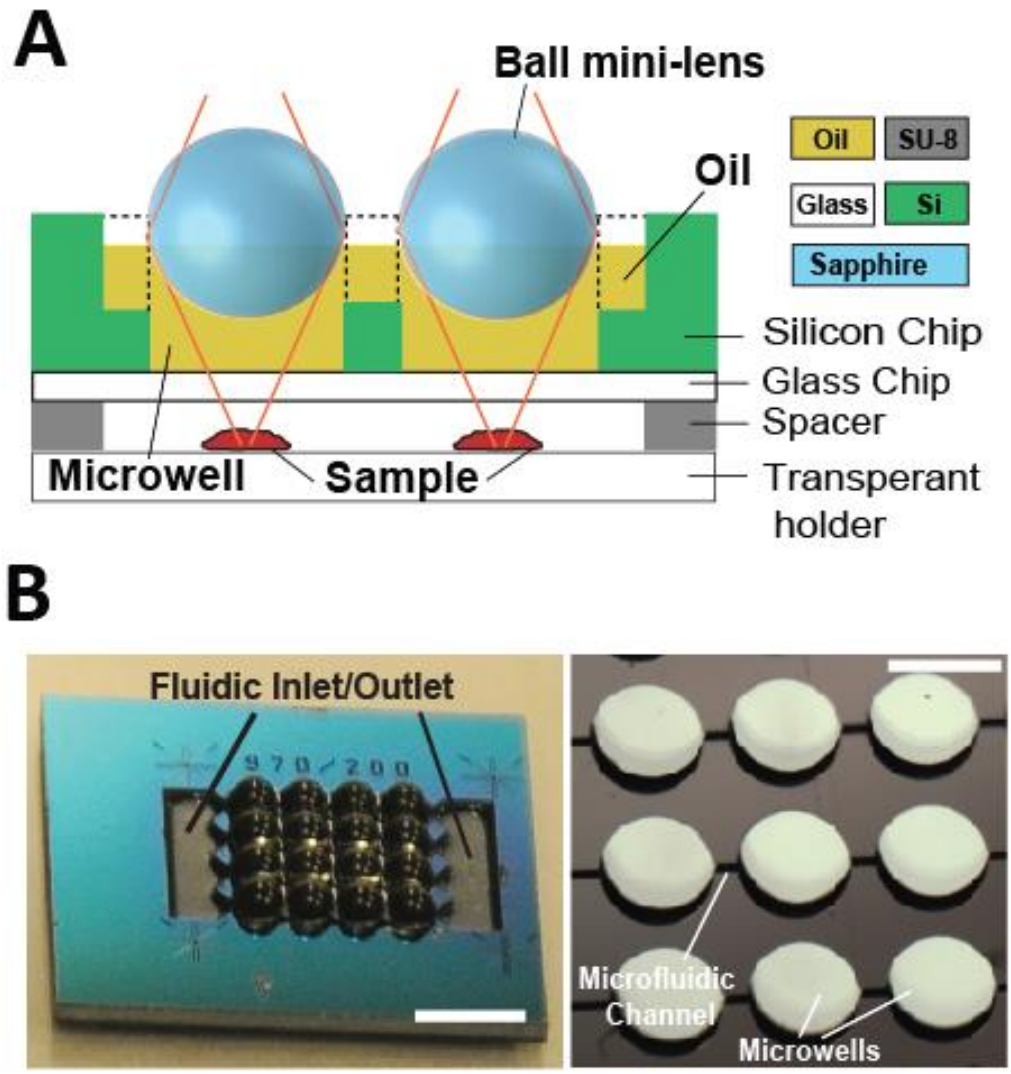

Figure 3.1: (A) Cross section schematic of the μOIL chip. (B) A picture (left) of the microfabricated μOIL chip (scale bar, 3 mm) and a close up view (right) of the microwell array with no ball mini-lenses (scale bar, 1 mm).

3.4 Microfabrication

The μOIL chip is fabricated using a 2-mask, standard silicon micromachining processes. The fabrication process consists of the following steps (**Figure 3.2A**): 1) a 400 μm thick silicon wafer is thermally oxidized to form a 200 nm thick SiO_2 film. The SiO_2 film is photolithographically patterned and HF-etched to create a hard masking layer for etching the microfluidic network, 2) a 5 μm thick photoresist film is then patterned using the second mask that contains the microwell array and a deep reactive ion etching (DRIE) step is performed to partially etch 200 μm out of the 400 μm microwell total thickness, 3) the photoresist is then stripped to expose the SiO_2 film. A wafer-through DRIE step is then performed to obtain the 200 μm thick microfluidic network and the microwells, 4) the silicon wafer is anodically bonded to a 100 μm thick Pyrex wafer and the bonded wafer is diced. A 5 μm thick SU-8 film - the spacer - is patterned at the bottom of each individual chip. Instead of using the SU-8 film, multiple glass coverslips can be stacked on top of each other and glued on the sides of the chip if it is desired to increase the distance between the μOIL chip and the sample, 5) the microfluidic network is filled with microscope immersion oil (Cargillis labs #159, refractive index 1.52) and, 6) the ball mini-lenses are manually assembled on the top of the oil-filled microwell array and kept in place by surface tension. They are separated from the bottom surface of the microwell array by ~20 μm. Before use, the μOIL module is placed on a flat surface for 30 minutes to let oil evenly distribute into the microwell array. The assembled μOIL module is then ready for use: it can then be placed on top of any specimen to obtain high resolution images through a stereoscope. The μOIL module can be re-used indefinitely as long as it is kept in a dry environment (to minimize oil

evaporation). It can also be cleaned and re-assembled if needed. For long term use, a thin parylene film can also be deposited to completely seal the μOIL module.

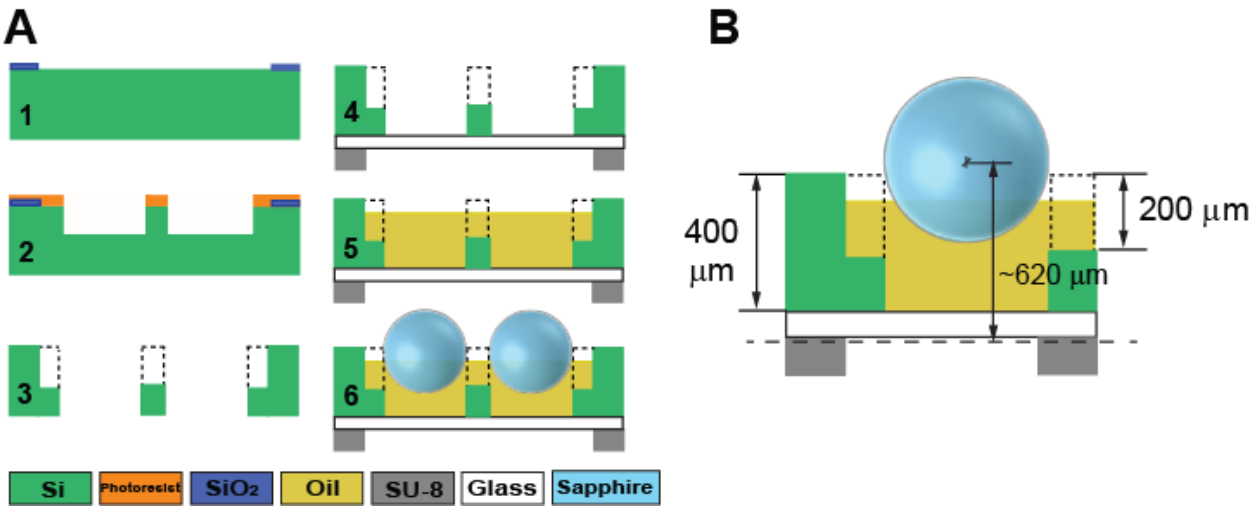

Figure 3.2: (A) Microfabrication process and (B) Critical dimensions of the μOIL chip. The focal length measured from the center of the ball mini-lens is ~620 μm. The dotted lines represent the microwell sidewalls that are not visible in the highlighted cross section.

3.5 Results & Discussion

3.5.1 The μOIL Module

3.5.1.1 Material Considerations

The amount of light collected by a lens -that also affects its resolution - can be quantified by its numerical aperture (NA):

$$NA = n_M \, Sin(\theta) \qquad (3.1)$$

where n_M is the refractive index of the medium that the lens is immersed into and θ is the half angle of the cone of rays collected by the lens. The maximum half angle θ - and therefore the maximum NA - can be obtained when the sample is located at the focal length of the lens. In

order to increase the NA, one should increase the refractive index of the medium and/or increase the angle θ. The former task can be achieved by using media that have high refractive index (e.g. oil or water). The latter one can be achieved by combining the high refractive index media with a high refractive index lens.

Our μOIL chip has similar behaviour that can be described by equation (**3.1**): the effect of the refractive index of the medium and the ball lens material are critical for achieving high NA. We choose to use microscopy oil as a medium in order to match the refractive index of the glass chip that seals the bottom of the microwell array. The use of oil reduces the total internal reflection of optical rays at the glass/oil interface, resulting in an increase in angle θ (the focal length also increases in this case, but the effect in angle θ is less significant) (**Figure 3.3A**). Microscopy oil also does not fluorescent and does not evaporate as fast as other media. In addition, by using a high refractive index lens material (e.g. sapphire, refractive index n_L= 1.77), the focal length decreases and the optical cone widens (angle θ increases) (**Figure 3.3B**).

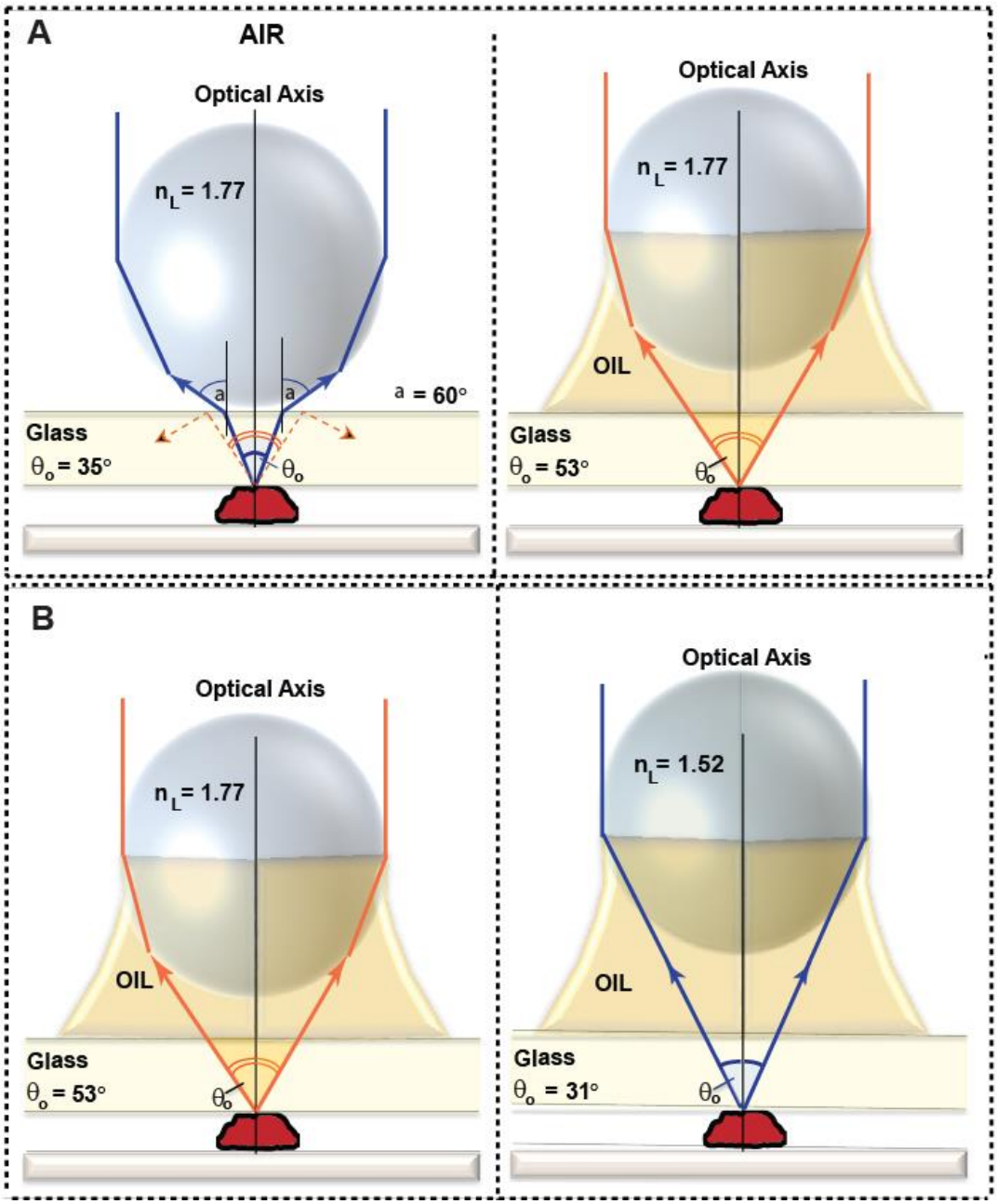

Figure 3.3: The effect of the refractive index of the immersion medium (**A**) and ball lens (**B**) on the ray collection angle θ_o. Values for angle θ_o are theoretical estimated by thick-lens equations

This specific combination of materials results in a high optical performance of the μOIL module (table 1) which is excellent for high-resolution imaging. We should emphasize that due to the modular assembly of the ball mini-lenses, the oil and the silicon/glass chip, the end user has the ability to custom-made his/her μOIL module.

To theoretically calculate the NA of μOIL chip, the maximum half angle (θ) of the cone of rays collected by the lens, the geometry and material properties of the 2 media and the ball mini-lens are needed.

3.5.1.2 The Numerical Aperture (NA) of the μOIL chip

In order to estimate the NA of the μOIL module, we modelled the ball lens as a thick lens [128] that is half immersed in medium and half immersed in air (**Figure 3.4)**. According to the thick-lens equations [34], [38- 39]:

$$\Phi_{IS} = \frac{n_{air} - n_L}{R_1} \quad (3.2)$$

$$\Phi_{OS} = \frac{n_L - n_M}{R_2} \quad (3.3)$$

$$\Phi = \Phi_{IS} + \Phi_{OS} + \Phi_{IS}\Phi_{OS}\left(\frac{CT}{n_L}\right) \quad (3.4)$$

$$P = \frac{\Phi_{IS}}{\Phi}\left(\frac{n_M}{n_L}\right)CT \quad (3.5)$$

$$P' = -\frac{\Phi_{OS}}{\Phi}\left(\frac{n_{air}}{n_L}\right)CT \quad (3.6)$$

$$EFL = \frac{1}{\Phi} \quad (3.7)$$

$$f_F = -n_M EFL \quad (3.8)$$

$$f_R = n_{air} EFL \quad (3.9)$$

$$BFL = f_R + P' \quad (3.10)$$

$$FFL = f_R + P \quad (3.11)$$

$$NPS = f_F + f_R \quad (3.12)$$

Where Φ_{IS} is the power of surface 1, Φ_{OS} is the power of surface 2 and Φ is Lens Power, n_M is object space medium index, n_L is Lens index, n_{air} is image space index (air), R_1 is Radius of surface 1 and R_2 is radius of surface 2, CT is center thickness of the ball mini-lens, P is primary principle point, P' is secondary principle point, EFL is effective focal length, measured from principle point to the focal point. BFL is back focal length of the ball lens measured from the lens surface to the focal point, FFL is the front focal length, NPS is the dodal point shift, f_F is front focal point and f_R is rear focal point.

Substitute eq. (3.2) and eq. (3.3) into eq (3.4):

$$\Phi = \frac{n_{air}-n_L}{R_1} + \frac{n_L-n_M}{R_2} + \left(\frac{n_{air}-n_L}{R_1}\right)\left(\frac{n_L-n_M}{R_2}\right)\left(\frac{R_1+R_2}{n_L}\right) \quad (3.13)$$

For the lens fully immersed in air, the focal point is expressed as follow:

$$\frac{1}{EFL} = \Phi = (n_L - 1)\left(\frac{1}{R_1} + \frac{1}{R_2} + \left(\frac{n_L-1}{R_1R_2}\right)\left(\frac{d}{n_L}\right)\right) \quad (3.14)$$

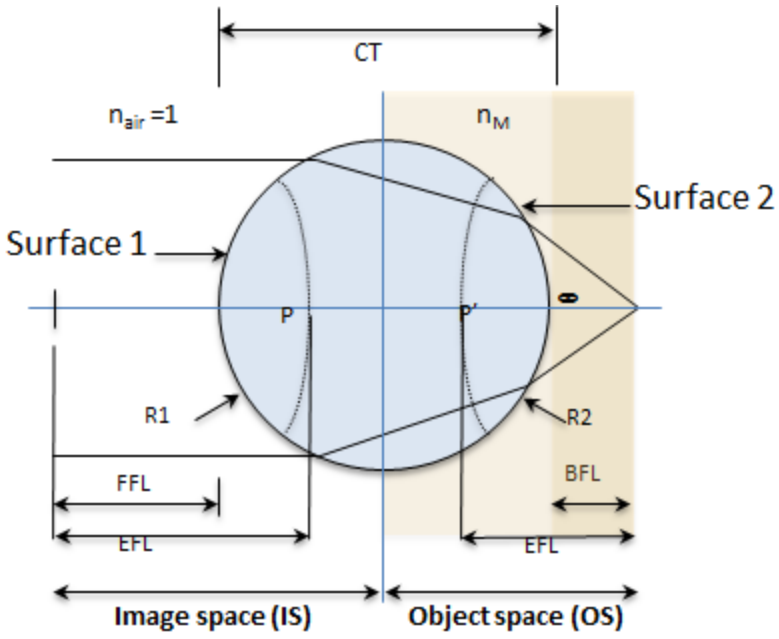

Figure 3.4: Schematic of a thick-lens immerse in two media.

The inverse lens power (Φ) is the effective focal point (EFL) of the lens where d is lens diameter. When the ball mini-lens is immersed in two different media, as in the case of μOIL, half of the lens is exposed in air where n_{air}=1 and half immersed in oil medium, Φ can be written as

$$\phi = \frac{1}{R}(n_M + 1 - \frac{2n_M}{n_L}) \quad (3.15)$$

Finding NA:

At the maximum acceptance angle, the optical rays originating from the sample will be tangent to the ball-lens surface (**Figure 3.4**) and NA can be expressed as

$$NA = n_M Sin(\theta) \ or \ n_M (\frac{R}{BFL+R}) \quad (3.16)$$

$$NA = n_M (\frac{\phi R n_L}{\phi R n_L + n_M n_L - 2(n_L - 1)(n_M)}) \quad (3.17)$$

Sapphire ball-lenses have a refractive index of 1.768. With the ball mini-lenses half immersed in immersion oil, the back focal length (BFL) of μOIL was calculated to be 124.5 μm away from ball-lens surface. The Lens power is $1.6mm^{-1}$, while BFL is 124.5 microns, the maximum acceptance angle ($\boldsymbol{\theta_{max}}$) is 53 degrees. The theoretical NA of the Sapphire ball-lens can be as high as 1.2.

Table 3.1: Properties of μOIL Chip

PARAMETER	VALUE
Ball mini-lens Diameter (D)	D = 1mm
Ball mini-lens Refractive index (n_L)	n_L = 1.77 (sapphire)
Back Focal Length (BFL)	124μm (see supplementary material)
Numerical Aperture (NA)	1.2 (from equation (3.17))
Lens power (ϕ)	$1.6mm^{-1}$ (from equation (3.15))
Magnification	~130x (see **Figure 3.5**)
Resolution (center)	0.7 μm (see **Figure 3.7**)
Depth of Field (DOF)	0.38 μm (from $\frac{\lambda}{NA^2}$) [69] [73]
F- number	0.62 (from $\frac{EFL}{D}$)

*Optical properties are calculated when the sample is located 5μm below the focal plane (that is when a 5 μm thick spacer is used)

** EFL: the effective focal length, λ: the wavelength

To better understand the dependence of NA on n_M and n_L, we plotted the NA versus n_L, when the ball mini-lens is immersed in 4 different media: air, water, oil and PDMS (**Figure 3.5**).

Air, water and oil are widely used media in standard optical microscopy. To cover the low end of the n_M spectrum, we choose PDMS as an alternative low-cost solution. The n_L of the lens was varied from 1.4 to 2, as those values represent refractive indices of off-the-shelve ball lenses (e.g. N-BK7 (n_L= 1.516), Ruby (n_L=1.77), S-LAH79 (n_L=2), etc). In the calculations to plot **Figure 3.5**, we did not take into account the aperture created by the silicon well (the silicon well is 30 μm smaller in diameter that the ball lens diameter) and we assumed that the top half of the ball-lens is exposed to air. The authors want to note that in reality, the size of the holder aperture (i.e. silicon well) is critical and therefore need to take into account since light blocked by smaller aperture will reduced rays and effect NA value. For all practical purposes, we also assumed that the sample is located at the focal plane. The results quantitatively validate our expectations: the higher the n_M and n_L the higher the NA. For ball mini-lenses of small refractive index (n_L=1.5-1.6), an increase on the refractive index of the immersion medium does not result a significant increase in the NA. The effect of refractive index of the immersion medium on the NA is significant (up to ~50%) when ball mini-lenses with high refractive indices are used (e.g. n_L>1.7). The combination of microscope immersion oil (n_M=1.516) and sapphire ball mini-lens (n_L=1.77) results in a numerical aperture of NA=~1.2 which is comparable to high-end oil or water immersion microscope objectives. The effective aperture is 320 μm in diameter. This is the aperture which will allow a light collection cone angle of 53° based on the geometry of μOIL chip demonstrate in figure 3b.

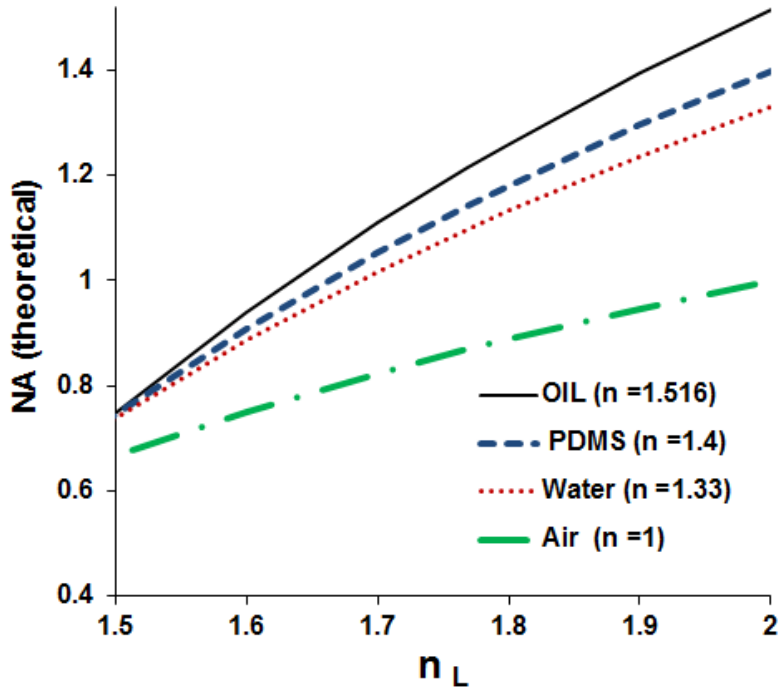

Figure 3.5: Numerical Aperture (NA) of the μOIL chip versus refractive index of the ball mini-lens (n_L) for four different cases of immersion media as theoretically predicted by equation (3.17).

3.5.1.3 Magnification and NA versus spacer thickness.

We performed optical simulations using OSLO software to obtain the magnification and numerical aperture as a function of the distance of the sample from the focal plane of the μOIL chip (the focal plane is located at the bottom glass surface of the μOIL chip). This distance coincides with the thickness of the spacer. For all practical purposes, we assumed a minimum spacer thickness of 5 μm (that is the thickness of the SU-8 film) and that the medium between the sample and the bottom glass surface of the μOIL chip is water. In this case, the numerical aperture and magnification are ~1 and ~130X respectively. As expected, when the spacer thickness increases, both the magnification and NA decrease (**Figure 3.6**). Spacer thickness has a

major impact on the magnification, as the magnification decay has an exponential trend. At a spacer thickness of 900 μm the magnification and the NA is 1X and ~0.01 respectively (data not shown), beyond that point the sample is being demagnified. We want to emphasize that this is the magnification obtained from the μOIL chip alone. For the combined stereo microscope/μOIL chip system, the total magnification is calculated by multiplying the magnification of the μOIL chip and the magnification from the stereo microscope.

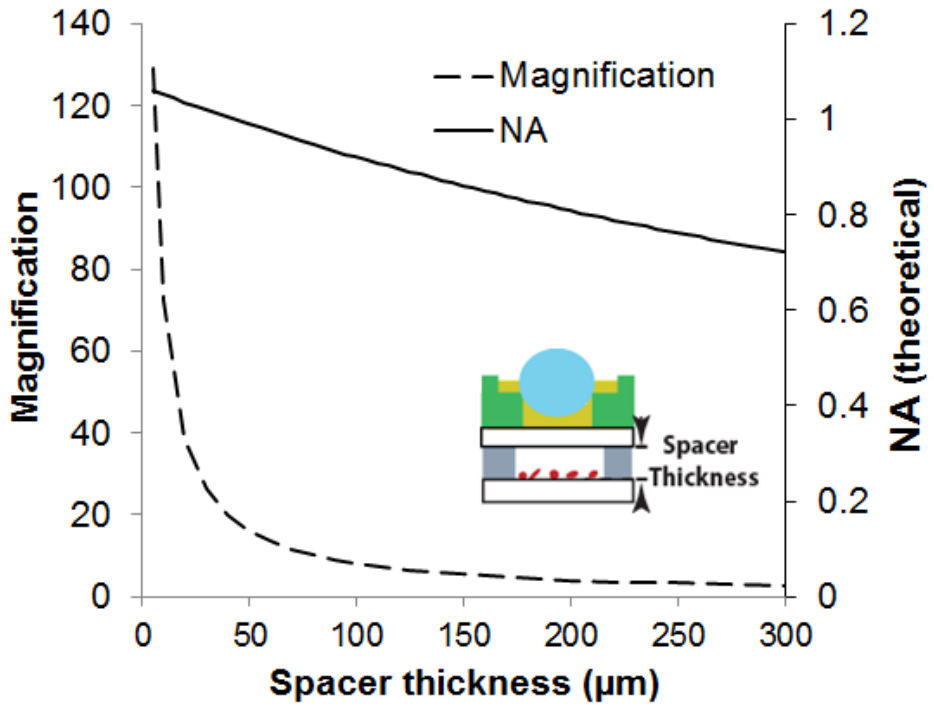

Figure 3.6: Dependence of the magnification and NA of the μOIL chip on spacer thickness.

3.6 Conclusions

We have developed a simple-to-use, reusable and compact, microfabricated imaging module for high resolution, large field of view imaging applications. The key element of the design is the integration of a microfluidic chip with an array of 16 liquid-immersed, high refractive index ball mini-lenses. The integrated chip –termed the μOIL chip - mimics the working principle of the front end of expensive, oil-immersion microscope objectives. The μOIL chip alone has a maximum numerical aperture of 1.2 and a magnification of 130X. In comparison to other microlens techniques, the μOIL chip is much simpler to make and has by far the highest NA and is the first one to achieve submicron optical resolution without software enhancement of the images (**Table 3.2 and Figure 3.7**).

3.7 Acknowledgement

I would like to thank Anurag Triphati and Mostafa Ghannad-Rezaie for their advice and helping me when I first start working in Prof. Chronis' group. I would like to thank Onnop Srivannavit for his help in microfabrication. All the devices were fabricated at the Lurie Nanofabrication Facility at the University of Michigan. I would like to thank Microfluidics in Biomedical Sciences Training Program (T32 EB005582-05) for my fellowship and research support from the National Institutes of Health (NIH) and the NIH Director's New Innovator Award (DP2OD006458).

Table 3.2: Comparisons of the performance of microlens techniques

	Microlens diameter (μm)	NA	Materials	Focal length tunability	Re-producibility	Image formation
Photoresist Reflow (2003) [113]	260	0.11	Photoresist (AZ 4620) n=1.617	No	Variable	Additional lens
Polymer molded (2005) [114]	232	0.22	Sol-gel polymer n= 1.55	No	High	Additional lens
Planar microlens (2009) [78]	60	0.3	SU-8 n=1.605	Yes	High	Additional lens
Ink-jet printed (2011) [118]	50	0.37	Sol-gel polymer n= 1.55	No	Variable	Additional lens
Doublet microlenses (2011) [24]	56	0.5	Glass bead n=1.51	No	Dependent on microsphere variation	Standalone
μOIL chip (2012) This work	1000	1.2	Sapphire bead n=1.77	No	Dependent on microsphere variation	Standalone

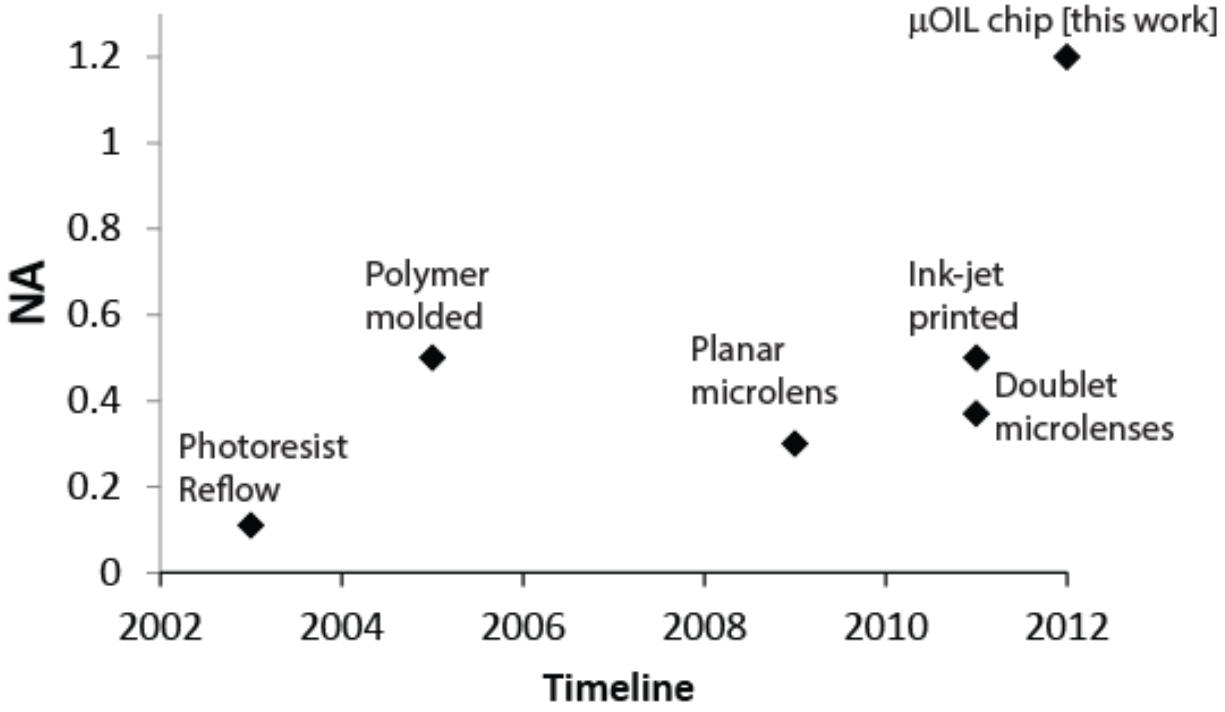

Figure 3.7: Comparing NA from different microlenses fabrication methods

---

CHAPTER 4

The μOIL chip as an Add-on Microchip Module for High Resolution Stereomicroscopy

4.1 Innovation

Given that low cost stereo microscopes are widely available and in use even in resource poor environments and by home hobbyists, we envisioned that our optofluidic chip described in the previous chapter can be a simple, cost effective, add on accessory to any stereo microscope to give it submicron imaging capability and thus open up new avenues of use. The lens array chip has dimensions of less than 6mmx6mmx1.5mm. Its use is as simple as putting it on top of the sample of interest and refocusing of the stereomicroscope. The details and performance are described below.

4.2 Introduction

Stereo microscopes are low-end, low-cost, imaging instruments, mainly used in the field of biology and medicine [131]. They provide 3D images, have long working distances, large fields of view and depth of focus. They are also modular, as the manufacturers provide a wide variety of objectives, stands and illumination accessories. Because of these advantages, they are commonly used in the lab or in the hospital for bacteria counting, organism and tissue imaging, as well as for dissecting and inspecting specimens [2–5]. Stereo microscopes are also used in geology, archaeology as well as for inspecting microparts and electronics, making jewellery and repairing watches [136].

Despite the advantages mentioned above, stereo microscopes have limited resolution (typically 10-20 microns) and magnification (1-6X without considering the magnification from the eyepiece) [136] when compared to the submicron resolution and magnification of up to 100x of expensive compound microscopes. In particular, low resolution is a critical shortcoming in low-end imaging systems as it prevents their use in clinical applications where cellular and sub-cellular imaging is needed.

An add-on optical module, e.g. a lens attachment for high-resolution imaging would be an attractive solution in order to maintain the intended generic use of a stereo-microscope.

Here, we report the development of a compact and inexpensive optical, add-on module that transforms any stereo microscope into a high resolution imaging system without compromising the field of view. The add-on module – a Microfluidic-based Oil-Immersion Lens (μOIL) chip - consists of an array of ball mini-lenses of excellent optical quality, that are microfluidically connected and half immersed in oil. The use of the μOIL chip is simple as it can be mounted on top of any biological sample and imaged through the stereo microscope by simply adjusting the focus. The μOIL chip is microfabricated on a wafer-level process, while the ball lenses are commercially available. The combined stereo microscope/μOIL chip system is an ideal tool for research studies and clinical applications where sub-micron and large field of views imaging is required.

4.3 The combined μOIL chip/ stereo microscope assembly

We evaluated the optical performance of a standard stereo microscope (Olympus SZ61) when the μOIL chip is used as an add-on module. We placed the μOIL module on top of various samples (test charts, blood cells) and analysed the obtained images. The stereo microscope we

used had a magnification range from 0.67X to 4.5X and was equipped with a 3.3 megapixel CCD (MicroPublisher 3.3RTV, with 0.5X de-magnifying lens in from of the camera). In all tests described below, we set the magnification of the stereo microscope to its maximum value of 4.5X that corresponds to a maximum NA of ~ 0.07 and a maximum resolution of ~ 10 μm [137]. We used bright field illumination in transmission mode by adjusting the mirror at the base of the stereoscope at ~45^0 degrees. The use of the μOIL chip as a module greatly enhances the resolution of the stand-alone stereo microscope (**Figure 4.1**). Using the stereo microscope alone, the finest pattern from a standard resolution plate (US Air Force - USAF1951) is blurred and none of the lines can be resolved (**Figure 4.1A**). When the μOIL chip is placed on top of the resolution plate, the narrowest lines (0.775 μm in width) are resolved (**Figure 4.1B**). Although, there is noticeable aberration away from the centre of the field of view.

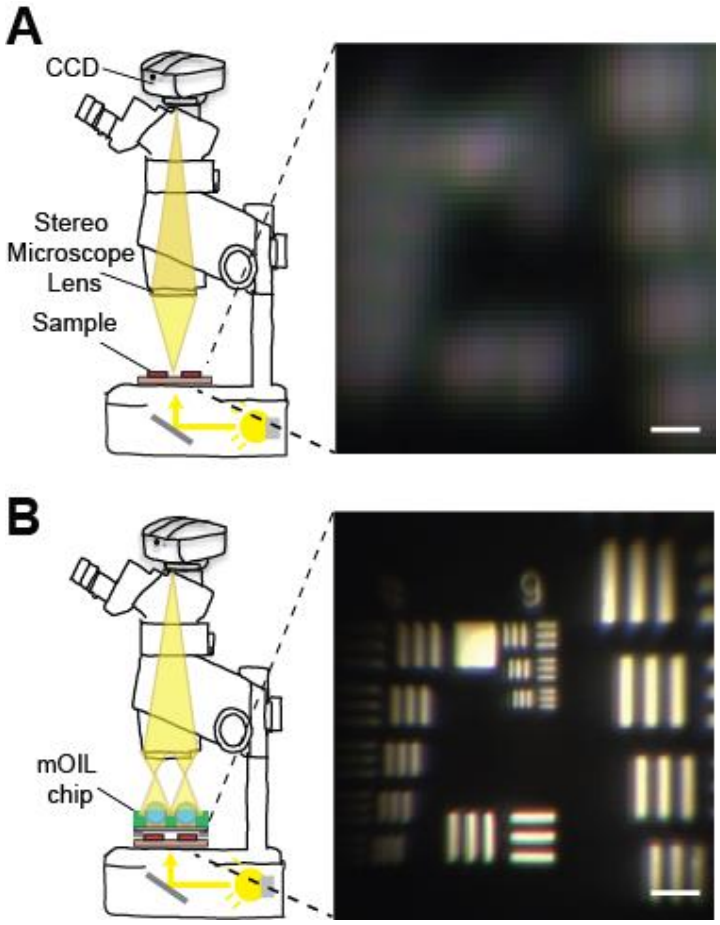

Figure 4.1: Images of a resolution plate (USAF1951) obtained from a stereo microscope alone (A) and from the combined μOIL chip/stereo microscope system (B). Scale bar: 10 μm in (A) and (B).

4.3.1 Resolution

To obtain the optical resolution of the combined system, we measured the image contrast of a resolution plate (USAF1951) that has equally spaced line patterns of decreasing width. The dependence of the image contrast on the line width represents the modulation transfer function of the combined system, which is a widely accepted method for obtaining the resolution of an optical system [138]. The acquired images were taken at the center within 30 μm diameter and analysed using Metamorph software and the percentage of the image contrast averaged over all color channels versus the number of line pairs per millimetre was obtained (**Figure 4.2**). In addition, we tested the effect on the resolution of a thin (~125 nm) parylene film that was deposited on top of the μOIL chip. As discussed above, the parylene film can permanently seal the μOIL chip in order to prevent evaporation of the oil as well as to serve as an anti-reflective coating [139].

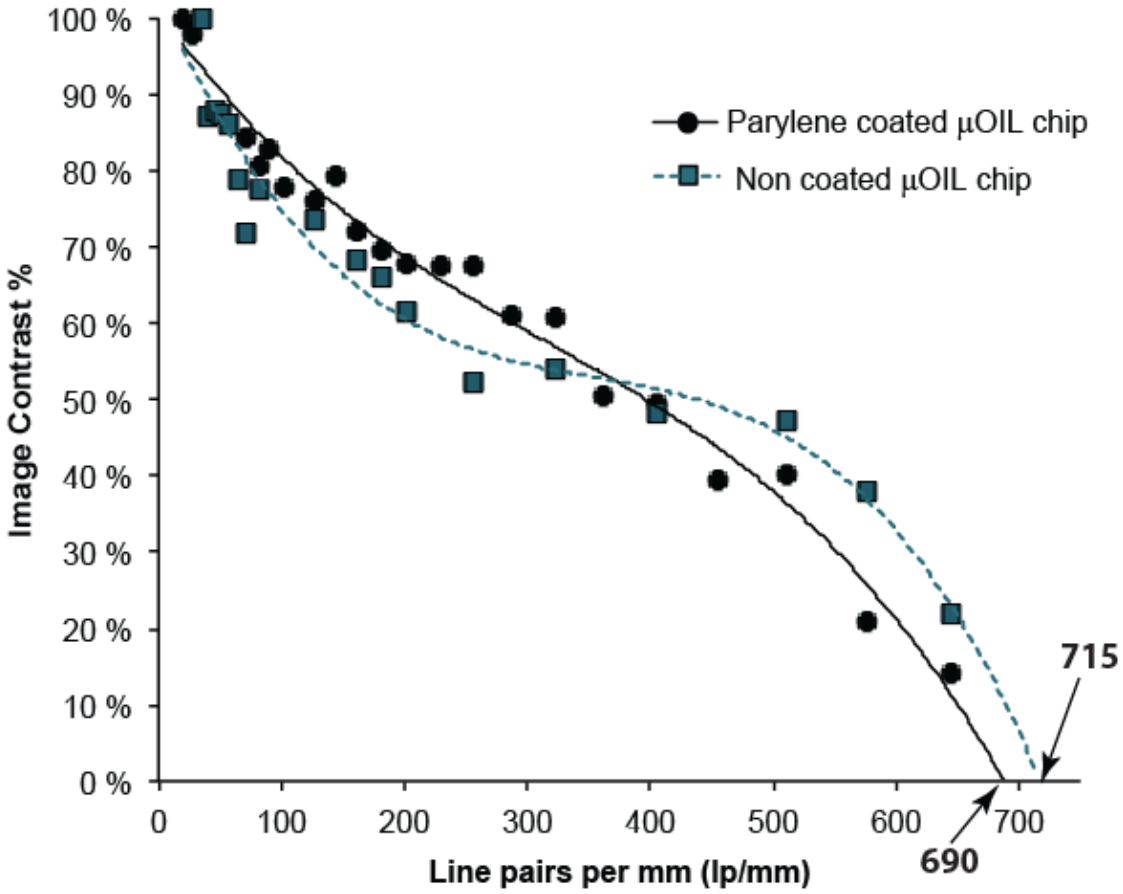

Figure 4.2: Image contrast (%) at the center of the FOV versus line pairs per mm for the combined system. The sample was a resolution plate that was imaged in air. The spacer thickness was 5 μm and NA (theoretical) is ~ 0.79.

The experimental results indicate that the image contrast percentage decreases continuously as the number of line pairs per mm increases. All the lines from the resolution plate -even the smallest lines with a width of 0.775 μm (corresponding to 645 line pairs/mm) - can be imaged clearly using both the non-coated μOIL chip and the parylene-coated μOIL chip. However, at 400 line pairs/mm and above, the parylene-coated μOIL chip resulted in a slight degradation in the optical performance as compared to the non-coated μOIL chip. As the minimum feature size of the resolution plate is larger than the anticipated maximum resolution,

we can only estimate the latter one by extrapolating the modulation transfer function until the image contract becomes zero. Using this approach, the theoretical resolution for the non-coated and the parylene-coated μOIL chip is 715 lp/mm (0.7 μm line width) and 690 lp/mm (0.73 μm line width) respectively. We should also emphasize that the obtained results are not limited by the camera resolution which was measured to be 0.15 μm/pixel at maximum magnification.

4.3.2 Field of View (FOV)

We experimentally obtained the change in the FOV of the combined system versus spacer thickness (**Figure 4.3**). The FOV was measured by imaging a commercially available grid distortion target (Thorlabs, catalog number R1L3S3P) that consists of 10 μm wide metal squares. For each spacer thickness, we obtained the one dimensional intensity profile across the grid pattern (**Figure 4.4**). The medium between the sample and the bottom glass surface of the μOIL chip is water. The intensity was uniform at the center of the ball mini-lens where minimum image distortion is observed. The FOV was defined as the diameter of an area where the intensity is above 80% of the maximum intensity. Although such a criterion is subjective, we experimentally observed that the 80% cut-off threshold was a rather conservative value for most practical application (e.g. for cell counting). For high-resolution imaging, the spacer thickness needs to be minimized (e.g. 5 μm), which results in a minimum FOV in the range of ~60μm/lens. Increasing the spacer thickness resulted in a linear increase in the FOV at the expense of resolution.

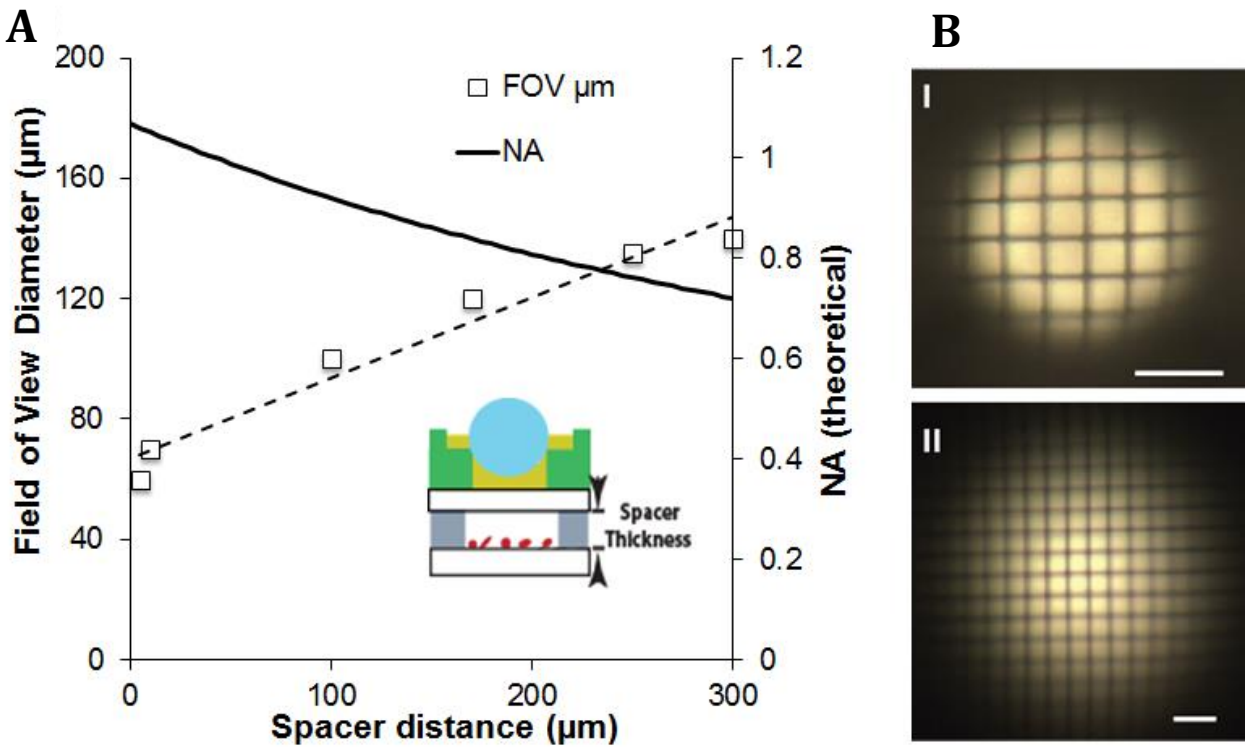

Figure 4.3: (**a**) Field of view (FOV) and NA versus spacer thickness. The theoretical NA values were calculated from thick-lens equation (see supplementary) (**b**) Image of 10 µm grid using a 5 µm spacer (I) and a 250 thick µm spacer (II). Scale bar, 20 µm in (**b**).

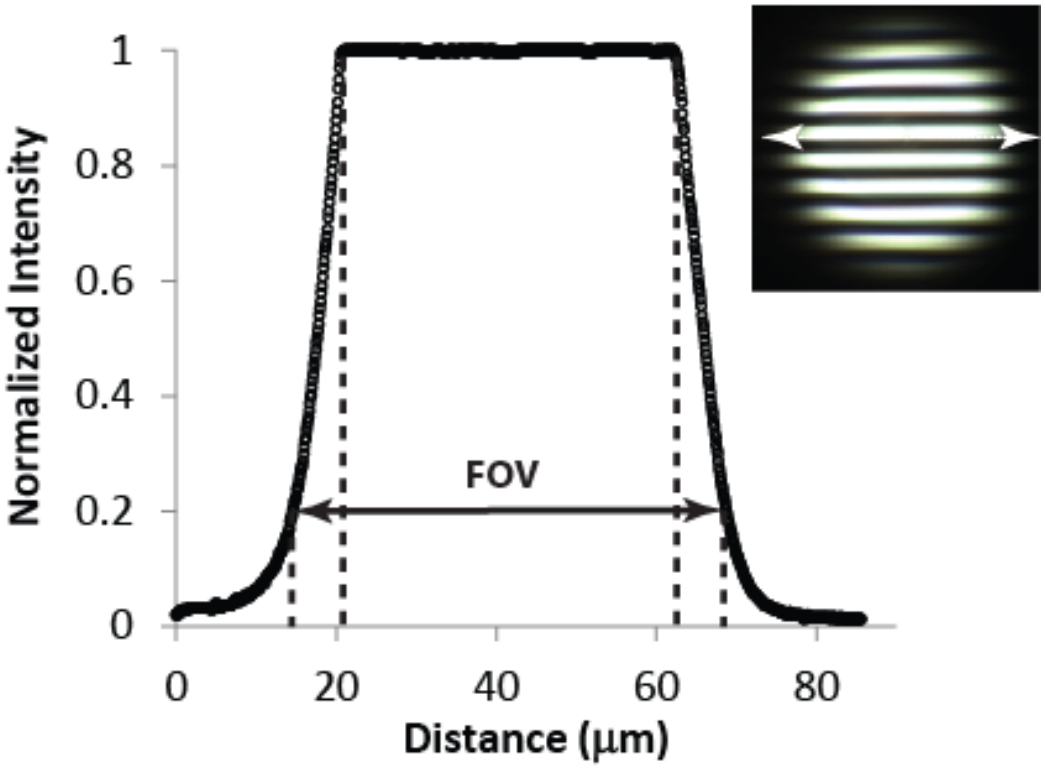

Figure 4.4: Intensity profile of a 3 μm grid pattern obtained from the combined system. The spacer thickness was 5μm. The field of view (FOV) is approximately 60 μm (where the intensity decreases by 20%).

4.3.3 Biological imaging.

In order to demonstrate the practical usefulness of the μOIL module, we imaged various biological samples using the combined system. In particular, we imaged: a whole, undiluted blood smear obtained from a patient diagnosed with sickle-cell disease (**Figure 4.5 (I) and (II)**). Cells were stained with Wright and Giemsa stain and imaged using transmission brightfield illumination (as illustrated in **Figure 4.5**). White, normal red and sickle red blood cells and platelets were clearly visible and distinguishable. If the μOIL module is removed, then the stereomicroscope alone cannot resolve single cells (**Figure 4.5 (III) and (IV)**).

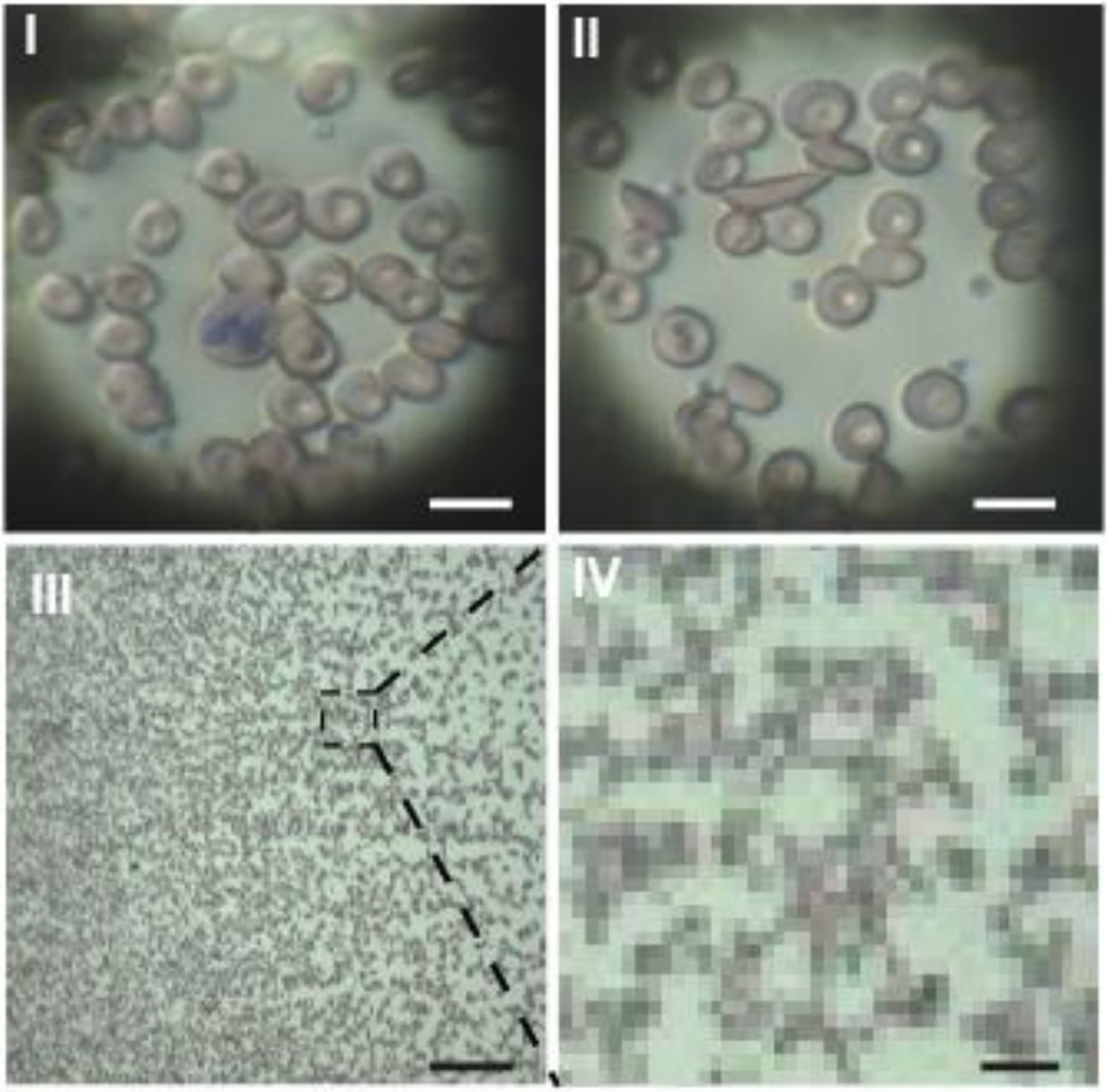

Figure 4.5: Wright and Giemsa stained blood smear from a patient with sickle-cell disease: neutrophils (I) and sickle cells (II) are clearly visible. In (III, IV), the same blood smear sample as imaged from the stereo microscope alone, Scale bars, 10 μm in I, II, IV, 50 μm in III.

In all the above experiments, the magnification of the stereo microscope was 4.5X. In this magnification, the combined system with the 1 inch CCD detector can simultaneously obtain images from 4-6 mini-lenses. To increase the FOV and image the entire μOIL chip (all 16 mini-lenses), one was to decrease the magnification of the stereo microscope to ~2X. Even in this case - the FOV is ~60 μm/lens - the shape of single cells from a smear test (**Figure 4.6**) is still visible. In order to obtain a sharp image from all mini-lenses in the array, minor focus adjustments by the stereomicroscope focus knob (~within 100 μm variation within the array) might be required as imperfections in the microfabrication and mini-lens assembly process result in a lens-to-lens variation in the focal length within the array. Our future work involves incorporate a better design of μOIL chip, better control of the fabrication process and tighter quality control assembly process to improve the focal plan uniformity of the array.

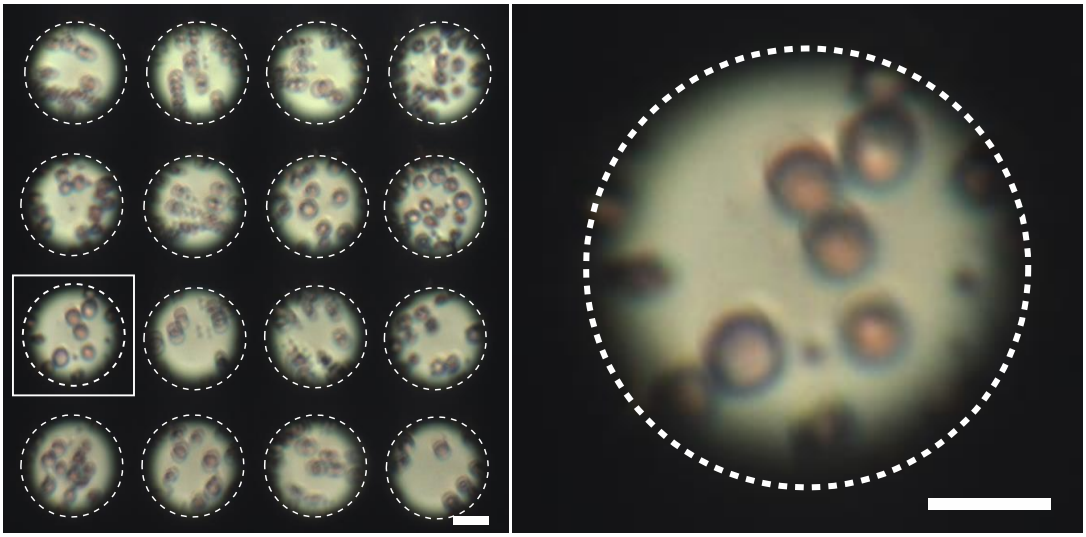

Figure 4.6: Imaging a blood smear using the entire μOIL chip (from all 16 ball mini-lens). The magnification of the stereo microscope was set to 2X. Scale bar, 20 μm.

4.4 Conclusions

We have developed an μOIL chip that can attach directly to the sample of interest and then imaged under a standard micro stereoscope by simply adjusting the focus and/or the magnification of the stereo microscope. We wants to note that the purpose of using an add-on optical module is a solution to obtain high image resolution from stereomicroscope at low cost; however, while using the add-on optical module, the large depth of field is unavoidably vanished because of the nature very shallow DOF from high resolution imaging. We demonstrated that, when it is used as an add-on module to a stereo microscope, it can resolve submicron micron features (maximum resolution of 0.7 μm) from a variety of biological samples. We believe that the μOIL chip can bring high resolution, large field of view imaging capabilities to research and medical laboratories and clinics where a stereo microscope is the only available imaging tool.

4.5 Acknowledgement

I want to thank Usha Kota and Christine Falkiewicz at the hematology lab, University of Michigan hospital for disease diagnostic training and providing sickle cell blood smear sample. I would like to thank Microfluidics in Biomedical Sciences Training Program (T32 EB005582-05) for my fellowship and research support from the National Institutes of Health (NIH) and the NIH Director's New Innovator Award (DP2OD006458).

CHAPTER 5

A point-of-care μOIL –based system for cell imaging and counting

In this chapter, we describe the development of a pocket size, lightweight, and cost effective **μOIL –based system** for bright field and fluorescent imaging. This device can be used as a generic platform for enumeration of different kinds of cells for disease diagnosis and research applications. In bright field mode, we used a white light emitting diode to generate collimated light for sample illumination. The illuminated sample was then imaged using a microfluidic oil immersion lens (μOIL) module that was positioned directly under the CMOS camera. Adding excitation, emission filters and a condenser lens to the bright field setup, converted the μOIL microscope to a fluorescence imaging microscope. We characterized the performance of this μOIL imaging system by counting red blood cells (RBC) and human leukemic monocyte THP-1 cells via image analysis software over a field of view (FOV) of ~0.64 mm^2. Furthermore, we demonstrated the μOIL system's potential for clinical use by imaging sickle red blood cells, *P. falciparum*-infected and *P. vivax*-infected RBCs in brightfield mode and human leukemic monocyte THP-1 cell samples in fluorescence mode with LED excitation. The resolution of the μOIL imaging device was found to be 0.43μm by imaging 0.05 μm fluorescent beads. Weighing less than 40 grams, this compact and cost effective μOIL imaging device can be useful for point of care settings by providing an important tool for disease

diagnosis, screening and quantification of various lab-on-chip assays developed for global health applications such as cost-effective monitoring of blood cells.

5.1 Innovation

Combining the optofludic chip with a CMOS image sensor and LED light source to make an integrated digital microscope weighing less than 40 grams and fitting into the palm of one hand, providing submicron resolution in brightfield and fluorescent imaging modes while having a large field of view.

5.2 Introduction

Although microscopy was invented more than four centuries ago, it remains the leading imagining equipment and gold standard for several biological and biomedical analyses. Numerous new methods have been developed in the field of microscopy such as fluorescence, phase contrast, dark field, confocal and differential interference contrast microscopy. Introduction of super resolution microscopy has taken optical imaging to dimensions less than the optical diffraction limit. The importance of this new development in imaging is illustrated by the 2014 awarding of a Nobel Prize to Eric Betzig, for super-resolved fluorescence (high-resolution lattice light-sheet) microscopy.

In the last 15+ years optical microscopy on lab-on-a-chip systems and microfluidics have emerged as powerful fields with high potential for healthcare applications[140]. Using lab-on-a-chip concepts, numerous tasks can be done in miniaturized systems including study of cell mechanics and sensing, cell and tissue culturing, cell separation and sorting, cell lysis, DNA and RNA amplification. The driving force behind miniaturization is the cost of reagents and/or small quantity samples. Also lab-on-a-chip devices make it feasible to study single cells, which could not be done in the past. Even though these lab-on-a-chip systems have accomplished

extraordinary levels of integration, obtaining the images of processes on lab on chip devices is still accomplished mostly through conventional microscopy in the laboratory[141]. This limitation can impact both the design and use of lab-on-a-chip devices targeting point of care for diagnostics, bedside testing and field applications.

During the past decade, various optofluidics imaging methods for lab-on-a-chip systems have been developed to substitute for bulky conventional microscopy such as lensless holography[94]–[96], [142], shadow imaging[85], [86], [143], and optofluidic microscopy (OFM)[90], [106], [141], [144]. The lensless holographic microscopy uses coherent light source to illuminate the sample. This method was successfully implemented for wide field of view (equal to the whole camera chip area) on-chip imaging application. One practical drawback of these systems is that very small sized pinhole is likely to get blocked by dust or particles easily. Moreover, proper adjustment of a pinhole to a focused laser beam requires expensive high precision optical and mechanical elements. Another lensless approach is using incoherent shadow imaging. This method captures shadow images of the object and partial non-coherent diffraction[82]. As a result, these captured shadow images are not identical to the object itself but represent a spatial characteristic signature of it (finger print)[145]. The shadow imaging is also referred to as contact imaging where the color filters and the microlens arrays are removed from CMOS imaging sensor chip so that the sample can be seeded directly onto the sensor surface (~0.9 μm away) in order to obtain vertical distances acceptable for microscopy purposes[89]. Another optofluidics imaging approach is through introduction of small pixel size sensor arrays with a pitch of ~ 1μm with a linear array of circular apertures fabricated directly on the sensor array[90] This approach requires that the samples be in a steady flow passing in front

of each aperture. Signals from the same object need to be captured several times to reconstruct the image off line[90], [107], [146].

In this chapter we used the novel μOIL chip described in the previous chapters together with CMOS image sensor and LED light source and demonstrate its use as a standalone imaging system for a number of different biomedical applications. First we show integration of the μOIL imaging device, next we characterize the performance of it by imaging 0.05 μm fluorescent beads to find the lateral resolution. Then, we demonstrate red blood cell (RBC) counting[147] and human leukemic monocyte THP-1 cell counting at different concentrations. We use computer-assisted automated counting of THP-1 cells via image analysis software (MATLAB). We later validate the capability of μOIL imaging device for clinical diagnostic use by imaging blood smear of sickle cells anaemia and malaria's patients. We also demonstrate the capabilities of the μOIL imaging device for fluorescence imaging.

5.3 Methods

5.3.1 Design Requirements

The handheld, point-of-care μOIL imaging device is designed with point of care applications in mind with smaller size, weight and low power consumption no more than the current mobile phones. In addition to be successful in point of care applications it should have enough resolution to image human blood cells which usually ~ 6-10 μm. The device also needs to be compact with no moving parts, simple to use with minimum adjustment and compatible with lab-on-a-chip systems. Finally the device parts must be mass producible in order to be cost effective and available worldwide. Starting with the criteria above, we developed a handheld

device following the guidelines of simplicity in design so that the μOIL imaging device can be further optimized for future point of care application.

5.3.2 Imaging System

The handheld μOIL imaging device comprised of (i) an array of Microfluidic-based Oil Immersion Lenses (termed 'the μOIL chip'), (ii) a low cost 5MP CMOS sensor (2.2 x 2.2 μm pixel size) (iii) a collimated LED and, (iv) a microfluidic chip. A custom-made plastic housing was manufactured to secure all those components in place except the specimens or the microfluidic device that is manually inserted into the housing from the side. The specimen is illuminated by the LED from below. The transmitted light is collected by the high numerical aperture (NA) lenses of the μOIL chip and focused on the CMOS sensor that is placed 3-4 mm above the μOIL chip (Fig. 1(i)). To achieve a sharp, well-focused image, the exact distance between the μOIL chip and the CMOS sensor is manually adjusted using a set of fine threaded screws. Finally, the CMOS sensor is connected to a computer that acquires and analyzes the image.

The first prototype of μOIL imaging device (**Figure 5.1:A(ii)**) was approximately 7 cm in diameter and 5 cm height. While, the μOIL chip's size is only 1cm x1.2 cm x 1mm, the standard specimen glass slide is 2.54 cm x 7.6 cm x 1 mm. The housing was designed to have a larger base, 7cm in diameter, to accommodate the sample slide and the LED holder which was 6cm in diameter.

For diagnostic or cell counting purposes, the sample slide can be inserted under the μOIL chip. To achieve a good contact between the μOIL chip and the specimen samples (and therefore eliminate any gap between them), a flexible cable is used as a spring to push the μOIL chip

against the coverslip. As a result, the distance between the μOIL chip and the sample is always fixed (**Figure 5.1B**).

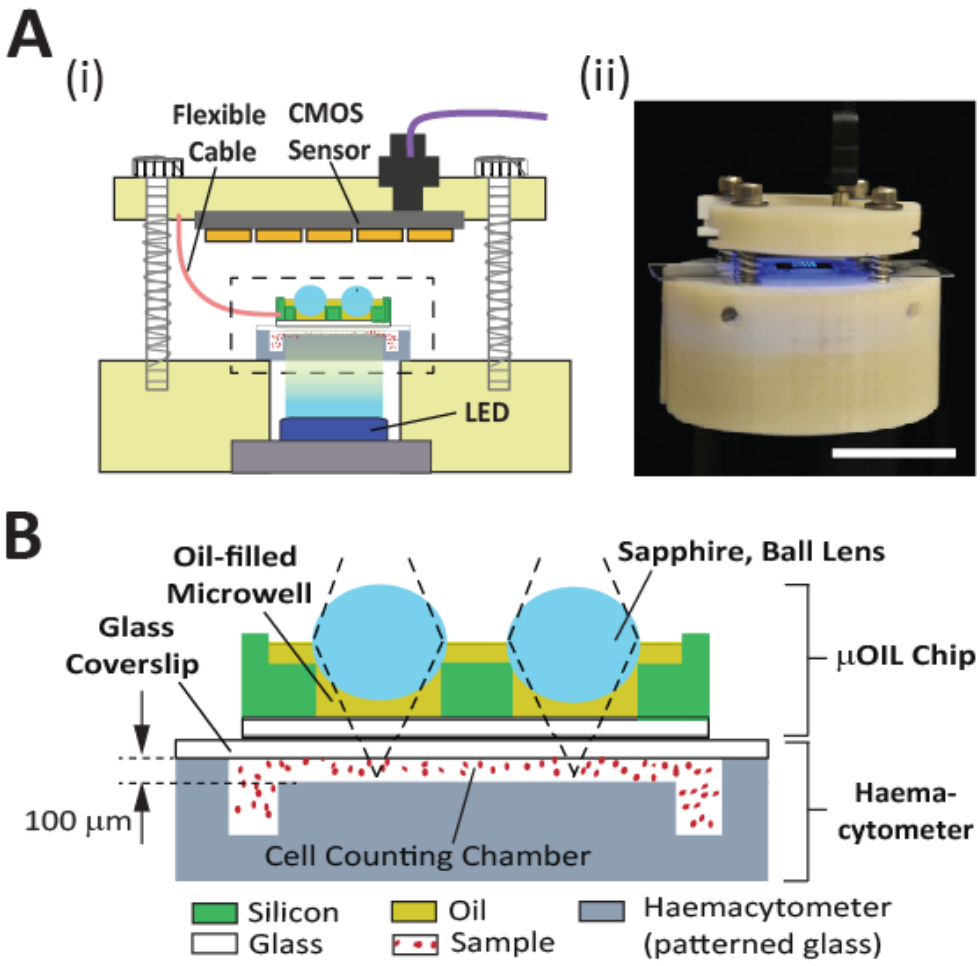

Figure 5.1: The working principle of the handheld optofluidic μOIL microscope.
A(i) The schematic cross-section of the optofluidic μOIL microscopy\e (not to scale). The μOIL chip is sit on top of a microfluidic chip (haemocytometer).
A(ii) Pictures of the optofluidic μOIL microscope. For cell counting, CMOS sensor (monochrome) and Blue LED (470nm) can be used. Scale bar in (ii), 3 cm.
B Details of μOIL chip on top of microfluidic sample. The sample is placed at the focus point of each lens and image is captured to CMOS sensor

The μOIL chip consists of 16 sapphire, ball lenses (1 mm nominal diameter, refractive index of 1.77) placed in a 4x4 array of oil-filled microwells. The oil/ball lens assembly forms a doublet lens and resembles the hemispherical front lens of an oil-immersion objective (**Figure 5.2**). Details of fabrication and assembly this μOIL chip is described in the previous chapter.

Figure 5.2: μOIL chip (1 cm x 1.2 cm) on US penny (A) and the μOIL chip/ haemocytometer assembly (B). Scale bars, 1 cm in A,B.

The second prototype of μOIL imaging device is demonstrated with a smaller size of 4cm x4cm x4cm and lighter weight (40 grams) compared to the first prototype. The optofluidic μOIL microscope configuration remains the same, starting from top down (**Figure 5.3A**); CMOS sensor, μOIL imaging chip, microfluidic chip, a collimated LED. Both CMOS sensor and μOIL imaging chip are fixed on the top holder at a fixed 4 mm distance away from each other, giving an optical magnification of ~17x when the sample is at its focal plane. Four screws at each corner of the top holder are used for adjusting the gap between the μOIL chip and the sample. The bottom holder has a recess made to fit the glass sample slide. When the sample slide is inserted, it will slide along this recess and be placed under the μOIL chip with the same gap (**Figure 5.3B**). LED, battery holder and 3V battery are stacked on top of each other and are placed in the bottom plastic holder.

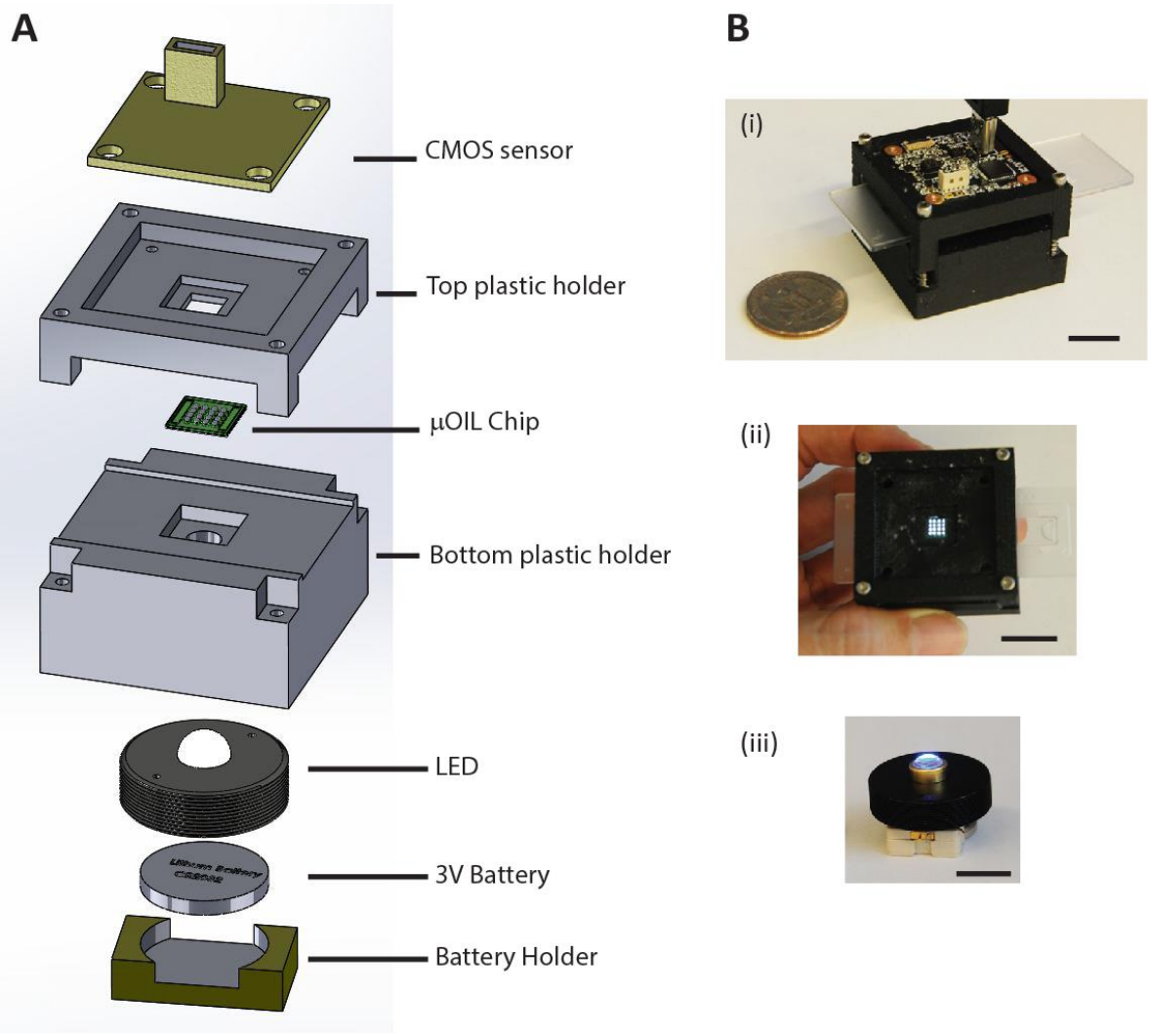

Figure 5.3: The second prototype optofluidic µOIL microscope (A) The exploded view of the illumination and detector units. (B) (i) side view, (ii) top view of µOIL microscope without CMOS sensor. Optofluidic µOIL microscope comprises only a few small-sized and cost-effective components resulting in a handheld and simple configuration designed for point-of-care imaging in bright field. (iii) LED light staging on top of 3Vbattery and battery holder. Scale bar: 1 cm in B

To transform brightfield µOIL imaging device to fluorescence mode, three additional parts are employed, arranged in trans-illumination configuration (**Figure 5.4**). An emission filter (Pixelteq,5mm x 5mm x 1mm) is added to top holder right under CMOS display, an excitation filter is added to the bottom holder above the LED light path allowing light at a specific

wavelength illuminating through the sample. An aspheric condenser lens (Thorlabs, ACL1210) is inserted above the LED, focusing LED light onto the sample. An alternative configuration is with a blue/violet diode laser without the excitation filter.

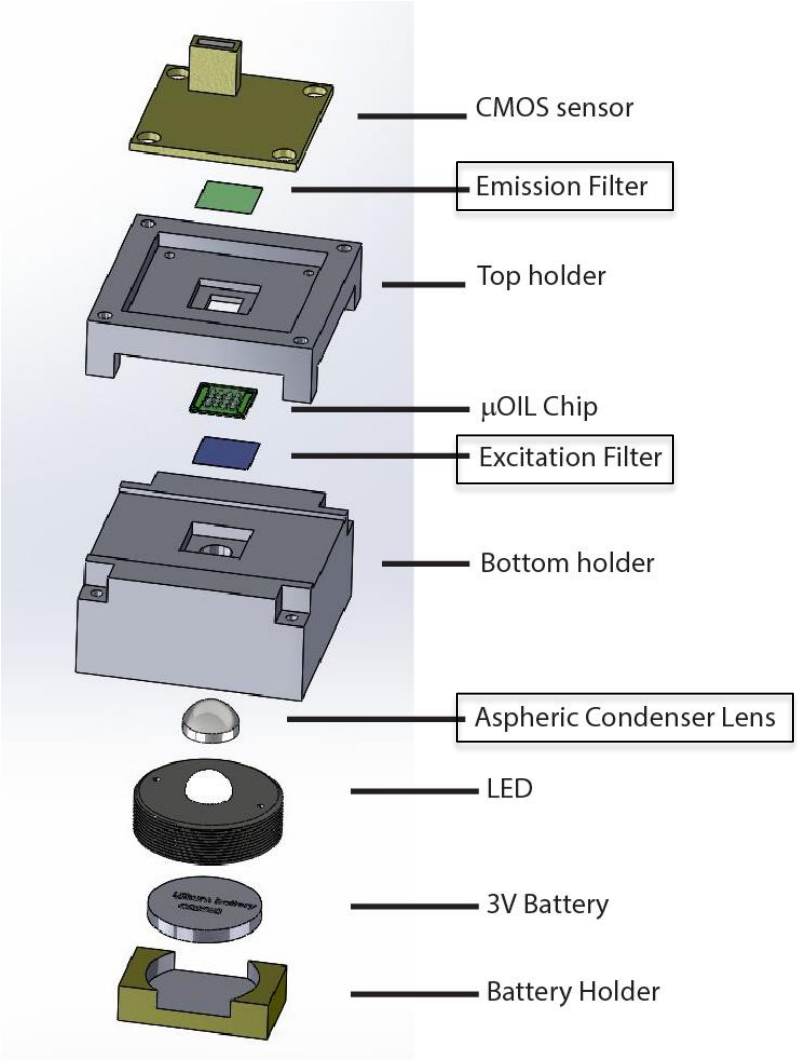

Figure 5.4: The exploded view of the fluorescence μOIL microscope. Three additional parts (Condenser lens, emission and excitation filters) are added into the bright field μOIL microscope turning the system into fluorescence mode.

5.4 Sample preparation

5.4.1 Liquid blood samples for counting cells

Whole blood samples from healthy patients were obtained from the Hematology laboratories, department of Pathology, University of Michigan Health System. The samples were diluted in Phosphate-buffered saline (PBS) at different dilution factors to demonstrate Red Blood Cell counting (RBC count).

For cell counting experiments at different concentrations, THP-1 cells which are round large human monocytic cells, were cultured and used as the representative of white blood cells.

5.4.2 Blood smear samples for cell imaging

Blood smear samples were obtained from two different sources. For Malaria thin/thick blood smears, the specimens were prepared at the department of diagnostic laboratory unit, the Tropical of Disease Hospital, Thailand. For Sickle cell anemia and other thin blood smear diagnostics, the specimens were prepared by the Hematology lab, department of Pathology, University of Michigan Health System

Preparation of blood smears and stains:

Blood smearing is a method of blood sample preparation on a glass slide to spread blood cells all the way to single cell layer such that it can be inspected under a microscope by a professional. Often, blood smears will be stained with different chemicals to color the periphery of the cells (Wright's stain), nuclei of cells (H&E stain) or chromosomes (Giemsa stain) in order to increase the contrast of the object of interest under microscope. The blood smear samples in this work are prepared and used for demonstration of diagnosis of sickle cells anaemia and malaria diseases.

5.4.2.1 Protocol for Preparing Blood Smears:

I. For thin smears, prepare at least 2 glass slides (1in x3 in). One slide is used for the blood sample and the second slide is used to smear the blood (spreader slide)

II. Place a very small drop of human blood on the edge of the glass slide (specimen slide).

III. Place the short side (1") of the spreader slide directly on the blood, let the blood spread across the short slide, held at 30-45 degree angle relative to the specimen slide and smear across the drop of blood rapidly and smoothly.

IV. The smear should end before the length of the specimen slide and show in a "feathered edge" where the blood cells are well spread. This is the useful area for inspection.

V. Let dry for 10 minutes

VI. Fix the film by dipping the specimen slide in 100% methanol 1-2 times, each time for a few seconds, let dry for 3 minutes

VII. Stain the specimen slide with Giemsa Stain (VWR product#1.09204.0500) to stain. Malaria Parasites.

a. Drop Giemsa's staining solution on the specimen slide for 10 minutes
b. Wash with PBS buffer (or DI water)
c. Air dry

VIII. Stain specimen slide with Wright's Stain (Fisher HealthCare, product# 23-264-983) to stain peripheral blood:

a. Drop Wright's stain on the specimen slide for 6 minutes
b. Wash with Wright's stain buffer (or DI water) for 1.5 minutes
c. Air dry

5.5 Counting cells

We performed RBC and THP-1 cell counts on a commercial haemocytometer (Hausser Scientific) slide covered with a 150 μm thick glass coverslip (Fig. 5A). The Neubauer chamber of the haemocytometer has a total volume of 6-7 μl and it has a square grid pattern to facilitate the cell counting (**Figure 4.5B**).

5.5.1 RBC counting

Blood samples (~10 μL in volume, diluted by a factor of 50, 100 and 200) were pipetted into the haemocytometer and driven in the Neubauer chamber by capillary action. Images of the blood samples were captured from 5 different 200 μm x 200 μm square areas in the grid pattern of the Neubauer chamber (marked as dark blue boxes in **Figure 4.5B**). The dilution and imaging procedures used in our experiments are the recommended ones for haemocytometer-based RBC counting [148]. To image the haemocytometer and count the RBCs, we used: (i) a microscope (Olympus-BX51WI) in epi-illumination mode with a 50x objective (NA=0.5), connected to a 5 MP digital camera and, (ii) our compact imaging system with a field of view (FOV) of 200 μm diameter and a NA of 0.54. In this case, the distance between the cells and bottom surface of the μOIL chip was ~250 μm (RBCs tend to settle at the bottom of the Neubauer chamber). In all RBCs imaging experiments, we used a single lens from the μOIL chip for consistency in the image quality.

5.5.2 WBC counting

As mention before, we use THP-1 monocyte in place of WBC. The THP-1 cells are cultured and prepared at 200 – 8000 cells/μL in order to cover the complete range of white blood cell concentrations in humans. With the microscope counting experiment, we counted cells that

were inside the four of 1x1mm grid pattern of the Neubauer chamber (marked as yellow boxes in **Figure 5.5C**). This is the same method for counting WBCs in whole blood. In this set of experiments we utilized all 16 lenses of the μOIL chip to image and perform cell counting on 0.64mm^2 surface area (16 lenses x200x200 μm^2) **(Figure 5.5C)**. μOIL lenses are placed in 4 x 4 arrays, spaced 515 microns center to center in both x and y directions. Automated counting software (MATLAB) was used to crop and assist in cell counting on images captured by the μOIL chip. At each concentration, we obtained 4 different sets of microscope-based and 10 different sets of μOIL system-based counts in order to improve the statistics at the low end of the cell concentrations.

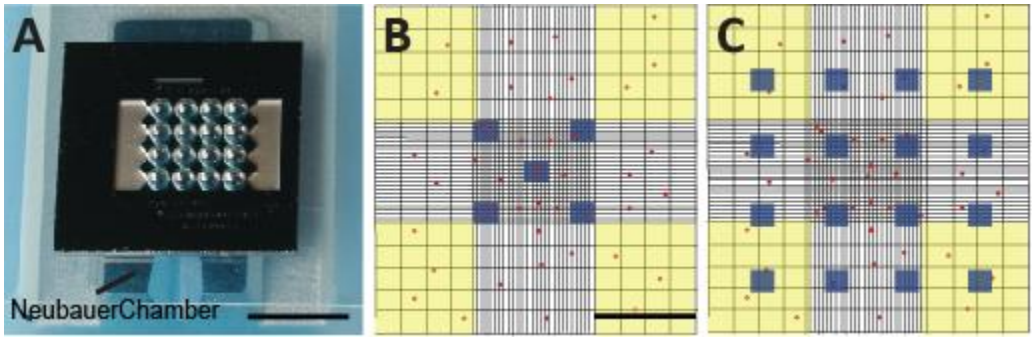

Figure 5.5: (A) The μOIL chip on top of the Neubauer chamber. Scale bar, 4 mm. (B) Schematic of the grid pattern that sits beneath the μOIL chip. The dark-colored boxes are 200 μm x 200 μm and represent the 5 regions where RBCs are counted, the yellow-colored boxes are 1mmx1mm which represent the 4 regions where THP-1 cells are counted under microscope counting experiment (C) The dark-colored boxes are 200 μm x 200 μm and represent 16 regions where THP-1 cells are counted under μOIL system. Scale bar: 5 mm in A, 1 mm in B.

5.6 Result and Discussion

5.6.1 Resolution of the μOIL imaging system

A good approximation of the possible resolution of the μOIL imaging system is the full width at half maximum (FWHM) of the point spread function[149]. The optical resolution of the μOIL chip was investigated by imaging 50 nm diameter fluorescent microspheres (441/486 nm, Polysicences Inc.) with μOIL imaging system setup in trans-illumination mode. The emission filter (505nm) and excitation filter (470nm) were used. Microspheres were fixed to a glass specimen slide and placed under the μOIL chip at the focal point with an oil interface in between at a magnification of ~17x. To determine resolution values, lateral intensity profiles of the microsphere images were plotted across the beads and fitted to Gaussian curves to obtain a best fit of $f(x) = 1.04exp^{(-\frac{x}{0.26})^2}$ (shown in **Figure 5.6**). The full-width-at-half-maximum (FWHM) of the Gaussian function was found to be ~ 430nm±20nm.

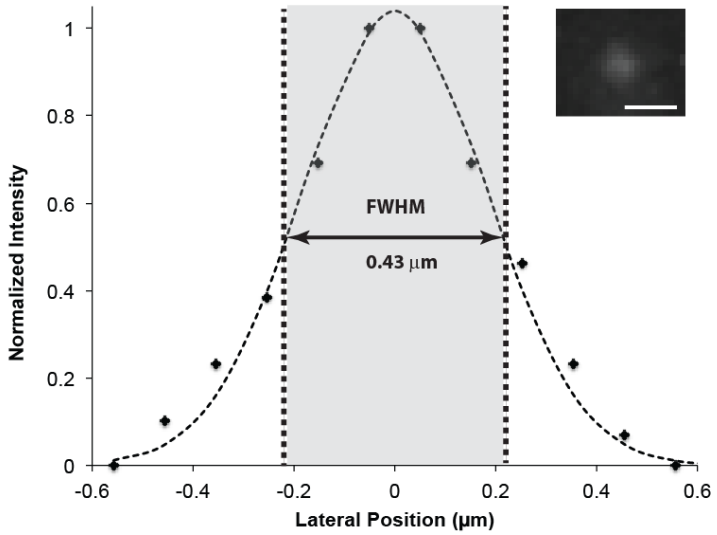

Figure 5.6: A Gaussian plot of a 50nm fluorescence microsphere resolution of μOIL chip. scale bar 1 μm

5.6.2 Field of View (FOV)

For cell counting applications, the FOV of each lens in our system is an important feature as it determines how much blood volume (and therefore how many cells) can be imaged. The FOV in our system can be modified by changing the distance between the bottom surface of the µOIL chip and the sample. To estimate that dependence, we used the grid pattern of the Neubauer chamber as a reference sample, placed it at 100, 150, 175 and 200 µm below the bottom surface of the µOIL chip and measured the corresponding FOV. We used glass coverslips of different thicknesses to vary the sample/µOIL chip distance. We also performed optical simulations in OSLO software to estimate the corresponding resolution (**Figure 5.7**). As expected, the larger the sample/µOIL chip distance the larger the FOV and lower the resolution. For our RBC cell counting experiments as explained earlier, we selected a FOV of ~200 µm as it matches the standardized, 200 µm x 200 µm imaging area of the Neubauer chamber (depicted in **Figure 5.5B**). The resolution and NA in this case were estimated to be 0.53 µm and 0.54.

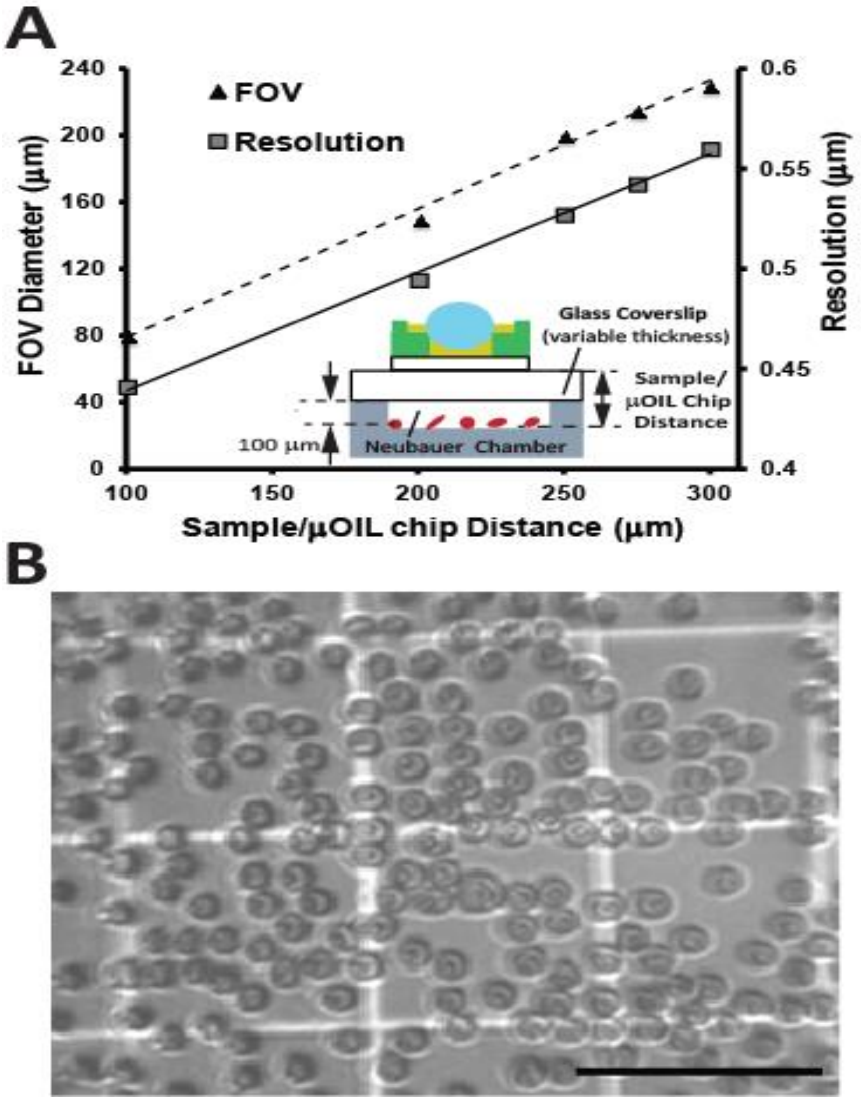

Figure 5.7: (A) FOV and resolution versus sample/µOIL chip distance. The FOV is the diameter of the area that a single sapphire lens can visualize.
(B) An image of RBCs as captured through our system for a sample/µOIL chip distance of 200 µm. Scale bar, 50 µm.

5.6.3 Comparing RBC counts

We obtained images from diluted whole blood samples with our system and with a microscope (**Figure 5.8A**) as described earlier. In both cases, we used a haemocytometer with a 150 µm thick glass coverslip. We noticed that, although the NA of the µOIL system and the

microscope are similar (0.54 versus 0.5), the μOIL system could resolve details of the cell geometry/size much better than the microscope (**Figure 5.8B**). The biconcave RBC shape with the characteristic dimple in the middle was clearly visible. We believe that the main reason for such a difference on the image quality is due to the high contrast that is generated by the bright-field illumination of our system. We also noticed that the sapphire lens of μOIL system distorts the edges of the viewing area. That effect did not alter the RBC counting results, as cells are still identifiable.

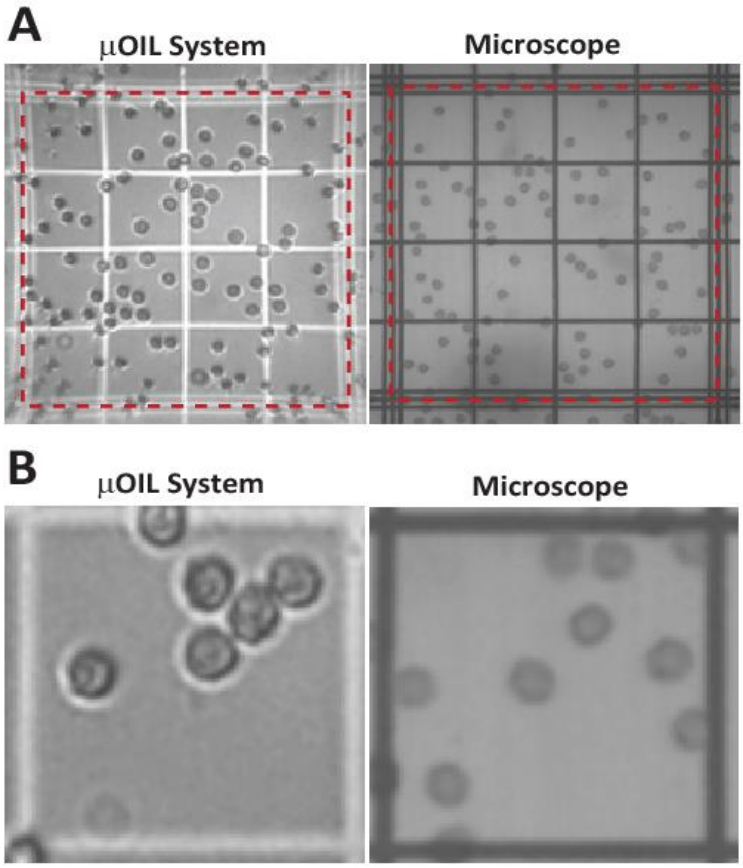

Figure 5.8: (A) Diluted blood samples as imaged through μOIL system in transmission mode (NA=0.54) (left) and a microscope in reflection mode with 50x (NA=0.5) objective (right). (B) Magnified images from a single 50 μm x 50 μm square of the grid containing RBCs. The dimple of the RBCs is visible with the μOIL system.

We furthermore performed imaging experiments with blood samples diluted by three different factors (50, 100 and 200). For all 3 dilution factors, we did not observe any significant differences between the RBC counts obtained with the microscope and our system.

We also compared μOIL system with a flow cytometer which is considered the gold standard for cell counting applications. The flow cytometer count was 4.57 million cells/μL (see dotted line in **Figure 5.9**, no dilution). The average count obtained from microscopy was 4.27± 0.2 and the average of count from the μOIL imaging system was 4.37± 0.2. The RBC count from our system is in good agreement with the flow cytometer results within one standard deviation for dilution factors of 50 and 100. RBC counts with larger (e.g. >200) dilution factors are not recommended as there is a significant difference (~10% error) between the flow cytometry and μOIL system results. However, standard haemocytometer-based RBC counting procedures recommend a dilution factor of 200 to facilitate the manual counting process. We should also note that despite the fact that we used whole blood, the presence of white blood cells (WBCs) does not affect the RBC count as WBCs make up only 0.1% of the total number of cells in blood and as a result they rarely appear in the images.

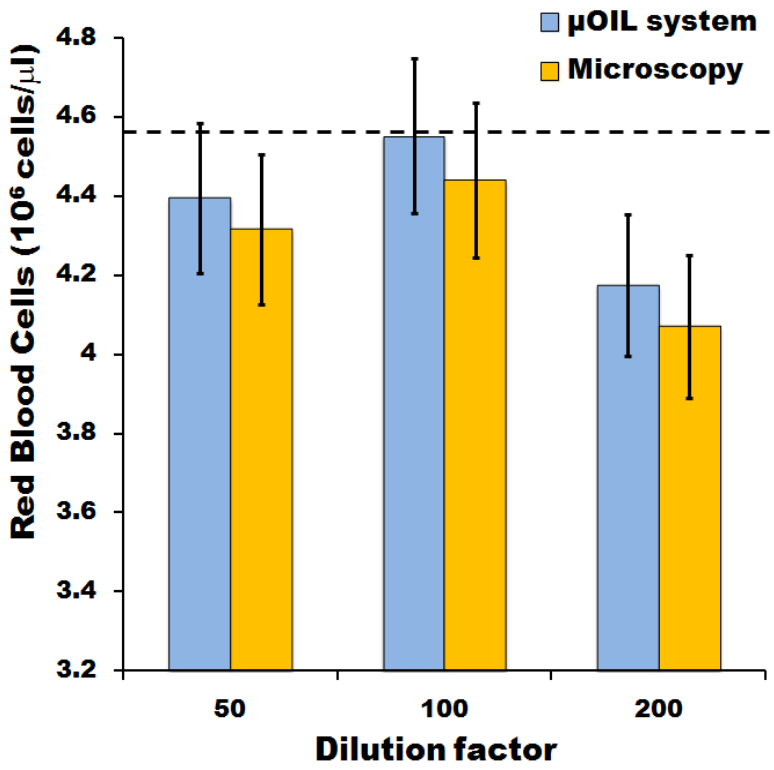

Figure 5.9: Comparing RBC counts. The dotted line is the RBC count (4.57x106 cell/mL) as measured by flow cytometry. The error bars represent one standard deviation.

5.6.4 Comparing monocyte THP-1 cells (represent White blood cells):

We obtained images from diluted whole blood samples with µOIL system and with a microscope the using the same method we counted RBCs. We also used a haemocytometer with a 150 µm thick glass coverslip. However, instead of using only one lens of the µOIL system, we utilize 16 ball lenses on the chip to obtain highest possible area we could count. The images of monocyte THP-1 cells that captured by the µOIL system (figure 10A) are imported to Matlab program and to count the cells (**Figure 5.10B-10D**). Even though white blood cell (WBC) concentration in healthy adults range from 4500-10000 cells/µL, we prepared different dilutions of monocyte THP-1 cells from a concentration as low as 200 cells/µL – 8300 cells/µL to cover

two different ranges of interest. The upper range covers the healthy adult WBCs and neutrophils, which range from 2500-7500 cells/μL. The lower range covers specific types of white blood cells such as CD4 T *lymphocyte* (CD4+ T cells) or neutrophils. CD4+ T-cells play a crucial role in the immune system and the concentration of these cells in HIV patients is a measure of the health of the patient. Typically, the CD4 count of a healthy adult range from 500 – 1200 cells/μL.

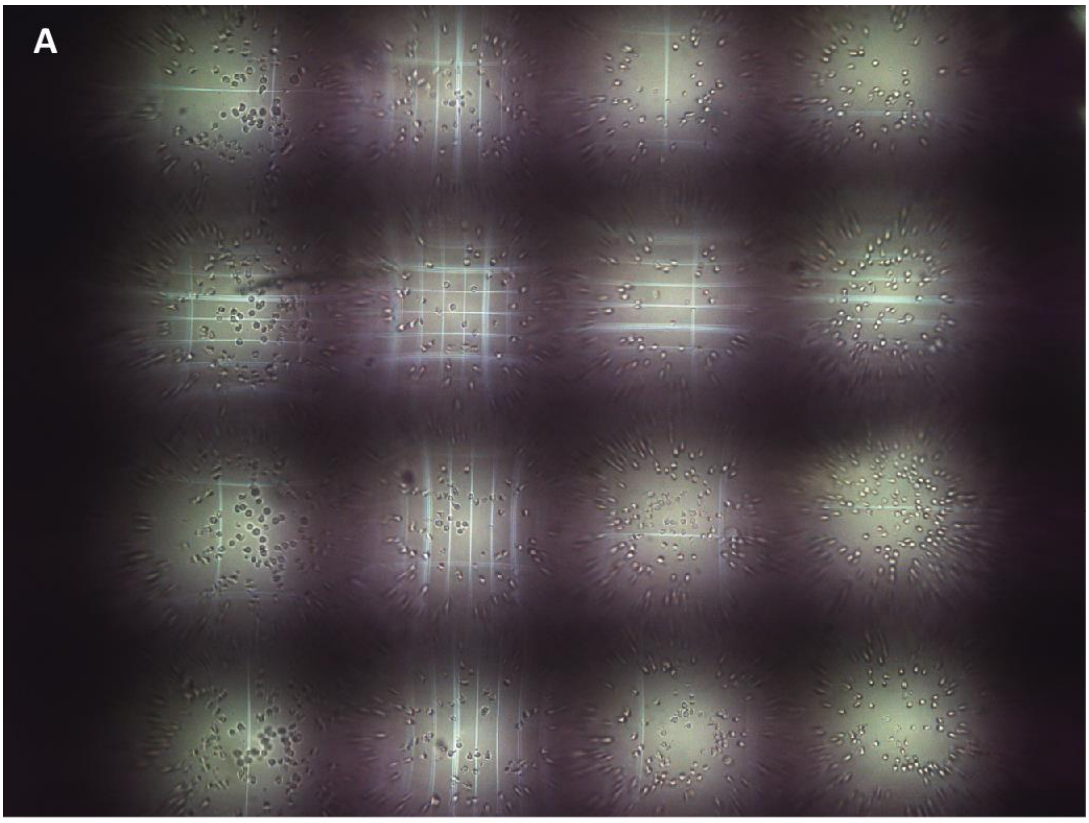
A

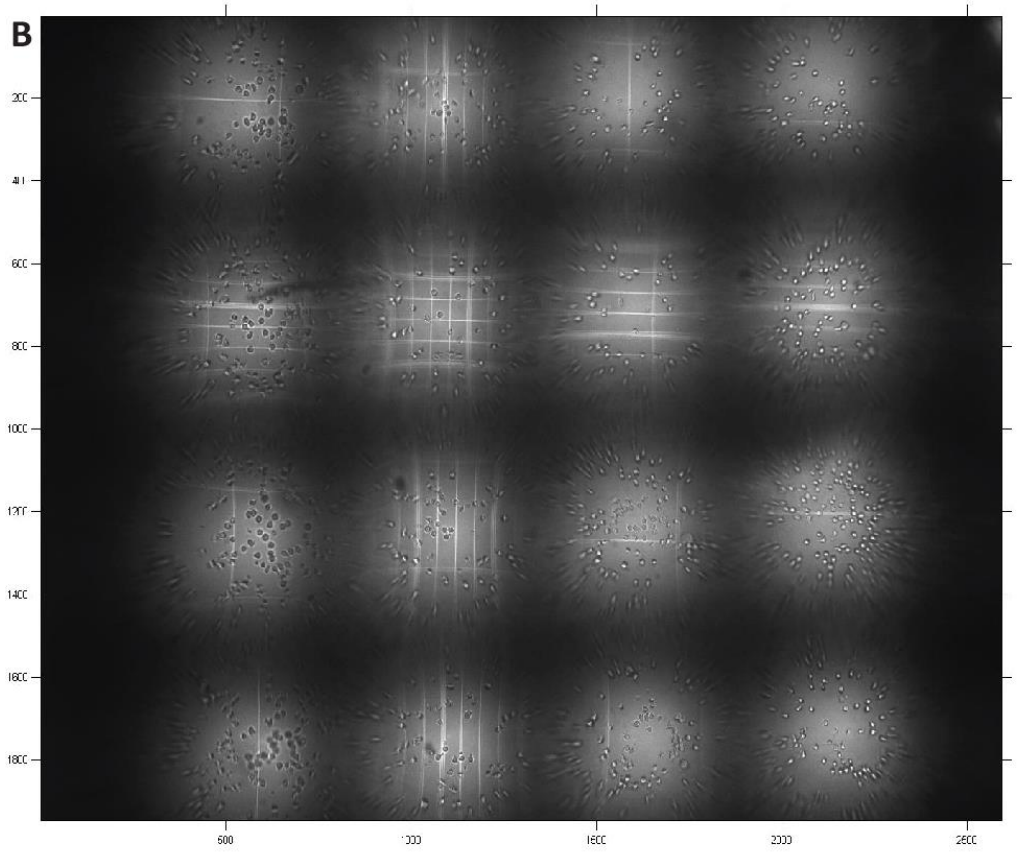
B
200
400
600
800
1000
1200
1400
1600
1800
600
1000
1400
2000
2600

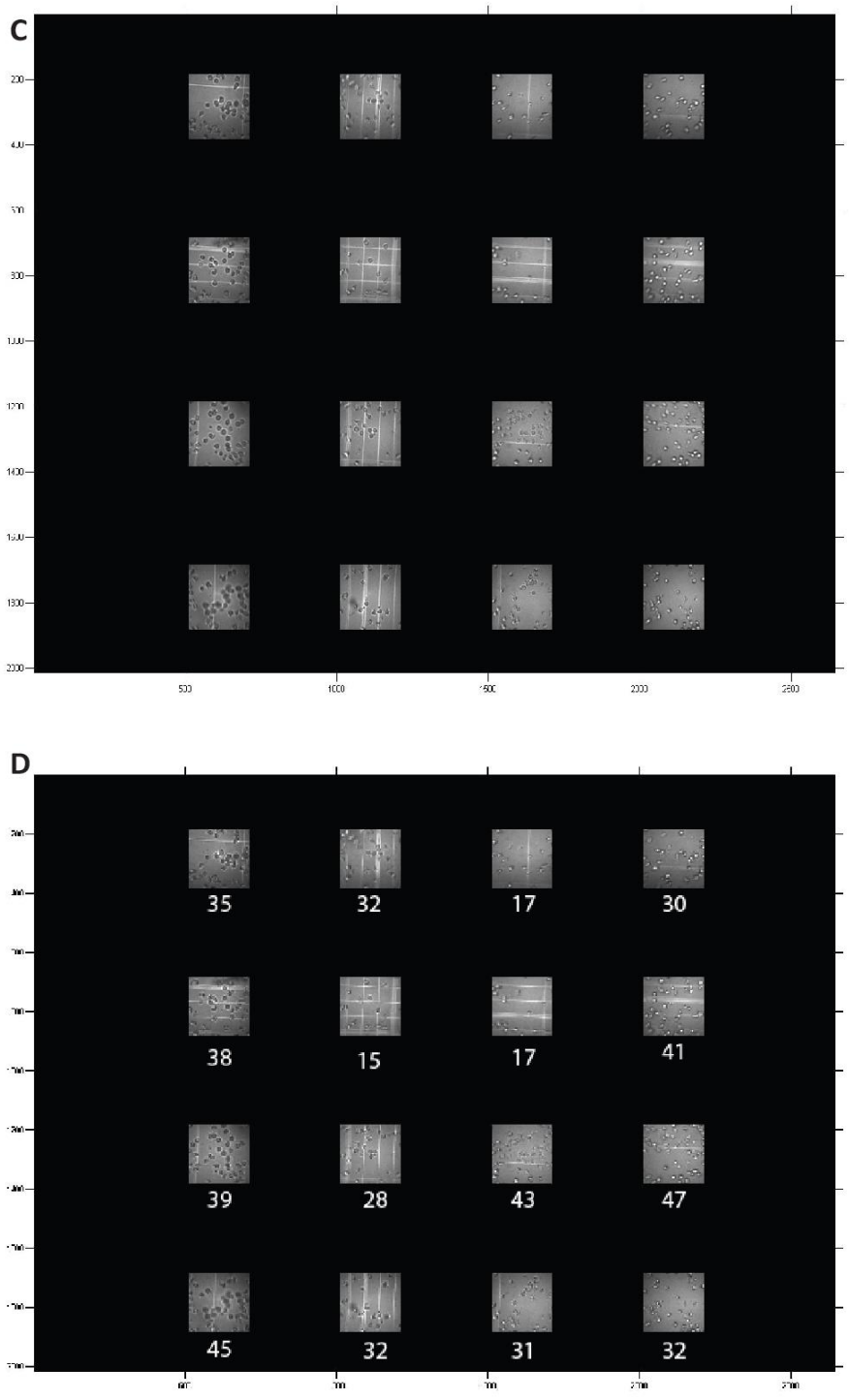

Figure 5.10: (A) An example raw image of monocyte THP-1 cells of ~8000 cells/μL captured by μOIL system (B,C,D) Same image is imported to Matlab softward assist cell counting to perform 16 lenses 200 μm x 200 μm cropping area according to lens' position in μOIL system and counting.

We averaged 4 different sets of cell counting using microscope-based method and 10 different sets with μOIL system method in order to increase the counting accuracy as much as possible. By counting approximately equal total number of counts by both instruments, we can compare the accuracy of both methods side by side for the concentration range of 200 cells to 8300 cells/μL (**Figure 5.11**).

Comparison of the THP-1 cell counts between the automated counting with 16 lenses of the μOIL measurements and the microscope measurements are shown in **figure 5.11**. We see that there is excellent agreement between the two methods of counting the number of cells in the same sample. Recommended minimum number of counts per square for having a reliable estimate of the actual cell white blood cell concentration for the hemocytometer at least 50 cells per square. For the μOIL chip this corresponds to an average of 3+ counts per lens. However with 50 counts only the statistical counting error is $\sim(50)^{0.5}$ =7.07=14% with ten different measurements a better estimate of the actual counts can be obtained by averaging the ten measurements and the standard error on the mean which is reduced to 10.9%. For both the μOIL counts and the microscope measurement, at the very low end of 200 cells/μL the error in the estimated cell concentration from sample measurements increases all the way to almost 25%. When the cell counts are above 1000 cells μL the measurements are quite accurate estimating the actual concentration with a standard error of 10% or less.

If we want to improve the statistics further we can increase the number of ball lenses further. In our current set up the main limitation was the size of the CMOS sensor ~5.76x4.29 (24.70 mm^2). With a half inch CMOS sensor the number of lenses can be increased three to four

fold enabling imaging of a much wider field of view and thus count three or four times more cells and reduce the variance by a factor of two.

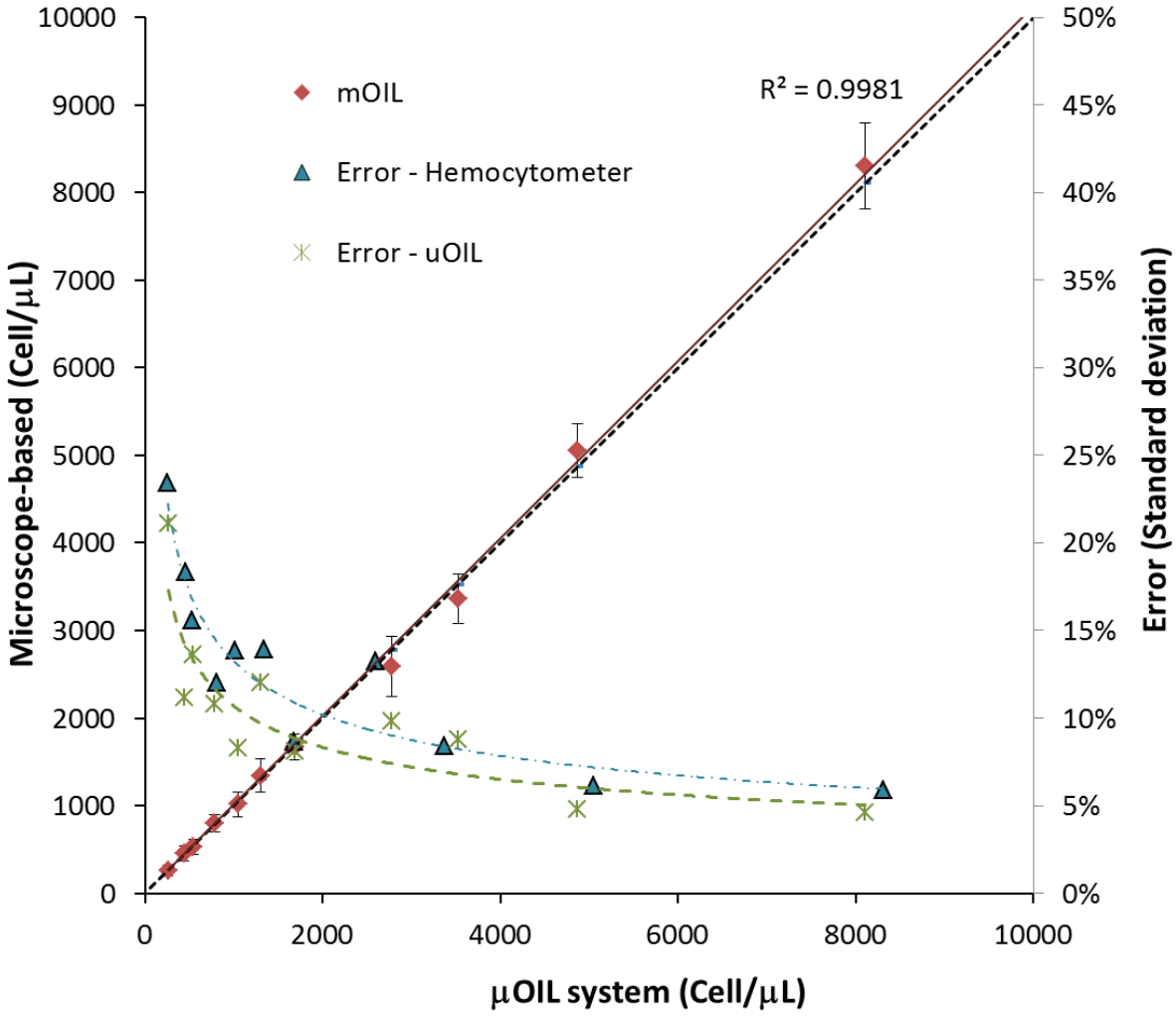

Figure 5.11: Comparison cell counting using Microscope-based vs µOIL system based to capture imaged and count cell concentration. The error bar on the right show error obtains at different cell concentration.

5.6.5 Diagnostic tool for biological specimens

Color imaging is an essential function for a diagnostic tool in order to differentiate structures of the biological specimens. We changed the monochrome CMOS sensor in to a color sensor in the μOil microscope for imaging stained samples. The resolution of the color CMOS is less than the monochrome CMOS, however, we believe the high resolution of μOIL chip compensated for the lower pixel resolution of the color sensor and resulting in adequate resolution for diagnosis purposes. **Figure 5.12** shows the result from the μOIL imaging and the comparision imaged from the microscope. We used the color μOIL system to image *Plasmodiun vivax* and *Plasmodium falciparum* malaria parasites, white blood cells and sickle cell anemia red blood cells from blood smear specimens. The morphology of *Plasmodiun vivax* is rough small dots in pink color (Schuffner's dots) in the cytoplasm of red blood cell and the size of the infected red blood cells increase by 1.5 times compared to normal red blood cells (**Fig. 5.12 A,B**). The morphology of *Plasmodium falciparum* malaria parasites is a crescent form microgametocyte with purple chromatin (**Figure 5.12 C,D**). The abnormally sickle shaped of red blood cells (**Figure 5.12 E,F**). While these images revealed the presence of abnormal of red blood cells, the μOIL system can also verify the type of white blood cells; monocyte in **Figure 5.12A**, Neutrophil in **Figure 5.12 C**, Eosinophil and Lymphocyte in **Figure 5.12 E**. The images on the right, (**Figure 5.12 B,D,F**) were taken from 60x water immersion objective which has NA=1.

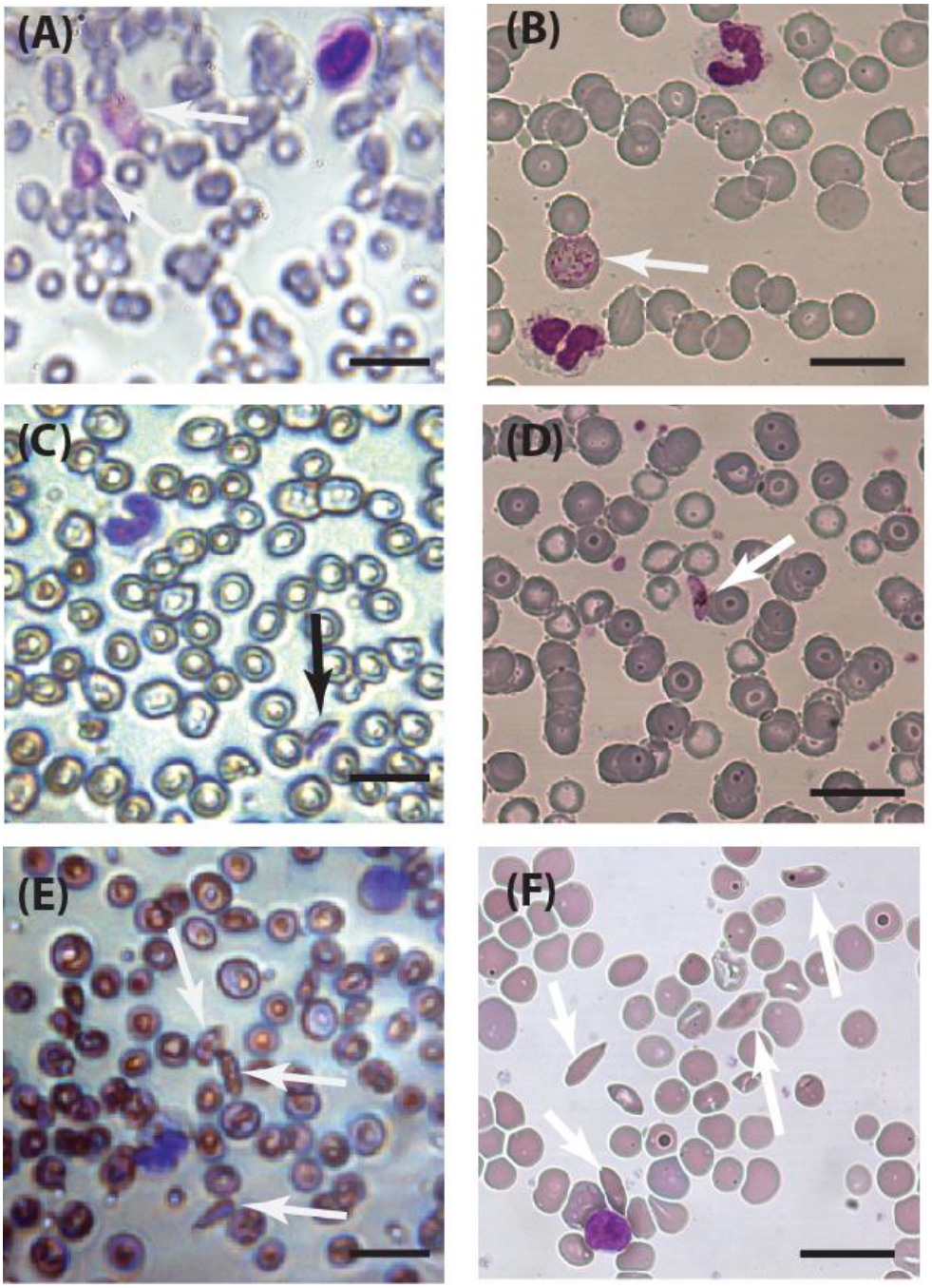

Figure 5.12: Image of thin film Giemsa stained micrograph shows both a mature and immature Plasmodiun vivax schizont (Malaria;PV) during growing trophozoite(A) Sickle cell disease anemia(C) Plasmodium falciparum during gametocyte (Malaria;PF)(E) imaging by μOIL system. Images on the right (B,D,F) obtain from 60x water immersion objective; NA=1 :scale bar 20 μm

5.6.6 Scanning image sample under one lens

With a single lens and higher magnification (**Figure 5.13A)**, μOIL system can be used to scan a larger area of interest for diagnostic purposes. An area of 520 μm x 160μm was scanned to demonstrate that sickle cells can be detected easily using μOIL imaging device (image processing software (Photoshop)) can stitch several images together as demonstrated in **Figure 5.13B**

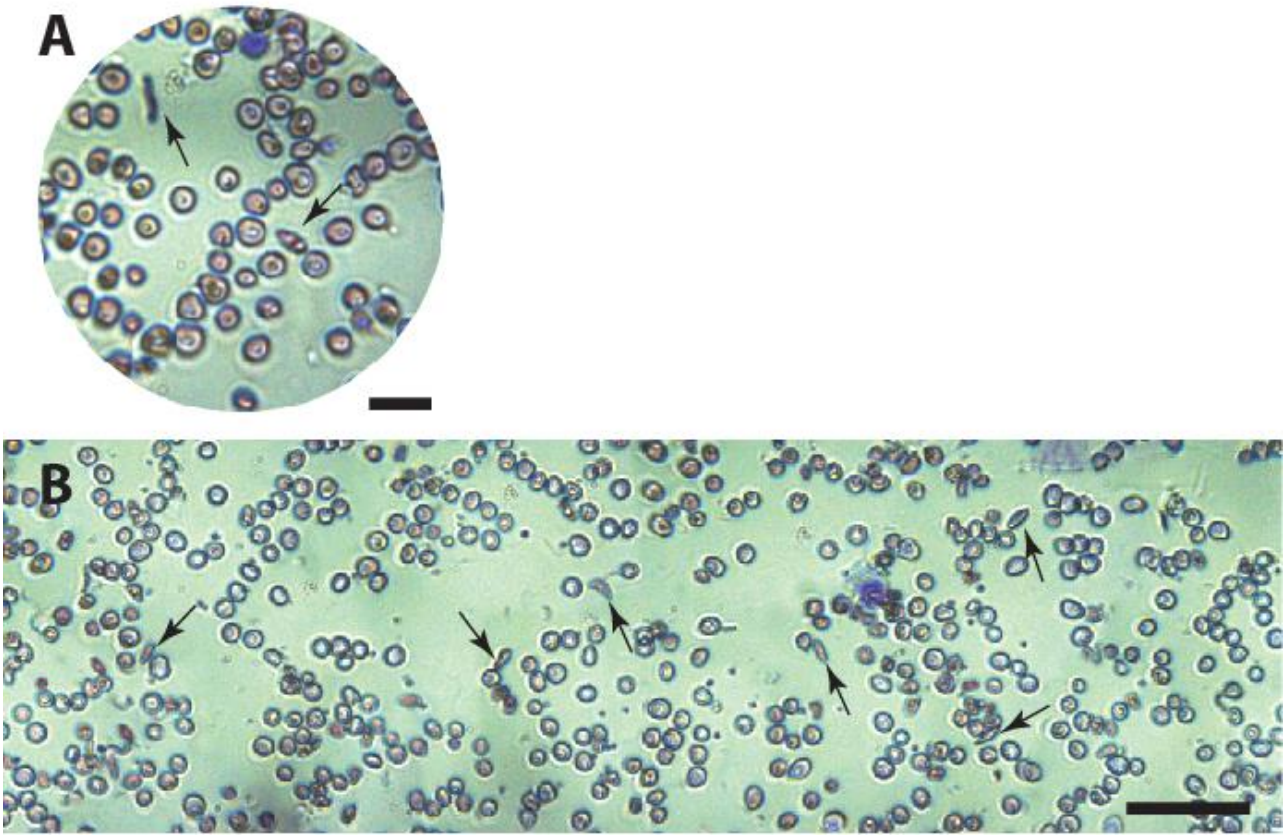

Figure 5.13: Image of sickle cell anemia red blood cells from blood smear specimens captured by one lens of μOIL system (A) and scan image (area 520 μm x 160μm) (B) Scale bar: 20 μm (A), 50 μm (B)

5.6.7 Fluorescence Imaging

μOIL system set up in trans-illumination geometry is can be used in fluorescence detection and imaging. An image of 4 μm Yellow/Green Fluorescent beads (excitation/emission 505/515nm) shows is seen field of view of 250 μm diameter (**Figure 5.14A**). We also stained THP-1 cells with Calcein AM to demonstrate fluorescence imaging of cells. Calcein AM is a cell permeant dye that is used to determine cell viability in most eukaryotic cells. In live cell, the green-fluorescent calcein is shown because acetoxymethyl ester hydrolysis by intracellular esterases [150]. The live THP-1 cells stand out against a dark background and can easily be counted (**Figure 4.14B**).

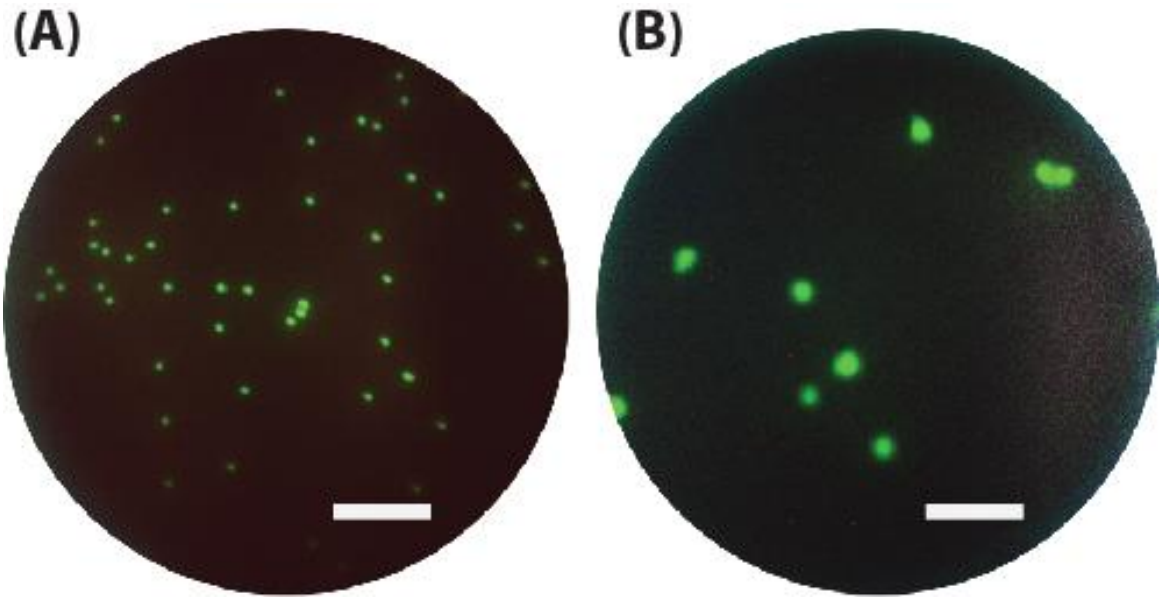

Figure 5.14: (A) Images of 4 μm Yellow/Green Fluorescent beads (excitation/emission 505/515nm) and (B) THP-1 cell dyed with Calcein AM from μOIL system Scale bar: 40 μm

5.6.8 Optical Imaging techniques for point of care and discussion

We discussed general detection methods in previous chapter (literature review). Here, we list the different methods comparing advantages and limitations (Table 5.1). One common method for chip scale optical imaging (holographic, shadow imaging, optofluidics microscope (OFM), μOIL) is the utilization of a CMOS sensor to record the image. Thanks to recent advances in CMOS image sensors and LEDs light sources, cost and size of optical imaging systems have been going down.

With a novel and simple to make μOIL chip, we can designed miniaturized optical pathway and housing while keeping the microscope to 40 g mass. Former approached to μOIL imaging in miniaturized format have generally required accessory, table-top optical instrumentation. Lens-less methods do not produce direct images but involve decoding diffraction patterns produced by cells immobilized at a fixed working distance[95][94]. OFM required assumptions about the microfluidic flow to deliver specimens at certain speeds at zero optical working distance across the CMOS sensor to generate high resolution projection images[81].

Our μOIL imaging device is assembled from mass-producible components where the cost per unit could be reduced with production volume. The LED, image sensor, filter and μOIL chip are all made via batch fabrication. The microscope housings were designed and made of plastic by 3D printing but once finalized they could be injection molded enabling much cheaper production of larger volumes. Thus the cost per unit can be expected to decrease rapidly with volume manufacturing. It is worth mentioning that the LED illumination is also highly energy efficient and the battery can last for a long time. The handheld microscope also offers ease of transport without the need for realignment.

The μOIL imaging microscope is different from prior miniaturized devices: it does not need alignment, simple to set up, small and portable (<40g). All parts can be mass produced and can address distinct applications in health care and research (**Table 4.1**).

5.7 Conclusions

In this chapter, we demonstrated that our compact μOIL optics based microscope can image individual cells at the submicron level and can also be used to count a variety of cells ranging in concentration from ~500/μL to 5 million/μL in a large FOV measuring 0.64 mm^2. This range covers both the red blood cells from dilute whole blood and white blood cells. Since the concentration of red blood cells is high, accurate counts can be obtained from a single lens, for white blood cells using all 16 lenses and automated counting is the more convenient way to obtain reliable counting statistics because of the much larger area imaged. High resolution imaging with the μOIL system for diagnostic purposes was demonstrated by imaging sickle blood cells and *P. vivex* ad *P. falciparium* infected red blood cells in bright field imaging mode. Flexibility of μOIL imaging system was also demonstrated for fluorescence imaging of 4μm spheres and peripheral mononuclear cells by the addition of only an emission filter and using blue LED trans illumination.

The capabilities of the μOIL imaging system are not limited to the examples given in this chapter. Thanks to the combination of high resolution and simplicity it can be used to image anything a high end compound microscope can image such as bacteria, microorganisms and tissue samples etc. The image quality and sensitivity of the system can be improved further with an advanced CMOS sensor, further modification of the μOIL imaging chip to prevent cross talk between the images at high magnifications.

Overall our integrated digital imaging system has shown resolution and flexibility beyond any of the small optical devices demonstrated with cell phone, shadow or holographic imaging systems.

5.8 Acknowledgment

I want to thank Prof. James Riddell, Director of HIV Clinical Research and Director of Infectious Diseases at The University of Michigan hospital for giving me an opportunity to be an intern at the outpatient HIV clinic to understand how such a POC device can be used in clinical setting. I also want to thank him for helping me to gain access to Hematology and clinical Microbiology laboratories to learn lab techniques (Blood count, Blood inspection, PCR test, C-Reactive Protein test, Cytomegalovirus (CMV) infection test, etc). I would like to thank Amrita Ray Chaudhury for her help with Matlab cell counting program. I would like to thank Microfluidics in Biomedical Sciences Training Program (T32 EB005582-05) for my fellowship and research support from the National Institutes of Health (NIH) and the NIH Director's New Innovator Award (DP2OD006458).

Table 5.1: Comparison currently optical imaging technologies for point of care diagnostics

Methods	Measurements/Applications	Advantages	Disadvantages	Resolution
Microscope on mobile phone (2009) [100]		Connect to Mobile phone for cell imaging. Optical components are taken directly from a microscope	Expensive, Bulky	1.2 µm (Objective NA 0.85)
Optical lens on mobile phone (2011) [104]		Optical components are taken off the shelf Connected to Mobile phone to perform cell counting, Wide field of views (81mm2), low cost	Low resolution	20 µm but using algorithms to increase resolution to 10µm
Optofluidic Microscope (OFM) (2008) [106][107] [81]	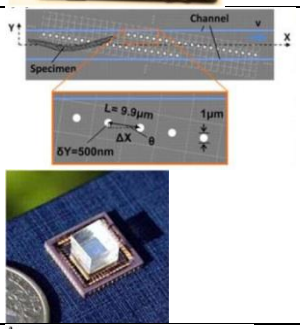	Chip scale, low cost, high resolution, for cell imaging	Sample needs to be in liquid and flow through each aperture, small FOV	1µm resolution
Shadow imaging (2009) [86]	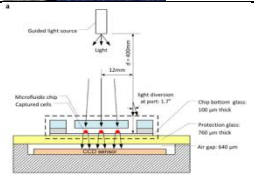	Chip scale, low cost, large FOV, for cells counting	Sample needs to contact or very close to CMOS chip. Require algorithms to decode diffraction patterns	Low resolution (N/A of NA)
Holographic microscopy (2009) [96][95][99]	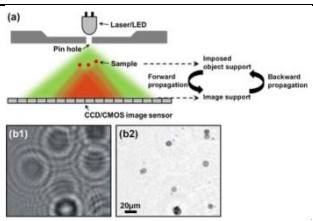	Chip scale, low cost, large FOV, for cells counting, high resolution	Require algorithms to decode diffraction patterns, require adjustment of light source through pinhole	1-2µm
µOIL imaging system [147] This work	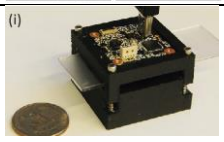	Chip scale, can integrate with microfluidic device, low cost, high resolution, for counting, and imaging purpose	Image aberration	~0.5 µm

CHAPTER 6

An Implantable, X-Ray Based Blood Pressure Microsensor for Coronary In- Stent Restenosis Surveillance and Prevention

The overall driving force for this thesis has been to make simple, cost effective biomedical devices which can be used for disease diagnostics and treatment monitoring. Since coronary artery disease is a leading cause of morbidity and mortality we decided to see if we can make a simple sensor to monitor restenosis in coronary artery stents.

In this chapter, we describe an X-ray addressable Blood Pressure (X-BP) microsensor. The X-BP has a column of radio-opaque liquid that changes its length with blood pressure. The X-BP allows for the non-invasive evaluation of the pressure drop across a stent and the fractional flow reserve (FFR) on radiographs. A FFR threshold of 0.75 to 0.8 is clinically well established as the cut-off for the identification of hemodynamically significant stenosis that requires intervention. The X-BP membrane was modeled and the x-ray Signal-to-Noise ratio (SNR) of different sensor dimensions was experimentally determined. Based on this data optimal design parameters were selected. The sensor was prototyped and tested under microscope, with radiographs and video fluoroscopy. The sensor has a potential dynamic range of 0-200 mmHg, and can reliably resolve the clinically important pressure drop of 20-25% across the dynamic range for an FFR value of 0.8 to 0.75 or less. The X-BP also has a time constant less than 32 ms, with no appreciable hysteresis. We believe this sensor can be used for periodic screening of coronary in-stent restenosis.

6.1 Innovation

We developed a novel X-ray readable passive blood pressure sensor, small enough to fit into coronary stents. Our sensor does not need any power and is simple to fabricate. It measures pressure changes by changes in the length of an X-ray contrast agent column with pressure in a microchannel. While there are many pressure sensors for larger organs and arteries, making one small enough to fit into a coronary artery stent has been the holy grail of pressure sensors, which has not yet been achieved. In what follows we describe our proof of concept device.

6.2 Introduction

Coronary Artery Disease (CAD) is the leading cause of morbidity and mortality in people over 20 years old in the United States. It affects 15.8 million people and accounts for 1 in every 6 deaths [38]. The direct and indirect cost of CAD was estimated at $431.8 billion in 2007 [2][3]. The genetic, epigenetic and lifestyle risk factors of CAD converge to damage the endothelial lining of the vessel wall. The resulting inflammatory response at the cell wall leads to plaque formation, with or without calcium deposition, and coronary artery stenosis. A stenosis causes a pressure drop (measured in mmHg) that decreases myocardial perfusion [151][153][154]. This can lead to a myocardial infarction, frequently referred to as a heart attack.

A common treatment of coronary artery stenosis is Percutaneous Coronary Intervention (PCI), the placement of a stent to increase the patency of the artery. In 2004 there was an estimated 1.3 million coronary catheterizations and 658,000 percutaneous interventions performed. Coronary in-stent restenosis is a common mode of stent failure. It accounts for more than half of nonfatal myocardial infarctions (MIs) after PCI [155].

The first stents were Bare Metal Stents (BMS). BMS had 5 year restenosis rates of 30%[156][40]. Finer stent struts less than 100 μm led to 1.68 times lower restenosis rates[157]. Newer Drug Eluting Stents (DES) have early restenosis rates lower than BMS, but meta-analyses have reported a fivefold greater risk of late stent thrombosis[158] and five year follow-up data revealed little difference in death or stent thrombosis[40][159]. As a result, PCI therapies with drug eluting stents have decreased in the past years.

The gold standard to assess native coronary artery stenosis and in-stent restenosis is angiography. In angiography a contrast agent is injected directly into the coronary artery. Angiography accurately identifies the two extreme cases of a stenosis: high degree stenosis and patent vessels. However, a large number of stenoses are intermediate grade, and their effect on myocardial perfusion cannot be assessed visually.

To address this shortcoming, cardiologists developed the Fractional Flow Reserve (FFR). The FFR is the ratio of the perfusion pressure after (Pa) and before (Pb) a stenosis measured during coronary angiography (FFR = Pa/Pb). A thin wire with a pressure transducer is passed through the stenosis to measure the pressure before and after the stenosis. FFR-guided procedures with a threshold of FFR ≤ 0.75, pressure drop of 25% or more, have reduced the rate of death, nonfatal myocardial infarction, and repeat revascularization [58]. FFR- guided stenting and optimal medical therapy was superior to best medical therapy alone and decreased the need for urgent repeat revascularization[40]. However, angiography is an invasive procedure with associated risk and costs approximately $13,014 per procedure[59].

Medical imaging, a non-invasive, less expensive alternative to angiography, has not been able to measure the FFR[160], or determine coronary in- stent restenosis. Coronary CT Angiography does not have the required resolution to reliably identify intermediate- grade native coronary artery stenosis, let alone in-stent restenosis that is confounded by beam hardening artifact from the metal stent. Nuclear stress tests can evaluate myocardial perfusion, but that is an indirect measure of stent patency. The cost of imaging ($700- $5,000) and the radiation exposure are prohibitive for these exams to be used as screening tests for a population. Clinically, a patient has to be symptomatic for a physician to prescribe an imaging test. Many of the patients with CAD are diabetic, or have already suffered a first myocardial infarction, both of which result in denervation. These patients may not be able to sense the pain of a heart attack to seek medical help. By the time a stress test is ordered it is often too late, the stent is completely occluded, the myocardium is nonviable, and re-intervention is no longer indicated [161].

Although several sensors have been developed to measure blood pressure in the ventricles [162][163][164][27][165][166][30][36], including RF powered telemetry [29][43][167], low power systems [126][28][168][169][35] and optical telemetry[36][35][33], none have been successful in measuring coronary arterial blood pressure. The main limitation is size. The ventricles have a lumen of 4-6 cm, whereas coronary arteries have a diameter between 4 and 2mm. The two smallest pressure sensors currently commercially available are the CardioMEMS EndoSensor^{TM}, 5x30 mm [43][44] and the ISSYS[45] sensor (20mm^3). These sensors monitor congestive heart failure (CHF) and Aortic Aneurysm graft pressures respectively. Their typical footprint is ~1 x 0.5 cm, while cardiac stents have an average diameter of 4 mm, making integration of such large devices impossible in a way that does not obstruct

flow. Nanoparticles do not produce sufficient signal to cross the mediastinum, which can be a few centimeters in depth [36]**.** There exist no sensors or other means to accurately and noninvasively measure coronary pressure, or estimate in-stent restenosis[46].

To address these pressing medical needs we have developed a micromachined, passive, X-ray-detectable Blood Pressure sensor, the X-BP microsensor. The X-BP enables the noninvasive and inexpensive evaluation of the FFR across a stent[170]. Blood pressure is obtained by simply measuring the length of a radio-opaque liquid column that is housed inside the X-BP microsensor on a chest radiograph (**Figure 5.1A**). By integrating two X-BP microsensors into a stent, one on the proximal and one on the distal ends of the stent, a radiologist can deduce the FFR across the stent by measuring the two pressures (**Figure 5.1B**). We believe that the X-BP microsensor's unique advantages of small size, absence of a battery, antenna, or any electronic components, as well as easy integration with non-proprietary x-ray machines can become an ideal solution to the long-standing need for the non-invasive, inexpensive and periodic evaluation of coronary in-stent restenosis.

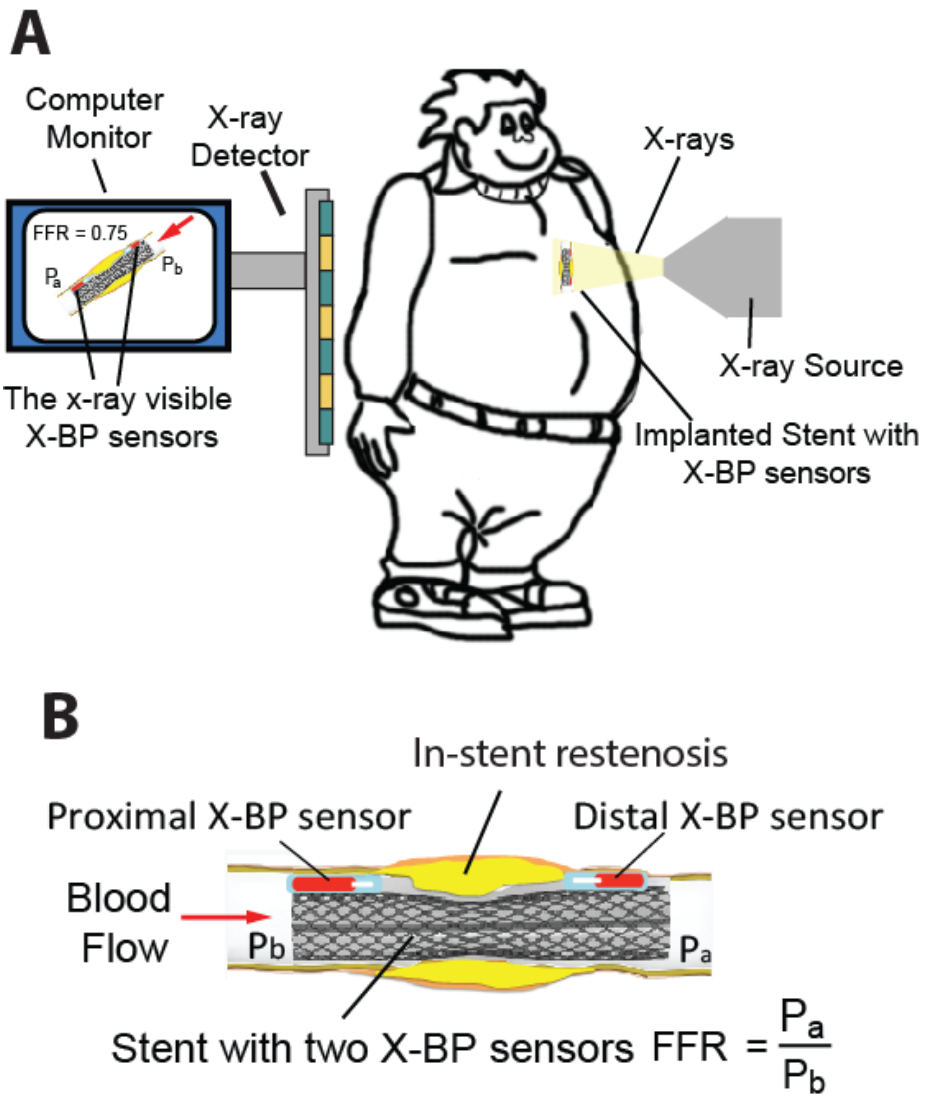

Figure 6.1: (A) X-ray based pressure sensing technology for monitoring coronary in- stent restenosis non-invasively. (B) Two X-BP microsensors integrated in a stent provide a direct measure of the Fractional Flow Reserve (FFR).

6.3 The X-BP Microsensor

6.3.1 Design and Working Principle.

The X-BP has three components: a blood pressure-exposed membrane, a micro-reservoir and a microfluidic gauge (**Figure 6.2 A**). The bulk of the device is made of silicon and glass

which do not significantly attenuate x-rays in comparison to anatomic background, as they have a similar mass attenuation coefficient to soft tissue, and are therefore imperceptible on clinical radiographs. The micro-reservoir is filled with radio-opaque, x-ray visible, fluid (Isovue-370). One of the micro-reservoir surfaces is the pressure-exposed membrane. As pressure increases, the membrane deflects, and displaces the radio-opaque fluid from the micro-reservoir into the microfluidic gauge (**Figure 6.2 B**). The micro-reservoir and micro-fluidic gauge together form a micro-hydraulic system [170][171] that amplifies small deflection of the membrane into a larger displacement of the radio-opaque fluid. These structures are used to improve sensitivity and dynamic range of sensors[38][39]. Here, the displacement amplification is needed to bring the movement of the fluid within the x-ray imaging resolution. Therefore, by optimal choice of reservoir to gauge geometry, SNR, thus sensitivity can be tailored to a desired value.

The x-ray visible length of radio-opaque liquid in the microfluidic gauge (indicated as 'L_{column}' in **Figure 6.2 BIII**) is proportional to the pressure applied to the membrane and acts as a pressure indicator. To measure the pressure drop across a stent and the FFR, two X-BP sensors are required: one sensor is placed in the proximal end and another sensor in the distal end of a stent. The two lengths measured on a single radiograph provide the pressure drop and thus the FFR across the stent.

The micro-reservoir is 8.5 mm long and either 400 µm or 600 µm wide. The microfluidic gauge is 4 mm long and 250 µm wide. Both the micro-reservoir and the microfluidic gauge are 250 µm thick. The reservoir and gauge are connected through a narrow, tapered micro-channel (**Figure 6.2 D**) which is 100 µm wide and 150 µm deep. At atmospheric pressure the membrane is infinitesimally deflected and the radio-opaque liquid reaches the tapered micro-channel but does not extend into the gauge (**Figure 6.2 BI**).

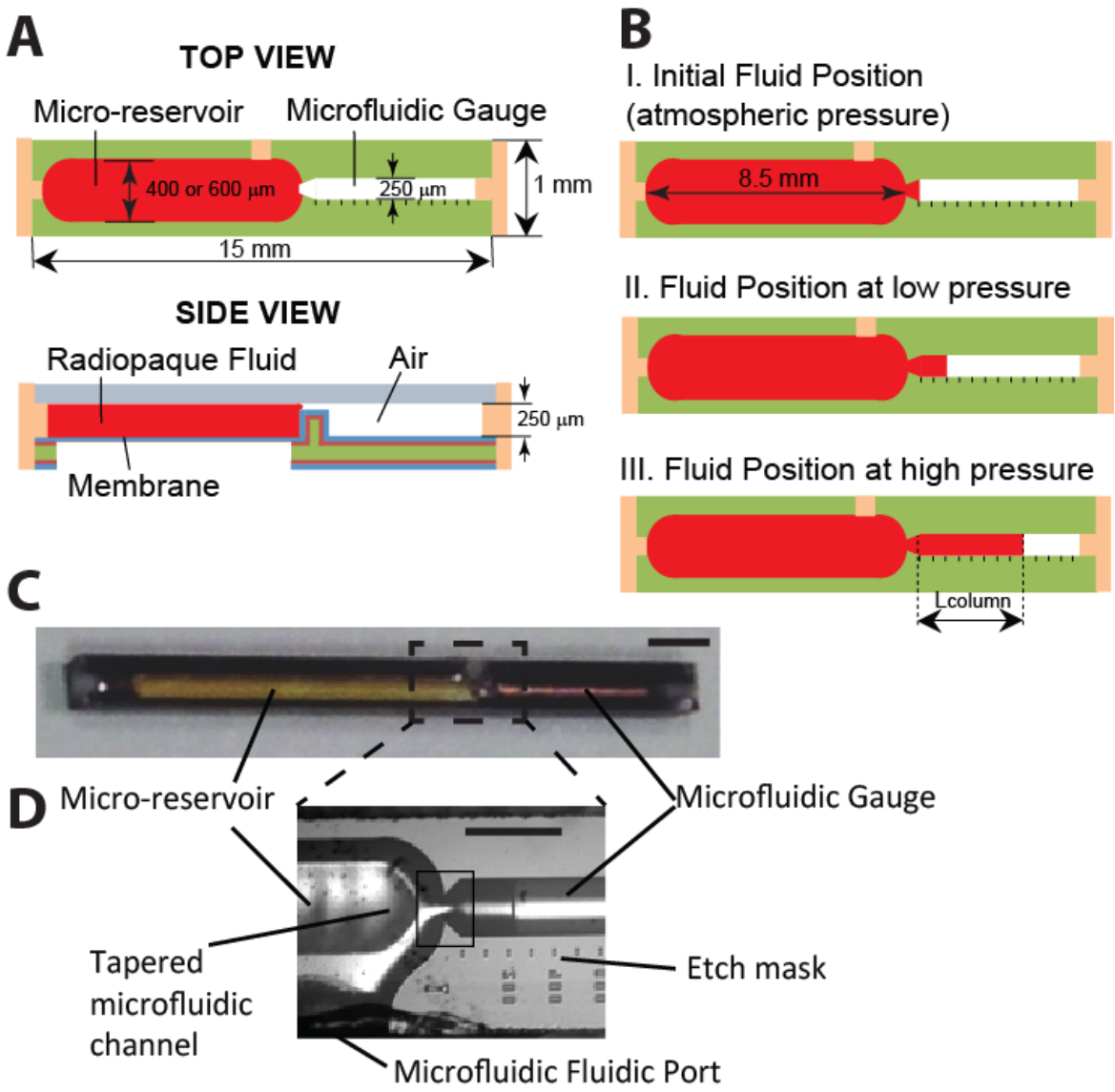

Figure 6.2: (A) Top view and cross section of the X-BP. (B) The working principle of the X-BP: the microfluidic gauge fills with the radio-opaque fluid as pressure is applied to the membrane. (C) The fabricated sealed sensor filled with Isovue-370. (D) The tapered micro-channel connection between the micro-reservoir and microfluidic gauge. C: Scale bar, 1 mm. D: Scale bar, 400µm.

6.3.2 Microfabrication and Sealing.

We used a three-mask bulk micromachining process to fabricate the X-BP microsensor (figure 3A). We first performed a 2-step deep reactive ion etching (DRIE) on the front side of a 400 μm thick silicon wafer. The 2-step DRIE process created the 400 μm wide micro-reservoir and the 250 μm wide microfluidic gauge. A 1 μm of thermal oxide was grown and stripped in Buffered oxide etch to reduce the roughness of the DRIE-etched silicon surface.

We deposited 0.2 μm of thermal oxide and 0.5 μm of low stress of low pressure chemical vapor deposition (LPCVD) silicon nitride (50 MPa tensile stress [174]). We then anodically bonded (700 V at 350°C) a 200 μm thick Pyrex wafer to the front, DRIE-etched side of the silicon wafer to enclose the micro-reservoir and the microfluidic gauge. We patterned the nitride/oxide films on the backside of the wafer with RIE. We diced the bonded wafer to create fluidic ports on its side and DRIE-etched to release the silicon nitride membrane.

We filled the device with Isovue 370 and sealed it in the following manner (**Figure 6.3B**): (i) we coated the inner surfaces of the X-BP sensor with a mild hydrophobic coating (Rain-X) using a custom-made 150μm glass pipette (**Figure 6.3B II**). The coating was allowed to form for 10 minutes and excess Rain-X rinsed off with isopropyl alcohol (IPA). Residual IPA was evaporated at 60°C for 5 minutes. We sealed the outlet of the microfluidic gauge with a biocompatible adhesive (Permabond ET5145 epoxy) (**Figure 6.3B IV**). We filled the micro-reservoir with Isovue-370 using the custom-made pipette. The microfluidic ports of the micro-reservoir were sealed with epoxy.

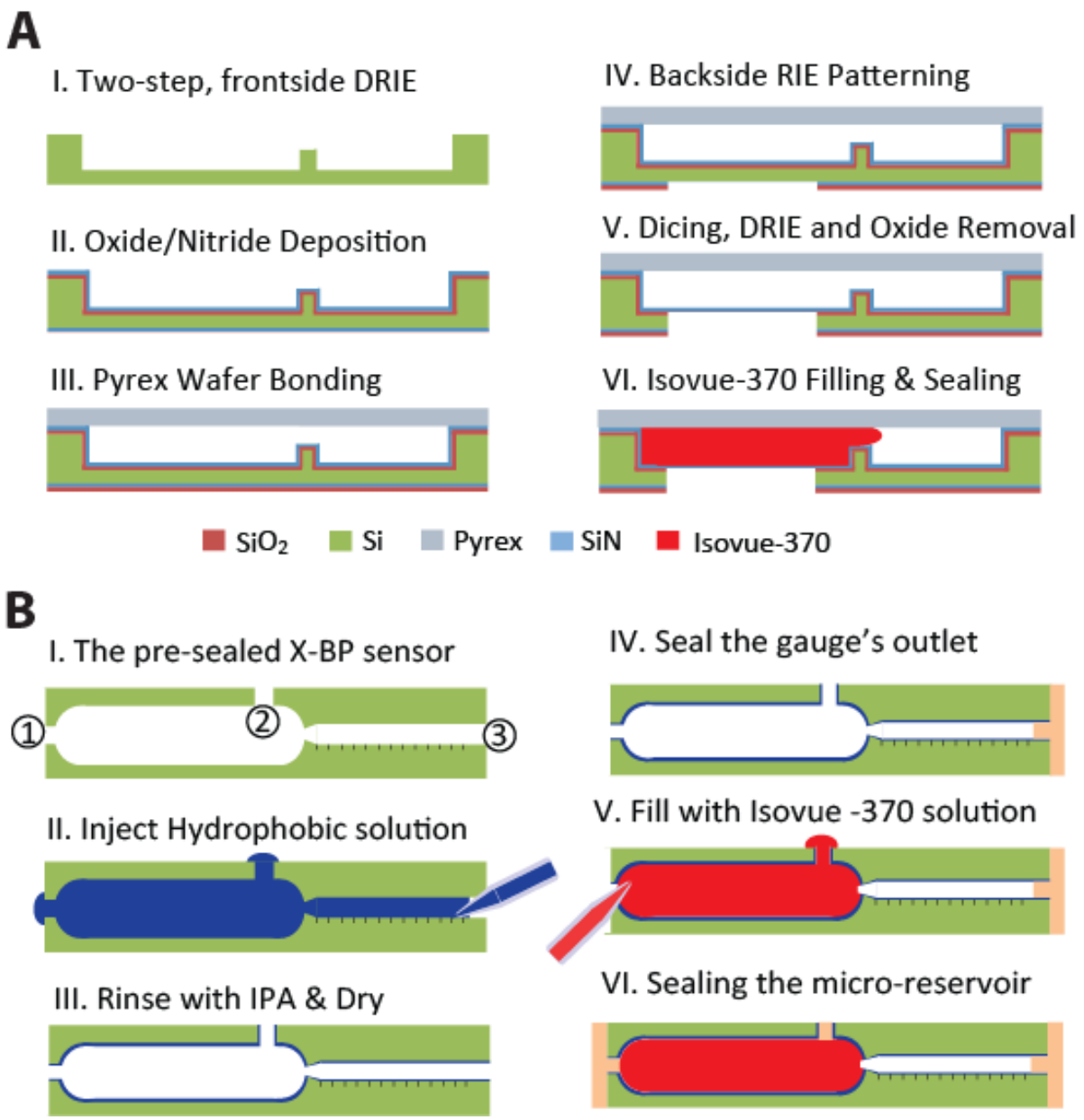

Figure 6.3: (A) The microfabricaton process of the X-BP sensor. (B) The process of filling the sensor with Isovue-370 and sealing the 3 fluidic ports (numbered 1-3 in B(I)).

6.4 Results and Discussion

6.4.1 X-Ray Attenuation and Signal of the microfluidic gauge

The signal produced by the Isovue-370 in the microfluidic gauge is related to the mass-attenuation (μ/ ρ) coefficient of the Isovue, a material property, and the thickness of Isovue the x-rays transverse (x) in a manner similar to the Beer-Lambert law:

$$I = I_0 e^{-(\mu/\rho)\,x} \qquad (6.1)$$

The deeper the microfluidic gauge, the greater the distance x, the x-ray attenuation I, and the signal of the sensor on the radiograph.

However, a deeper microfluidic gauge requires a larger volume of radio-opaque liquid to fill. Either the length of the gauge will be reduced which will decrease the sensor sensitivity and dynamic range, or the membrane will have to deflect further to displace more radio-opaque liquid to fill the entire gauge. A greater membrane deflection can be achieved with a wider, or a thinner membrane. The height of the microfluidic gauge and the membrane width and thickness have to be optimized to attain the best sensitivity, dynamic range and x-ray signal to noise ratio (SNR) while keeping the overall device size small enough for coronary artery implantation.

6.4.2 Microfluidic Gauge Dimensions and Signal to Noise Ratio (SNR)

To experimentally determine the SNR with respect to the Isovue-370 thickness, we fabricated test structures with a wide range of heights (100-450 μm) on a 400 μm thick silicon wafer covered by thermal silicon dioxide (0.2 μm) and LPCVD low stress silicon nitride (0.5 μm), sealed with a 200μm thick pyrex glass wafer and filled them with Isovue-370. The test structures were imaged with a commercial x-ray imaging system (Siemens Axiom Luminos TF). The SNR of the radio-opaque column was calculated as follows [175]:

$$SNR = \frac{\Delta I}{\sigma_I} \qquad (6.2)$$

Where σ_I is the standard deviation of the background intensity and ΔI is the observed change in the intensity of the radio-opaque column when compared to the background intensity. The background intensity is measured at an area adjacent to the microfluidic gauge, consisting of the entire 600 μm thick silicon/glass wafer.

Based on the experimental results obtained, Isovue-370 revealed a high SNR of 4.5 and 21.5 at 100 and 450μm microfluidic gauge thickness respectively (**Figure 5.4**) while σ_I was 1.3. The thicker the gauge, the higher SNR and the lower sensitivity, since the volume of fluid that is required to fill up the gauge is proportional to the thickness of the gauge. As a result of this test, we designed the X-BP device with a 250 μm thick x 250 μm wide microfluidic gauge that gave us an SNR of 12.75.

To confirm adequate visibility over anatomic background we filled 250 μm and 340 μm inner diameter polyimide capillaries with Isovue 370 and superimposed them on the chest phantom: an artificial model of human chest including lungs, heart as well as bones and arteries commonly used for radiology producing life- like images under radiographs that are indistinguishable from human images by a trained radiologist. The capillaries have significantly longer length than the prior test-structures, which allow investigation of the SNR over a larger, more variable anatomical background, on a single radiograph. The resulting SNR was 1.5 and 1.74 respectively with the capillaries superimposed on the heart and ribs providing adequate visualization. A SNR of 1.5 was deemed acceptable for detection of the changes in the length of the microfluidic gauge by the radiologists looking at the X-ray images taken with the phantom. As a result, the microfluidic gauge thickness was set to 250 μm.

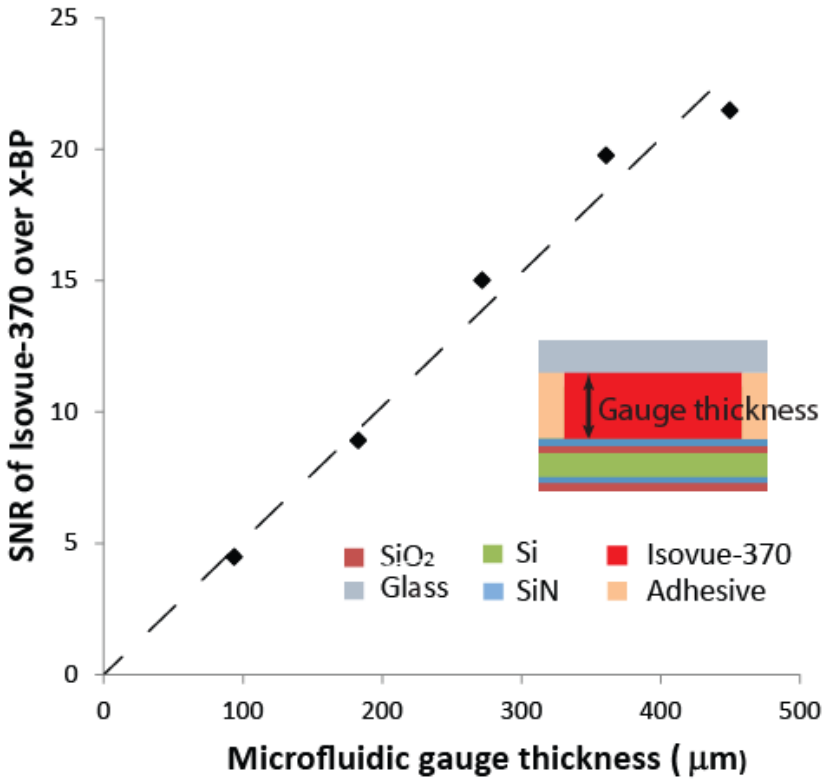

Figure 6.4: SNR of Isovue 370 for different microfluidic gauge thicknesses as measured in radiographs with no background (e.g. no use of phantom). The schematic (insert) represents the cross section of the test structure

---

6.4.3 Analytical Model of the X-BP pressure sensor.

The relationship between blood pressure (P_{blood}) and the length of the radio-opaque liquid column (L_{column}) inside the microfluidic gauge is the key aspect of the X-BP sensor design as this relationship defines most of the clinically relevant specifications (dynamic range, resolution, sensitivity) of the sensor. To obtain that relationship, we modelled the forces and pressures acting on the radio-opaque liquid when an external pressure (P_{blood}) is applied to the membrane (figure 5). The silicon nitride membrane of the X-BP sensor was modeled as a thin, elastic, rectangular plate which is anchored in its periphery. The membrane experiences a net, uniform pressure load, which depends on the balance between the blood pressure and the

pressure exerted from the radio-opaque fluid (P_{liquid}). The maximum deflection (W) of the membrane can be calculated from [176]:

$$P_{blood} - P_{liquid} = \frac{C1\,\sigma tW}{a^2} + \frac{C2EtW^3}{a^4} \qquad (6.3)$$

where C_1, C_2 are constants (C_1 = 1.52 and C_2 = 0.7 [176]), E is the Young's modulus of silicon nitride (E=250 GPa [177][178][179]), σ is the residual stress of the silicon nitride film, α is the half width of the membrane (α=300 μm for 600 μm diaphragm), t the membrane thickness (t= 0.5 μm).

We varied the initial stress present in the membrane in our analytical modeling because we have no way of knowing the exact initial stress present in the membrane. Initial stress of the membrane can change the deflection of the membrane significantly. We used a low stress silicon nitride deposition process. However, it is well known that even low stress nitride films can have stresses between 50 MPa compressive to 50 MPa tensile even on the same wafer [174].

Assuming that the membrane deflection profile has a cylindrical cross section when the membrane is pressurized, the volume of the radio-opaque liquid that is being displaced (V_{liquid}) is given by:

$$V_{liquid} = tan^{-1}\left(\frac{a}{R-W}\right) * (R^2 b) - \frac{a*b}{2}(R-W)\,, \quad \text{where} \quad R = \frac{a^2+W^2}{2W} \qquad (6.4)$$

where R is the radius of curvature of the deflected membrane. W is the maximum deflection of the diaphragm. The above equation neglects the non-cylindrical deformation at the two ends of the membrane. V_{liquid} values obtained from COMSOL simulations show less than 10% deviation from the results obtained from equation (4). V_{liquid} also represents the amount of fluid that enters the microfluidic gauge as the liquid is incompressible. Given the (fixed) cross section of the microfluidic gauge (A_{gauge} = 250 μm x 250 μm), we can write:

$$L_{column} = \frac{V_{liquid}}{A_{gauge}} \quad (6.5)$$

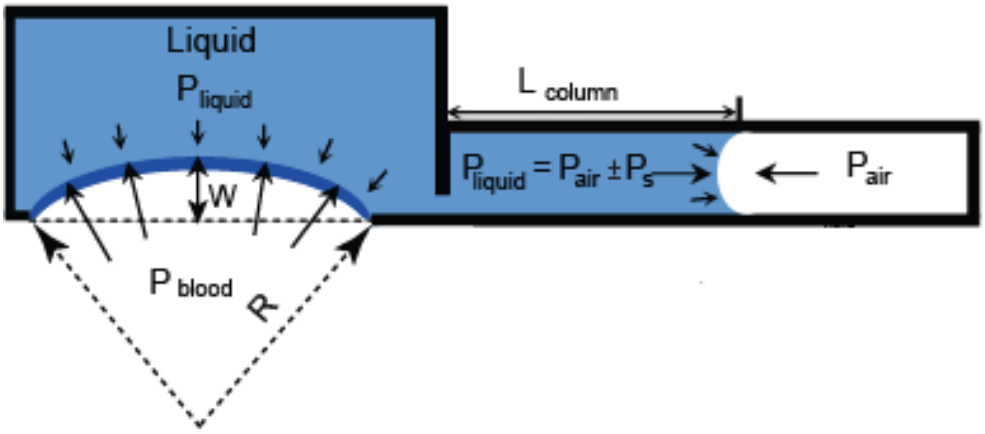

Figure 6.5: Schematic of the X-BP pressure sensor analytical model

---

Inside the microfluidic gauge, P_{liquid} is a function of the air pressure and the surface tension force generated at the fluid/air/solid interface. For all practical purposes, the surface tension force (P_s) has a minor affect on P_{liquid} (<10%) even at extreme hydrophobic conditions, eg. when the contact angle is ~120^0 (hydrophobic), P_{liquid} increases by only ~3 mmHg. In addition, we noticed that our post-fabrication surface treatment (the sensor was coated with a hydrophobic agent -Rain X) resulted in nearly ninety degree contact angle, which allows us to neglect the effect of surface tension force in our analytical modelling.

Neglecting the surface tension force P_{liquid} equals the pressure of the air inside the gauge (P_{air}). Assuming that the air inside the microfluidic gauge behaves as an ideal gas under constant temperature and occupies initially the entire length of the gauge (L_0) at initial pressure (P_0), we

can derive an expression between L_{column} and P_{liquid}:

$$P_{liquid} = \frac{P_0 L_0}{L_0 - L_{column}} \quad (6.6)$$

Combining (6.3) through (6.6), we can estimate L_{liquid} and the corresponding P_{blood} for a given W from:

$$L_{column} = \frac{1}{A_{gauge}} tan^{-1}\left(\frac{a}{R-W}\right) * (R^2 b) - \frac{a*b}{2}(R - W) \quad (6.7)$$

$$P_{blood} = \frac{C1\,\sigma tW}{a^2} + \frac{C2EtW^3}{a^4} + \frac{P_0 L_0}{L_0 - L_{column}} \quad (6.8)$$

Assuming P_0 is at atmospheric pressure, and L_0 is the total gauge length that contains air inside without any applied pressure.

6.4.4 Length of the radio-opaque column (L_{column}) versus applied pressure (P_{blood})

We placed the X-BP sensors in a custom-made, air-filled pressure chamber to experimentally quantify the dependence of L_{column} to P_{bood}. We varied the pressure with an electronic pressure controller (Elveflow AF1) and recorded the displacement of the fluid/air interface in the microfluidic gauge with a microscope (Olympus BX51W1, Epi-illumination mode, 5x objective). The known distance of the etch marks along the length of the microfluidic gauge (**Figure 6.2D**) was used as a scale bar to accurately measure the length of the fluid column (L_{column}).

We tested two designs of the X-BP sensor, with 400µm and 600µm wide membranes, 0.5µm thick and 8.5 mm long. The experimental results (**Figure 6.6A**) indicate that the X-BP sensors accurately respond to the clinically relevant pressure range (0-150 mmHg), as predicted by the analytical model. The X-BP sensors show a logarithmic Pressure- Displacement response that is expected to saturate at pressures higher that 200 mmHg. This logarithmic response results in high sensitivity (measured in microns of L_{column} increase per 1 mmHg of applied pressure) at

low pressures and decreased sensitivity at higher pressures (**Figure 6.6B**). The results from the analytical model accurately predict the observed behavior at low pressures (<100 mmHg) while at high pressures (>100 mmHg) there is ~20% deviation from the experimental data.

We attribute this deviation to three factors: (1) values of the residual stress and elastic modulus of the nitride films were based on literature [177], (2) the presence of a residual compressive oxide on top of the tensile nitrile film that alters the membrane properties. (3) The membrane is deposited as a conformal layer at the bottom of the etched micro-reservoir (**Figure 6.3A II**) [180] which may result in a membrane with a small positive curvature when it is released (Figure 3AV).

6.4.5 Hysteresis.

To evaluate the hysteresis of the membranes, we exposed them to sinusoidal pressures between 0 and 150mmHg at 1 Hz and recorded displacement under the microscope. Throughout the three cycles, the average peak value for 400 μm and 600 μm width diaphragms are 220 μm and 378 μm respectively. The changes seen in peak values during cycling are within experimental measurement error of ± 9 microns. The parts of the curve with a positive slope and those with a negative slope are mirror images of one another for both 400μm and 600 μm wide membranes, indicating minimal, if any hysteresis (**Figure 6.6C**).

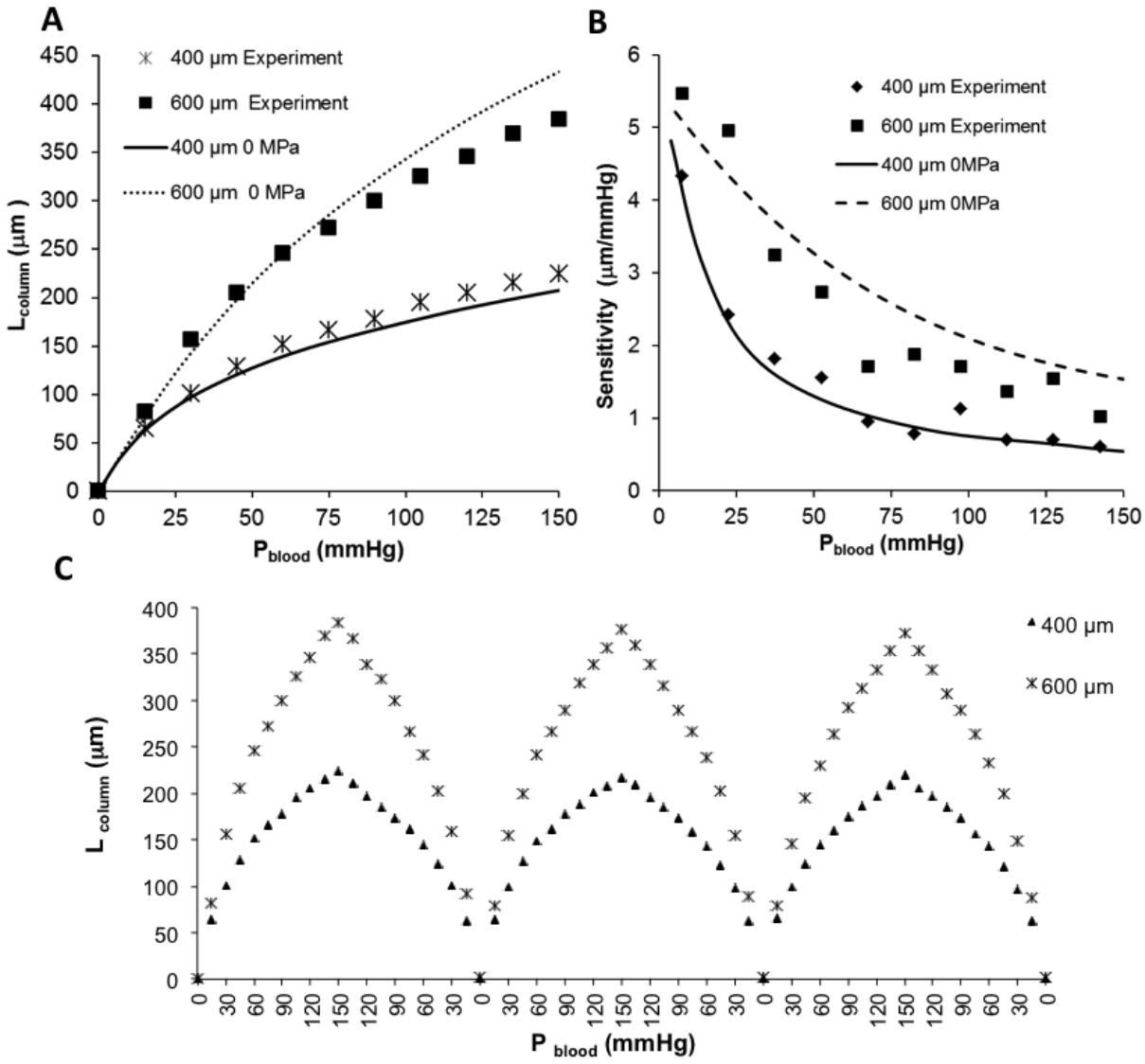

Figure 6.6: (A) Plot of Blood Pressure vs displacement of radio--opaque fluid (Isovue 370) in the microfluidic gauge chamber 250µm wide x 250 µm deep. (B) Sensitivity of X-BP as a function of applied pressure. Diaphragm sizes are 400 µm and 600 µm wide. (C) Three cycles of pressure-displacement shows symmetric increase and decrease in displacement, indicating minimal hysteresis.

6.4.6 Maximum Stress on the Membrane

A mechanical failure of the X-BP sensor can render the sensor useless and pose a risk to the patient. As the membrane is the most fragile element of the sensor, we evaluated the possibility of failure with COMSOL software. We calculated the stress distribution across the membrane. It is critical that the maximum stress of the membrane, the von Mises stress, to be smaller than the (tensile) yield strength of silicon nitride (~5.5 GPa [177][181][182]) as increased stress can lead to plastic deformation and/ or microcracks. In our simulations we spanned a pressure range between 0 and 300 mmHg for 400 μm and 600 μm wide membranes (**Figure 6.7A**) with zero residual stress. The results suggest that even at extreme blood pressure values (e.g. above 200 mmHg), the maximum von Mises stress is one order of magnitude lower than the silicon nitride yield strength. As expected, the maximum stress always appears at the edges which are anchored (**Figure 6.7B**).

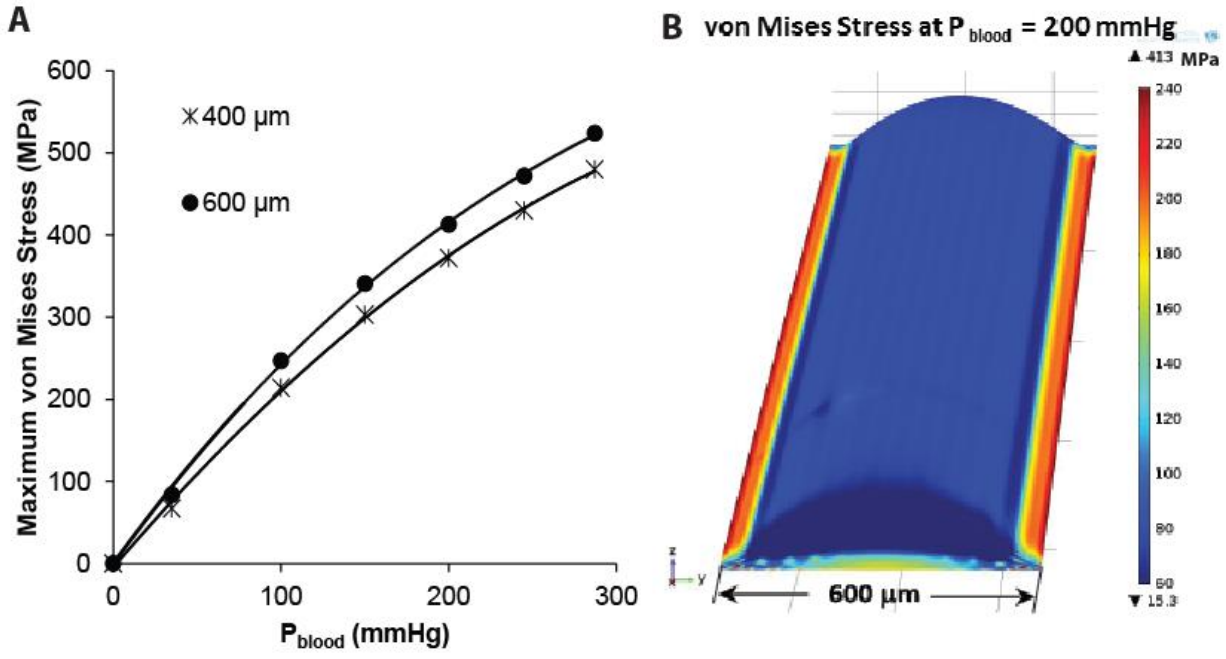

Figure 6.7: (A) The maximum stress at different applied pressure on 400μm and 600 μm wide diaphragm. (B) 3D stress distribution across 600 μm membrane (maximum stress of 413 MPa)

To mass produce an implantable sensor we need to ensure long term reliability and biocompatibility. For long term reliability we plan to fatigue test the sensor over millions of cycles at physiologic parameters. Silicon and glass that are used in the X-BP are biocompatible [183]. However, there is currently no general consensus method to declare a sensor biocompatible besides testing the finished product [184].

6.4.7 Sensor time constant (τ)

To determine the time constant (τ) of the X-BP we acquired real-time video of the X-BP in the pressure chamber at 20 frames per second under microscope to capture images of liquid movement at the device gauge (F**igure 6.8**). We varied the pressure between 75 and 150 mmHg to simulate physiologic, mildly hypertensive blood pressure commonly seen in patients with CAD.

The video images were post-processed in Metamorph (Molecular Devices, USA). Using time constant equation:

$$\boldsymbol{V(t)} = \boldsymbol{V_o}(\mathbf{1} - \mathbf{e}^{-\frac{t}{\tau}}) \qquad (6.8)$$

We found that the X-BP has a τ of 32ms which is 30-60 times smaller than the cardiac cycle of 1-2 Hz. Therefore, the X-BP could be used for real- time measurements of the FFR under fluoroscopy.

The fast time constant implies a variation in the X-BP gauge length and the sensor sensitivity depending on where in the cardiac cycle a radiograph "snap-shot" is acquired. This is less of a problem because the FFR is the ratio of the two X-BP sensors and both are affected equally. We do not expect this to be critical, but two additional solutions would be to acquire a number of radiographs and choose the one with the greatest X-BP displacement, or gate the

study to the cardiac cycle with a pulse oxymeter.

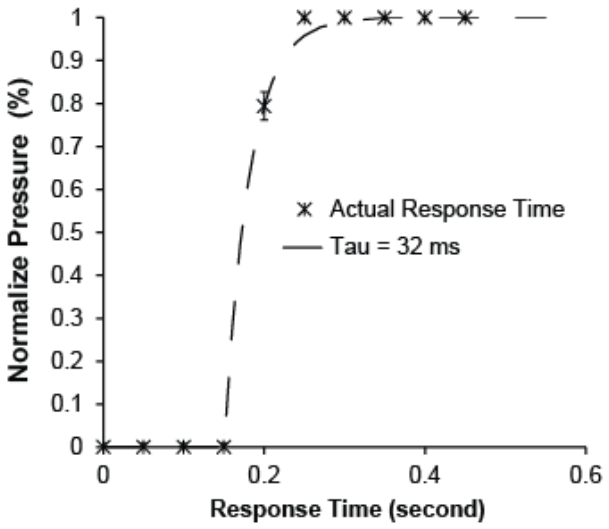

Figure 6.8: Time response for pressure changing from 75 mmHg to 150 mmHg. Average Time response is 32ms.

6.4.8 X-ray spot images over anatomic background SNR and Sensor Pressure Resolution

To simulate as real an imaging scenario as possible we acquired spot images, ie "stills", of the X-BP sensor over the anatomic background of the standard radiology chest phantom (**Figure 6.9**). The chest phantom comprises of human osseous structures embedded in Lucite, which has a mass attenuation coefficient similar to soft tissue, resulting in radiographs indistinguishable from human anatomy.

Two X-BP sensors (**Figure 6.9A**) were placed inside a stent (Boston Scientific Express LD iliac/ biliary 8mm diameter, 27 mm long, stainless steel). The stent was narrowed in its center to demonstrate a stenosis. The X-BP sensor (X-BP-A) in the upper part of the stent (**Figure 6.9 B-I, C-I**) had its gauge completely filled with Isovue, to simulate normal perfusion

pressure, while the sensor in the lower part (X-BP-B) of the image had Isovue only in the reservoir (**Figure 6.9 B-III,C-III**), to simulate the pressure drop of a stenosis. Radiographs of the stent and the two X-BP sensors were acquired with and without magnification (Siemens Axiom Luminos TF).

Qualitatively, the microfluidic gauge was easily visible inside the micro-reservoir (**Figure 6.9B**). SNR was calculated for the microfluidic gauge for a best- case (F**igure 6.9B-I**) and a worst case scenario (**Figure 6.9B-II and 6.9B-III**). In the best case scenario the gauge overlaps the thorax, heart and ribs. In the worst case scenario the X-BP overlaps the thorax, heart, ribs and stent. The x-ray images from eFilmLite 3.4 (Merge Healthcare, USA) were exported in tiff format to Metamorph and the SNR of the images were found to be 4.69 for the best case and 2.79 for the worst case, which confirms the qualitative results of adequate visibility.

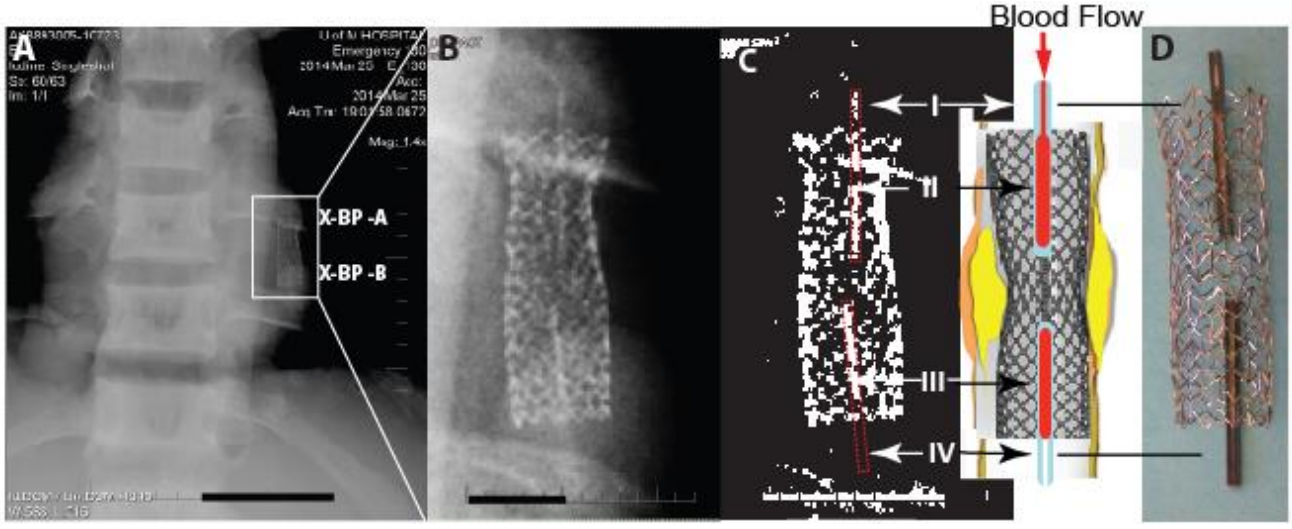

Figure 6.9: (A) An x-ray image of IV the X-BP microsensor placed inside a coronary stent placed on top of a human phantom's heart. (B) Zoom in X-ray snapshots of two X-BP microsensors attached at the both ends of a stent. (C) Post image processing of image B with histogram equilibration. (D) Picture of two X-BP microsensors with stent, A: Scale bar, 3 cm. B: Scale bar, 1 cm.

6.4.9 Resolving FFR

The clinical utility of the X-BP is to accurately determine a 20-25% pressure decrease across a stent that corresponds to an FFR of 0.8- 0.75 that is the clinical threshold that prompts intervention. To establish whether the X-BP can accomplish this we placed it in the pressure chamber, increased pressure from 0 to 150 mmHg in 15 mmHg increments and acquired radiographs as described above (F**igure 6.10A, 6.10B**). Histogram equalization, a common technique used in adjusting the image intensities to increase contrast [185] was performed in Matlab and Photoshop to create binary images (**Figure 6.10C**). Gridlines were superimposed and the number of pixels along the microfluidic gauge counted with eFilmLite 3.4 (Merge Healthcare, USA) x-ray image analysis software. Using the radio-opaque liquid column length versus pressure calibration obtained from the optical microscope we determined the spatial resolution of the x-ray images to be 48μm/pixel which corresponds to a sensor pressure resolution of 18.75 mmHg/pixel. Higher pressure resolutions and sensitivities can be obtained with a higher resolution x-ray imager. Because the resolution of the x-ray camera was not as high as the microscope image, the X-BP response curve (**Figure 6.10D**) is approximated as a linear function rather than a logarithmic one, likely due to sampling error. However, the resolution of X-BP is more than adequate to detect a pressure drop of 20- 25% across the physiologic pressure range, and produce a clinically meaningful output that corresponds to an FFR of 0.8- 0.75, or less.

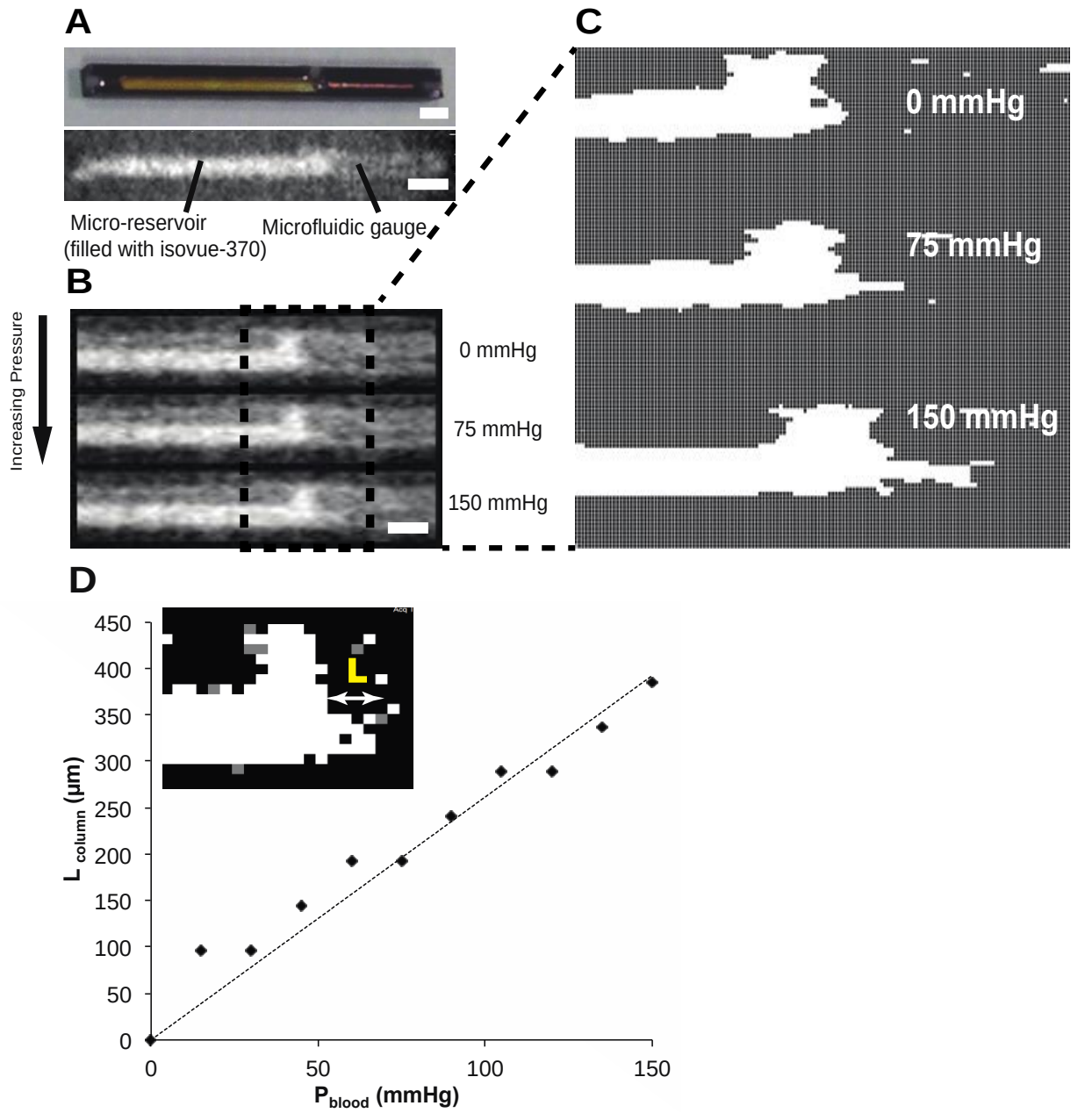

Figure 6.10: (A) An x-ray image of the X-BP microsensor. (B) X-ray snapshots of the micro-reservoir/gauge region of at three increasing pressures (600 µm diaphragm wide X-BP device). (C) Post image processing of image B with histogram equilibration. (D) Plot of measured gauge length (#pixels * x-ray resolution µm/pixel) versus applied pressure. A,B,C Scale bar: 1mm.

6.4.10 Clinical Imaging Considerations

Because of variability in anatomy, the angle of the x-rays may not always be

perpendicular to the direction of the stent. However, the FFR is the ratio of the length of the two sensors and the measurement is largely angle independent. In the occasion a stent is imaged in its short axis (“donut view”), the technician can change projections from frontal to lateral, which will ensure the entire length of the stent is imaged. The X-BP in these imaging experiments was placed partially within and partially outside the stent to evaluate different imaging scenarios. For in-vivo experiments it will be placed entirely within the stent.

Intimal hyperplasia and plaque build-up on the sensor membrane is expected to decrease the sensitivity of the sensor. However, in similar membranes the effect of 200 μm of intimal hyperplasia reduced the pressure (or the radial stress) of the membrane by only 6-7%[186]. Furthermore, neointimal hyperplasia is commonly symmetric across a stent and will have the same impact on both sensors, leaving their ratio largely unaffected. In-stent restenosis commonly occurs at the central articulation, the middle of the stent. The X-BP can be positioned with the membrane placed closer to the ends of the stent to avoid this problem.

The X-BP SNR and sensitivity are intimately linked to the height of the microfluidic gauge and the membrane deflection. Membrane deflection depends on the width of the membrane and the thickness of the membrane. We have demonstrated sufficient SNR and a potentially high sensor pressure resolution with existing x-ray technology. The attained Isovue displacement in the microfluidic gauge translates to a pressure resolution significantly lower than that available during invasive angiography, but adequate to identify a FFR of 0.75, the clinically relevant threshold for a screening test which will triage a patient to imaging, or angiography that can more accurately delineate the degree of stenosis and functional impairment. To take full advantage of the sensor and increase its resolution we will further increase the volume of fluid displaced by making the membrane slightly thinner and wider. Imaging technological

advancements such as improved x-ray receptor resolution that are on the way will help improve the performance of the sensor. The X-BP sensor itself can be improved through the use of a higher contrast agent than Isovue such as gold or tungsten nanoparticle colloidal suspensions [53][54]. These approaches meet imaging SNR requirements, but challenges exist to ensure the long-term stability of the suspension over a period of years.

The X-BP addresses an important, unmet clinical need in a cost effective manner. The FFR as a marker of myocardial perfusion is an important physiologic value that so far could not be attained non-invasively and inexpensively. Radiographs are widely available in community healthcare facilities and are reimbursed by CMS (Medicare, Medicaid) at approximately $41. The radiation to the patient from a chest radiograph is 0.1 mSV. For comparison, the background annual radiation at average altitude is 3mSv and in Colorado 4.5 mSV. The radiation from a chest CT is more than 7 mSv. The lifetime risk the patient may develop cancer from this radiation is minimal, defined as 1 in 100,000 to 1 in a million chances[189][190].

The X-BP allows for the periodic surveillance of a stent for in-stent restenosis. If the X-BP indicates an abnormality, the patient can be referred for additional imaging, such as a stress test, to confirm the abnormality and to angiography and PCI as needed, potentially reducing unnecessary, invasive and costly procedures. This approach rations healthcare resources and can be used widely as a screening test.

The innovation of the X-BP is its small size, which no other MEMS approach has been able to deliver. There is currently no sensor small enough for use in coronary arteries that range in size between 2 and 4mm. Although a number of engineering and imaging challenges remain, we are optimistic they can be overcome and we can soon implant the X-BP in an animal model.

6.5 Conclusions

We successfully designed, fabricated and tested a novel, x-ray detectable blood pressure microsensor, the X-BP sensor for periodical surveillance of coronary in-stent restenosis with clinical chest radiographs. The device can be produced with three simple lithography steps. Short-term interval follow-up of patients every 3 to 6 months is possible thanks to the low cost of radiographs and the negligible radiation exposure. With the availability of x-ray infrastructure in every hospital, we believe the X-BP sensor offers an elegant, cost-effective method to noninvasively assess coronary in-stent restenosis in a way not previously feasible. We anticipate this novel technology could solve other medical problems, such as peripheral arterial stent or ventricular shunt failure. Potentially, thanks to the fast time constant, the most important aspect of this technology could be the ability to provide real- time data for continuous monitoring of the FFR.

6.6 Acknowledgment

I want to thank Dr.Theodore Cosmo Marentis at the Department of Radiology, University of Michigan hospital for his help in X-ray detection concept and experiment. I would like to thank Prof. Paula Novelli for her help in performing the X-BP implantation surgery. I also want to thank Mostafa Ghannad-Rezaie for his PDMS experiment as a quick test in 2011. I would like to thank Microfluidics in Biomedical Sciences Training Program (T32 EB005582-05) for my fellowship and research support from the National Institutes of Health (NIH) and the NIH Director's New Innovator Award (DP2OD006458).

CHAPTER 7

Conclusions and Future Work

7.1 Conclusions

The research described in this thesis resulted in several ground breaking advances in optofluidic imaging and demonstrated a totally new type of passive blood pressure sensor. Our optofluidic lens array is simple to fabricate, cost effective and individual lenses in the array have the highest NA reported for hand held optical devices. Individual lenses in the array each have very high NA and resolution. We demonstrated that the lens array can be an add-on for a stereo microscope to increase resolution dramatically. Using the same lens array we also fabricated an integrated digital imaging system weighing less than 50 grams fitting in the palm of one hand. The integrated unit achieved even more impressive brightfield and fluorescent imaging results.

Our third project was in the area of blood pressure monitoring in coronary arteries. We successfully demonstrated a proof of concept implantable sensor which does not need any power and can be read out with a chest x-ray. The absence of any electronics, and x-ray read out of pressure was demonstrated for the first time in an implantable blood pressure sensor.

7.1.1 An Optofluidics Lens Array Microchip: A Compact Module for High Resolution, Large Field of View Imaging

Inspired by the conventional oil immersion microscope objective lenses with high numerical aperture (NA), we developed a simple-to-use, reusable and compact, microfabricated

imaging module for high resolution imaging applications. The key element of the design is the integration of a microfluidic chip with an array of 16 half liquid-immersed ball mini-lenses (1.77 refractive index, 1 mm diameter). The integrated chip–termed the μOIL chip - mimics the working principle of the front end of expensive, oil-immersion microscope objectives. The μOIL chip alone has a maximum numerical aperture of 1.2 and a magnification of 130X. When compared to other microlens techniques, the μOIL chip has by far the highest NA. The beauty of our design is its simplicity (only two masks for fabrication) and use of off the shelf high index sapphire lenses as opposed to using complicated fabrication steps to achieve reasonable quality optical performance.

7.1.2 An Add-on Microchip Module to Stereomicroscope for High Resolution Imaging

The μOIL chip can be placed directly on the sample of interest and then imaged under a standard stereomicroscope by simply adjusting the focus and/or the magnification of the stereomicroscope. We demonstrated that, when it is used as an add-on module to a stereo microscope, it can resolve submicron micron features (maximum resolution of ~0.7 μm) from a variety of biological samples and be capable of obtaining simultaneous images from multiple lenses. The field of view of each lens in the array is 60-140 μm diameter. The μOIL chip brings high resolution (~0.7μm), large field of view imaging capabilities to research and medical laboratories and clinics where a stereomicroscope is the only available imaging tool. The chip can be reused or is of low cost enough to be disposable.

7.1.3 A Handheld µOIL –Based System for Cell Imaging and Counting

We have developed a pocket size (4cmx4cmx4cm), lightweight (50 gram) µOIL microscope using a compact µOIL optics based with high resolution of 0.43 µm. This microscope can image in both bright-field and fluorescence mode. We demonstrated its capability by imaging individual cells at the submicron level and used it for counting a variety of cells ranging in concentration from 200 cells/µL to 5 million cells/µL. This range covers both the red blood cells from dilute whole blood and white blood cells. Since the concentration of red blood cells is high (4-6 million cells/ µL), it can be diluted by 100 and an accurate count can be performed from a single lens. For white blood cells (4500-10,000 cells/ µL), we used all 16 lenses to image over an area of 0.64mm^2 (at the volume of 64 nL) and automated counting to obtain reliable counting statistics. High resolution imaging with the µOIL system for diagnostic purposes was demonstrated by imaging sickle blood cells, P.*vivex* and P.*falciparium* malaria parasite infected red blood cells in bright field imaging mode. Flexibility of µOIL imaging system was also demonstrated for fluorescence imaging of 4µm spheres and peripheral mononuclear THP-1 cells by the addition of an emission, an excitation filter and a condenser lens in trans- illumination configuration.

The beauty of our integrated handheld system is its simplicity, low cost, and ease of fabrication (only two mask steps). This beauty is complimented by equally impressive performance. Our hand held system's resolution is less than a factor of two away from the theoretical diffraction limit this is far better than the best reported literature value of 1 µm resolution of the state of the art hand held optical systems[89], Florescence imaging with our hand held system in trans illumination mode is also very simple.

7.1.4 An Implantable, X-Ray Based Blood Pressure Microsensor for Coronary In-Stent Restenosis Surveillance and Prevention

We designed, fabricated and tested a novel, x-ray readable blood pressure microsensor, the X-BP sensor for periodic surveillance of coronary in-stent restenosis with clinical chest radiographs. The device can be produced with a three simple mask microfabrication technique from Si, SiO_2, Si_3N_4 (all biocompatible[184]). The X-BP has a column of radio-opaque liquid that changes its length with blood pressure. The X-BP membrane was modeled and the x-ray Signal-to-Noise ratio (SNR) of different sensor dimensions was optimized. As a result, the optimum size of the microfluidic gauge is 250 μm thick x 250 μm wide. We tested two designs of the X-BP sensor, with 400μm and 600μm wide membranes, 0.5μm thick and 8.5 mm long. The experimental results indicate that the X-BP sensors accurately responds in the clinically relevant pressure range (0-150 mmHg), as predicted by the analytical model. We evaluated the possibility of device failure with COMSOL software, the maximum von Mises stress is ~413 MPa at 200mmHg which is one order of magnitude lower than the silicon nitride yield strength (5.5GPa). The X-BP does not exhibit any hysteresis and has a time response constant less than 32 ms. The resolution of the x-ray images is 48μm/pixel, which corresponds to a sensor pressure resolution of 18.75 mm Hg/pixel. The sensor has a potential dynamic range of 0-200 mmHg, and can reliably resolve the clinically important pressure drop of 20-25% across the dynamic range for an FFR value of 0.8 to 0.75 or less. As a first generation proof of concept passive sensor the device shows a lot of promise and warrants further research.

7.2 Future Work

7.2.1 An Optofluidics Lens Array Microchip: A Compact Module for High Resolution, Large Field of View Imaging

7.2.1.1 Increase field of view from individual lens

Even though, high resolution optical imaging can be obtained through μOIL chip, the usable field of view (FOV) is still in the range of 200 μm diameter per lens. The FOV can be increased further by integrating an array of apertures on top of the μOIL chip to limit interference between neighboring lenses. To find an optimized aperture size, a ray tracing software such as Zemax can be used. Another improvement which can be done on the μOIL chip is increasing image area/chip dimensions. Ball-lenses and Microwells can be arranged in high density such as in hexagonal close packing. For the same array size of 6x4, arrangement configuration in **figure 7.1A** will result in a chip of 7.5 mm long x 4.5 mm wide to give a ~ 0.96mm^2 FOV area. The same FOV can also be obtained from a compact μOIL chip designed over a chip size of 7.5 mm long x 3.8 mm wide) arranging ball-lenses in the hexagonal close packed arrangement **(Figure 7.1B)**.

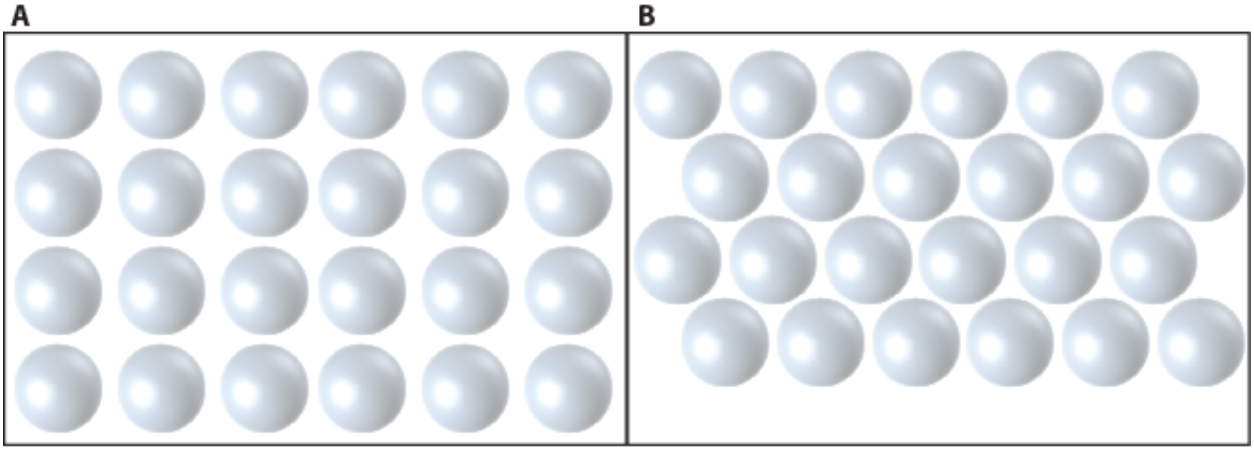

Figure 7.1: Two methods of μOIL chip design. (A) in original arrangement of 6x4 array which can take up the area of 7.5 mm long x 4.5 mm wide of the μOIL chip (B) compact overlapping diagonal arrangement to reduce chip real estate to 7.5 mm long x 3.8 mm wide μOIL chip area.

7.2.1.2 Find a better manufacturing method to attain an identical focal plane from μOIL chip

Imperfections in the microfabrication and mini-lens assembly process, result in a lens-to-lens variation of the focal length within the array. Tighter quality control of the lens diameters and the depth of the microwells will improve the focal plane uniformity of the array. While we have not quantified differences in lens diameters and chamber depths variations in both are not expected to be more than ten microns. However, with a short focal length of 625 μm the depth of focus is less than one micron for high index sapphire lenses.

7.2.1.3 Replacing the Immersion Oil with Norland optical epoxy

In the μOIL chip, oil was used as the immersion liquid. The refractive index (n) of oil is 1.516 which matches the refractive index of glass coverslip. However, over time, oil can evaporate, spill or it can get dusty thus deteriorate the quality of image. Refilling the oil or

cleaning the μOIL chip can be a challenging task. A better material with similar refractive index such as Norland optical light sensitive epoxy 61 (n= 1.527, viscosity ~300 cps) can be used to replace oil. This epoxy comes in liquid form; therefore fluidic channel network and microwells can be filled with it. To transform the liquid Norland epoxy to solid after the ball lenses are assembled, the μOIL chip can be exposed to UV light and the epoxy will crosslink and solidify. Cleaning can be achieved easily by blowing the μOIL chip with dry air or nitrogen.

7.2.2 A digital handheld μOIL microscope for point of care diagnostics

The digital handheld μOIL microscope can be developed as a standalone device. The number of cells in the viewing area can be displayed on the screen. Currently, the μOIL imaging device has a CMOS sensor that connects to a computer. The images are captured and then fed to Matlab for cell counting. An LCD display can also be added to the standalone μOIL microscope to enable an instantaneous imaging as it can be used for clinical diagnostics. More electronics such as imaging analysis software can be added to the device so that it can be used as standalone cell imaging/ counting instrument. Bluetooth or wireless telemetry function (similar to cell phone or camera) can be added in order to send/save images to other sources (e.g. consulting for second opinion, storage).

7.2.3 Implantable, X-Ray Based Blood Pressure Microsensor for Coronary In- Stent Restenosis Surveillance and Prevention

7.2.3.1 Au nanoparticle colloidal suspensions, a better contrast Agent

Currently, the spatial resolution of the x-ray images is 48μm/pixel which corresponds to a sensor pressure resolution of 18.75 mmHg/pixel. Higher pressure resolutions and sensitivities can be obtained with a higher resolution x-ray imager. The X-BP sensor itself can be improved through the use of a stronger contrast agent than Isovue (iodine-based contrast agent) such as

gold (Au) nanoparticle colloidal suspension. Au has a higher atomic number than Iodine (Au,79 vs I, 53) and higher absorption coefficient (at 100 keV: gold: 5.16 cm^2 g^{-1}; iodine: 1.94 cm^2 g^{-1}; soft tissue: 0.169 cm^2 g^{-1}; and bone: 0.186 cm^2 g^{-1}). Au nanoparticle colloidal suspension approach can provide about 2.7 times higher contrast per unit weight than iodine [191]. This will improve the SNR and resolution, but the long-term stability of the suspension over a period of years has to be tested.

7.2.3.2 Optimization of the microfluidic gauge design

A new design should incorporate a larger volume air pocket at the end of the microfluidic gauge so that the sensitivity does not decrease rapidly with increasing pressure. Because the gauge tube is initially sealed at 1 atm (760 mmHg), it cannot be compressed by more than 30% since the maximum blood pressure is on the order of 200 mmHg which results in almost zero sensitivity at the high end. If we have a large (compared to the gauge volume) volume air packet at the tip of the gauge tube the change in the sensitivity will be minimal.

Different biocompatible materials with low young's modulus can be used in place of silicon nitride. Diaphragm with lower young's modulus would give slightly higher sensitivity to pressure.

7.2.3.3 Long-term study in vitro and in vivo

In vitro, the robustness of the system needs to be checked by cycling the device through pressure cycles for millions of times to estimate it's lifetime.

In *vivo*, the device can be implanted in animals to evaluate the response of the liquid in the gauge to pressure due to the encapsulation and long-term biocompatibility. The sensor has to be attached to the stent. The methods of positioning of the sensor and attachment to the stent need to be studied. We did a first try at implanting the device into the coronary artery of a pig,

however, the glue used to attach the sensor to the stent failed after a couple of days. A better method of attaching to the stent may be needed.

In order to understand the effect of Neointimal Hyperplasia on the device diaphragm response to pressure, we did COMSOL simulation of the maximum deflection of thin film low stress silicon nitride diaphragm with Neointimal deposit at different thickness (100-400 μm). The change of the maximum deflection due to thickness of endothelial cells on the device's diaphragm is shown in table 7.1. At 150 mmHg, 400 μm Endothelial cell deposit causes ~ 4.37% change in maximum diaphragm deflection.

Table 7.1: Maximum diaphragm deflection value, with and without endothelial tissue encapsulation, response at different pressure.

Pressure (Pa)	Pressure (mmHg)	Diaphragm deflection (No endothelial)	Endothelial 100 μm	Endothelial 200 μm	Endothelial 300 μm	Endothelial 400 μm
5000	37.5	5.74	5.69	5.57	5.49	5.44
10000	75	7.26	7.21	7.11	7.02	6.96
15000	112.5	8.32	8.26	8.18	8.06	7.96
20000	150	9.16	9.11	9.02	8.89	8.76

Note: Endothelial Tissue parameter: Young's modulus = 6 MPa, Poisson's ratio = 0.495 Tissue density = 1.06 g/cm^3

APPENDICES

Appendix A

Fabrication Process Flow of the Microlens array

There are 2 masks design for Microlens array fabrication.

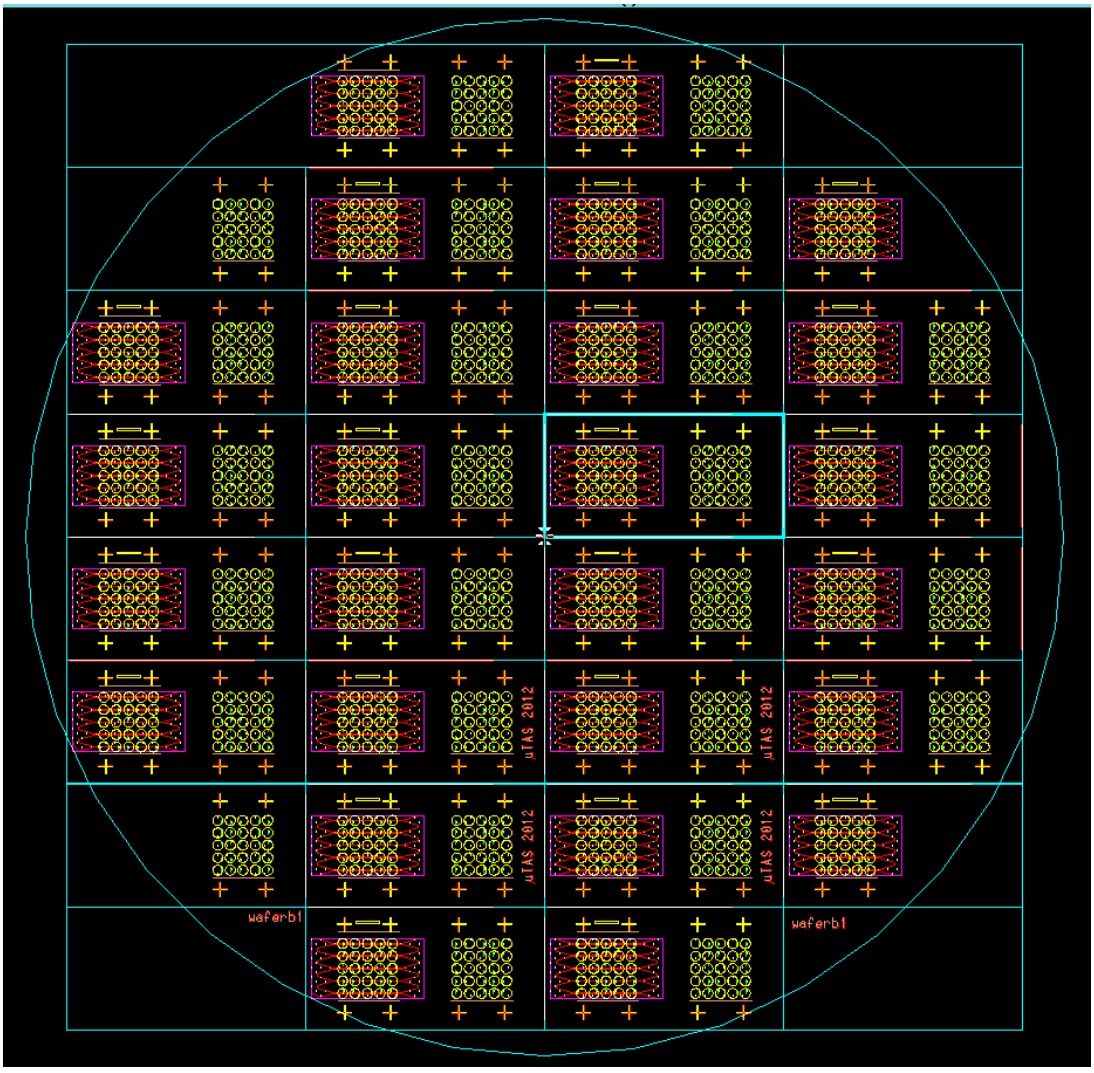

Figure A1: Image of overall µOIL array design on wafer

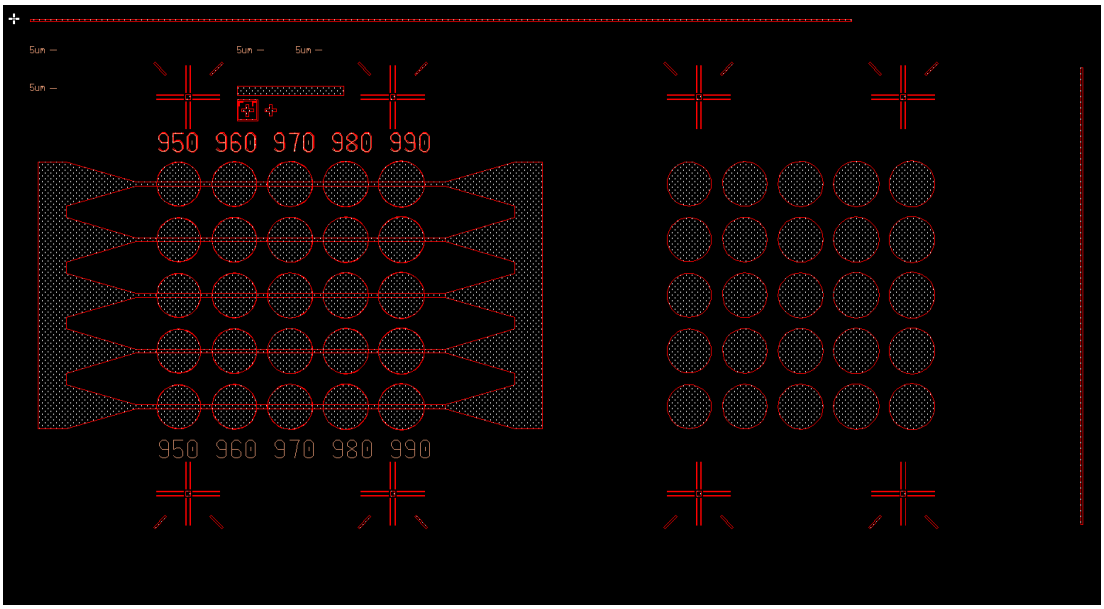

Figure A2: Mask 1, Microfluidic network and microwells array together.

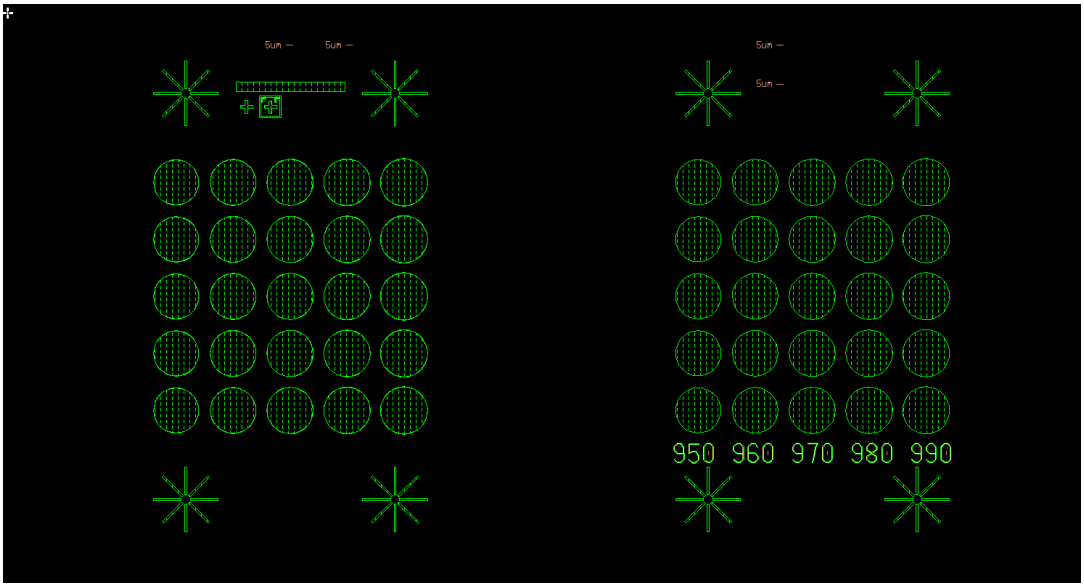

Figure A3: Mask 2, Microwells array pattern.

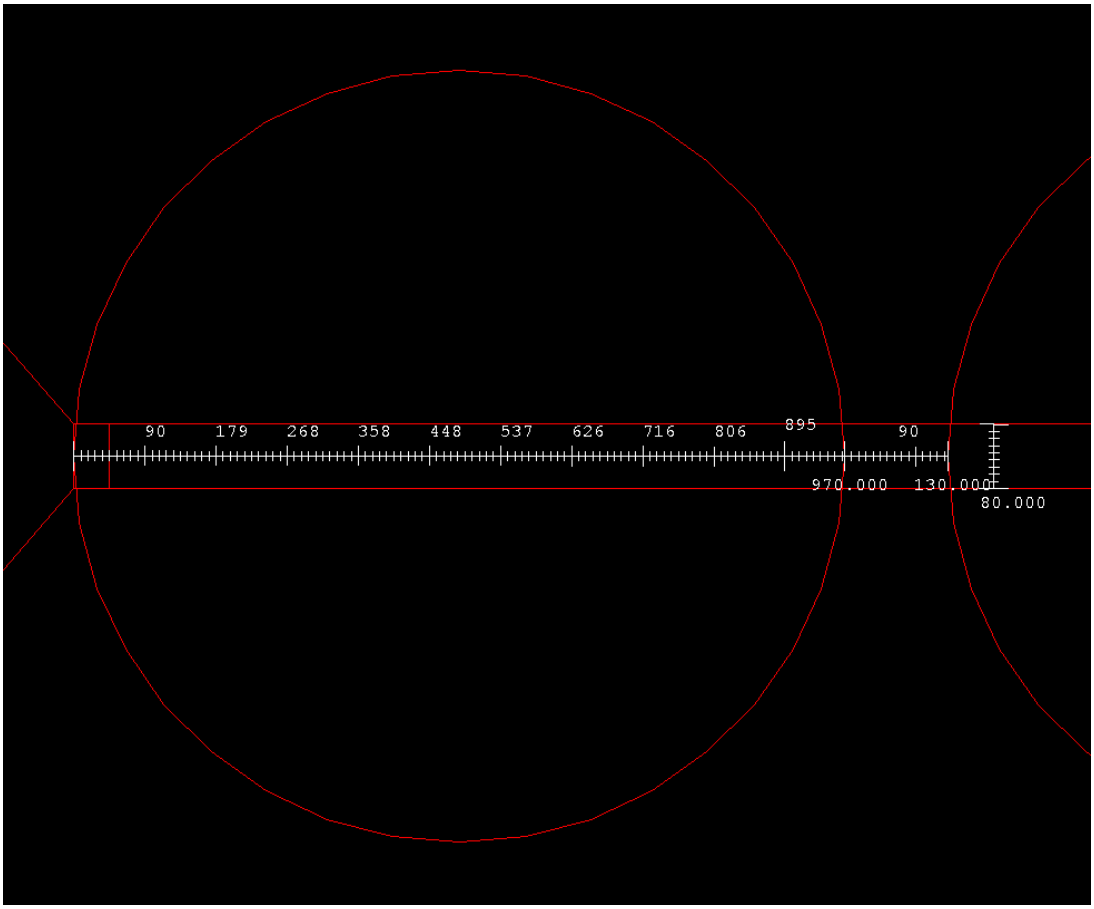

Figure A4: Details dimension of μOIL array: Microwell diameter can vary from 950 to 990 μm, microfluidic channel width is 80μm. Currently distance between each microwells is 130μm. The optimized diameters that obtained best image are 960 and 970 μm. Die size is 1cmx1cm.

Fabrication process is explained under 3.4 Microfabrication. Details process is explained below:

1 Start with Silicon substrate (400 μm thick)

2 Grow masking oxide 2500Å

a. Prefurnace Clean (using NH_3OH, H_2O_2 and HCl)

b. Thermal Oxidation for 2500 Å

i. Dry/Wet/Dry for 10min/35 min/10 min at 1100°C

3 Pattern Mask #1 (Figure A2) Opening microfluidic network and microwells

Lithography with photoresist 1813

i. Note: SPR220 can be used in place of 1813 however, you need to be careful with very hydrophobic surface of SPR220, so descum process is a must before wet etch)

ii. HMDS/ Spin PR at @4krpm

iii. Soft bake at 90°C hotplate for 1 min

iv. Exposure for 6sec at 20mW/cm^2

v. Develop in MF319 for 1min/ rinse 2 min spin/ dry

vi. Hard bake at 110°C for 2 min

4 Descum in O_2 plasma at 50 mW for 2 min.

5 BHF etch oxide 2:45 min Etch rate ~ 900-1000Å/min

6 Inspect with nanospec (or ellipsometer) to see if all SiO2 film on Si is gone. The surface should look gray and nanospec should show ~10Å

7 Strip PR in hot PRS2000 for 5 min/ rinse 5 min/ spin/dry

8 Pattern Mask #2 (Figure A3) for microwells array

Lithography with SPR 220

i. HMDS/ Spin SPR220 for 5 µm using ACS automatic coating tool

ii. Soft bake at 90°C for 1:30 min

iii. Exposure for 10.5 sec at 20mW/cm^2

iv. Wait for 10 min

v. Post exposure bake at 115°C for 2 min

vi. Develop in MF319 for 1min/ rinse 2 min spin/ dry

vii. Check thickness of PR using Dektek

9 DRIE in Pegasus tool, using recipe #3

i. Ar descum for 20 sec

ii. Etch down 250 μm

iii. Using Dektek to check the etch rate

10 Strip PR

a. O2 RIE in Plasma therm

i. 100 W, O_2 100 sccm, 10 min

b. put in Hot PRS2000 for 15 min/ rinse 5 min/ spin/dry

11 DRIE in Pegasus tool, using recipe #3

i. Ar descum for 20 sec

ii. Etch down until the microwells are etched through.

iii. Using Dektek to check the total depth in microfluidic

iv. Using Zygo surface profilometer (or dekteck) to check microwells diameter

Appendix B

The optical simulation software (OSLO LT) is used to calculate effective focus length and numerical aperture of Microlens (Figure B.1)

A

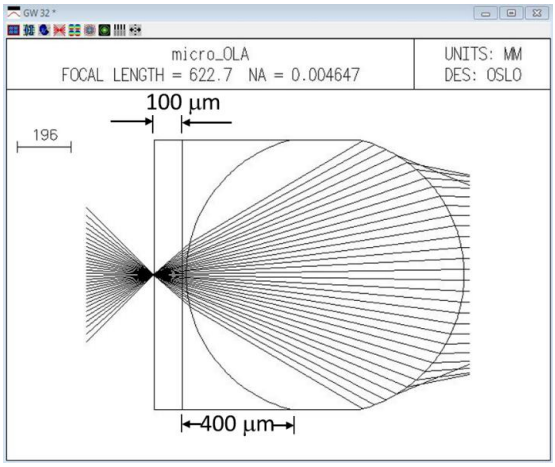

B

Surface Data

4.0

Gen | Setup | Wavelength | Variables | Draw On | Group | Notes

Lens: No name Efl 622.660625

Ent beam radius 4.000000 Field angle 1.9223e-07 Primary wavln 0.587560

SRF	RADIUS		THICKNESS		APERTURE RADIUS		GLASS		SPECIAL
OBJ	2.000000		4.000000		4.0000e-06		BLOOD	M	
1	1.0000e+10		75.000000		485.000000		GLASS1	M	
2	1.0000e+10		9.600000		485.000000		OIL	M	
3	500.000000		1.0000e+03		485.000000		GLASS3	M	
AST	-500.000000		0.000000		485.000000	A	AIR		
5	0.000000		0.000000		485.000000		AIR		
IMS	0.000000		0.000000		850.043039	S			

C

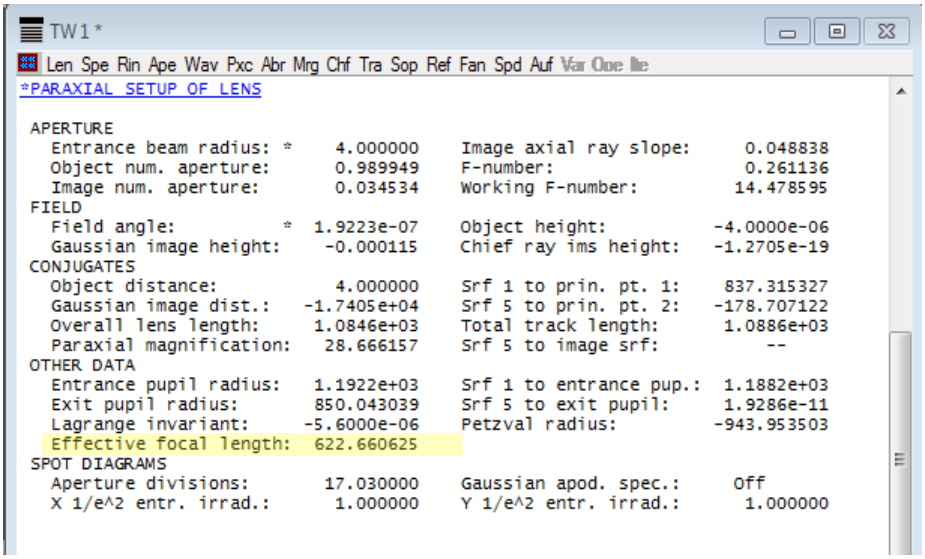

Figure B.1: Simulation of microlens' focal length and numerical aperture using OSLO software. (A) A ray diaphragm demonstrating the microlens' focus point. (B) Lens surface data spreadsheet for entering individual material properties and geometrical structure. (C) Prescription data of surface data in (B).

Appendix C

The Matlab Software for counting cells from the image obtained from microfabricated microlens array

```
close all;clear all;clc;
%read the image and rotate to straighten it out
% image = imread('2000 count1.bmp');
image = imread('Image name.bmp');
image = rgb2gray(image);
figure,imshow(image);
angle = horizon((image),0.1,'hough');
image_rot=imrotate(image, -angle,'bicubic');
image_rot_orig=image_rot;
figure,imshow(image_rot);
title('Rotated Aligned Image');
% marking two points to calculate the image pixel spacing
title('Enter the start and end points of a sub grid to determine
resolution');
[x1,y1] = ginput;
[x2,y2] = ginput;
% x1=857.2575;x2 =908.2806;y1=557.2520;y2=560.2534;
Pos=[x1 x2;y1 y2]
D=dist(Pos);
distance = D(1,2);
conversion = distance/50;
length= input('Input the value of height of TROI in um: ');
length = round(length*conversion);
%cropping a circle
title('Select the upper left corner of the first cell:');
[c1 c2] = ginput;
imageSize=size(image_rot);
mask=zeros(imageSize(1,1),imageSize(1,2));
for i=1:length
    for j=1:length
        mask(round(i+c2),round(j+c1))=1;
        mask(round(i+c2),round(j+c1)+515)=1;
        mask(round(i+c2),round(j+c1)+2*515)=1;
        mask(round(i+c2),round(j+c1)+3*515)=1;
        mask(round(i+c2)+515,round(j+c1))=1;
        mask(round(i+c2)+515,round(j+c1)+515)=1;
        mask(round(i+c2)+515,round(j+c1)+2*515)=1;
        mask(round(i+c2)+515,round(j+c1)+3*515)=1;
```

```
        mask(round(i+c2)+515*2,round(j+c1))=1;
        mask(round(i+c2)+515*2,round(j+c1)+515)=1;
        mask(round(i+c2)+515*2,round(j+c1)+2*515)=1;
        mask(round(i+c2)+515*2,round(j+c1)+3*515)=1;
        mask(round(i+c2)+515*3,round(j+c1))=1;
        mask(round(i+c2)+515*3,round(j+c1)+515)=1;
        mask(round(i+c2)+515*3,round(j+c1)+2*515)=1;
        mask(round(i+c2)+515*3,round(j+c1)+3*515)=1;
    end
end
figure,imshow(mask);
for i=1:imageSize(1)
     for j=1:imageSize(2)
       if (mask(i,j) == 0)
           image_rot(i,j)=0;
       end
     end
 end
 figure,imshow(image_rot);

 cell1=image_rot(round(c2):round(c2+length),round(c1):round(length+c1));
 figure,imshow(cell1);
 cell1=imadjust(cell1);
 figure,imshow(cell1);
  [centers1, radii1] = imfindcircles(cell1,[1
6],'ObjectPolarity','dark','Sensitivity',0.9)
%   [centers1, radii1] = imfindcircles(cell1,[2
12],'ObjectPolarity','bright')
figure,imshow(cell1);
 h1 = viscircles(centers1,radii1);
 count1=size(radii1,1);


cell2=image_rot(round(c2):round(c2+length),round(c1+550):round(length+c1+550)
);
figure,imshow(cell2);
 cell2=imadjust(cell2);
figure,imshow(cell2);
 [centers2, radii2] = imfindcircles(cell2,[1
6],'ObjectPolarity','dark','Sensitivity',0.9)
%  [centers2, radii2] = imfindcircles(cell2,[2 12],'ObjectPolarity','bright')
figure,imshow(cell2);
 h2 = viscircles(centers2,radii2);
 count2=size(radii2,1);


cell3=image_rot(round(c2):round(c2+length),round(c1+2*550):round(length+c1+2*
550));
figure,imshow(cell3);
 cell3=imadjust(cell3);
figure,imshow(cell3);
 [centers3, radii3] = imfindcircles(cell3,[1
6],'ObjectPolarity','dark','Sensitivity',0.9)
%  [centers3, radii3] = imfindcircles(cell3,[2 12],'ObjectPolarity','bright')
figure,imshow(cell3);
```

```
 h3 = viscircles(centers3,radii3);
 count3=size(radii3,1);


cell4=image_rot(round(c2):round(c2+length),round(c1+3*550):round(length+c1+3*
550));
figure,imshow(cell4);
 cell4=imadjust(cell4);
figure,imshow(cell4);
 [centers4, radii4] = imfindcircles(cell4,[1
6],'ObjectPolarity','dark','Sensitivity',0.9)
%  [centers4, radii4] = imfindcircles(cell4,[2 12],'ObjectPolarity','bright')
figure,imshow(cell4);
 h4 = viscircles(centers4,radii4);
 count4=size(radii4,1);


cell5=image_rot(round(c2+550):round(c2+length+550),round(c1):round(length+c1)
);
figure,imshow(cell5);
 cell5=imadjust(cell5);
figure,imshow(cell5);
 [centers5, radii5] = imfindcircles(cell5,[1
6],'ObjectPolarity','dark','Sensitivity',0.9)
%  [centers5, radii5] = imfindcircles(cell5,[2 12],'ObjectPolarity','bright')
 figure,imshow(cell5);
 h5 = viscircles(centers5,radii5);
 count5=size(radii5,1);


cell6=image_rot(round(c2+550):round(c2+length+550),round(c1+550):round(length
+c1+550));
figure,imshow(cell6);
 cell6=imadjust(cell6);
figure,imshow(cell6);
 [centers6, radii6] = imfindcircles(cell6,[1
6],'ObjectPolarity','dark','Sensitivity',0.9)
%  [centers6, radii6] = imfindcircles(cell6,[2 12],'ObjectPolarity','bright')
 figure,imshow(cell6);
 h6 = viscircles(centers6,radii6);
 count6=size(radii6,1);


cell7=image_rot(round(c2+550):round(c2+length+550),round(c1+2*550):round(leng
th+c1+2*550));
figure,imshow(cell7);
 cell7=imadjust(cell7);
figure,imshow(cell7);
 [centers7, radii7] = imfindcircles(cell7,[1
6],'ObjectPolarity','dark','Sensitivity',0.9)
%  [centers7, radii7] = imfindcircles(cell7,[2 12],'ObjectPolarity','bright')
figure,imshow(cell7);
 h7 = viscircles(centers7,radii7);
 count7=size(radii7,1);
```

```
cell8=image_rot(round(c2+550):round(c2+length+550),round(c1+3*550):round(leng
th+c1+3*550));
figure,imshow(cell8);
 cell8=imadjust(cell8);
 figure,imshow(cell8);
 [centers8, radii8] = imfindcircles(cell8,[1
6],'ObjectPolarity','dark','Sensitivity',0.9)
%  [centers8, radii8] = imfindcircles(cell8,[2 12],'ObjectPolarity','bright')
 figure,imshow(cell8);
 h8 = viscircles(centers8,radii8);
 count8=size(radii8,1);


cell9=image_rot(round(c2+2*550):round(c2+length+2*550),round(c1):round(length
+c1));
 figure,imshow(cell9);
 cell9=imadjust(cell9);
 figure,imshow(cell9);
 [centers9, radii9] = imfindcircles(cell9,[1
6],'ObjectPolarity','dark','Sensitivity',0.9)
%  [centers9, radii9] = imfindcircles(cell9,[2 12],'ObjectPolarity','bright')
 figure,imshow(cell9);
 h9 = viscircles(centers9,radii9);
 count9=size(radii9,1);


cell10=image_rot(round(c2+2*550):round(c2+length+2*550),round(c1+550):round(l
ength+c1+550));
figure,imshow(cell10);
 cell10=imadjust(cell10);
figure,imshow(cell10);
 [centers10, radii10] = imfindcircles(cell10,[1
6],'ObjectPolarity','dark','Sensitivity',0.9)
%  [centers10, radii10] = imfindcircles(cell10,[2
12],'ObjectPolarity','bright')
 figure,imshow(cell10);
 h10 = viscircles(centers10,radii10);
 count10=size(radii10,1);


cell11=image_rot(round(c2+2*550):round(c2+length+2*550),round(c1+2*550):round
(length+c1+2*550));
figure,imshow(cell11);
 cell11=imadjust(cell11);
figure,imshow(cell11);
 [centers11, radii11] = imfindcircles(cell11,[1
6],'ObjectPolarity','dark','Sensitivity',0.9)
%  [centers11, radii11] = imfindcircles(cell11,[2
12],'ObjectPolarity','bright')
figure,imshow(cell11);
 h11 = viscircles(centers11,radii11);
 count11=size(radii11,1);
```

```
cell12=image_rot(round(c2+2*550):round(c2+length+2*550),round(c1+3*550):round
(length+c1+3*550));
figure,imshow(cell12);
 cell12=imadjust(cell12);
figure,imshow(cell12);
 [centers12, radii12] = imfindcircles(cell12,[1
6],'ObjectPolarity','dark','Sensitivity',0.9)
%  [centers12, radii12] = imfindcircles(cell12,[2
12],'ObjectPolarity','bright')
 figure,imshow(cell12);
 h12 = viscircles(centers12,radii12);
 count12=size(radii12,1);


cell13=image_rot(round(c2+3*515):round(c2+length+3*515),round(c1):round(lengt
h+c1));
 figure,imshow(cell13);
 cell13=imadjust(cell13);
 figure,imshow(cell13);
 [centers13, radii13] = imfindcircles(cell13,[1
6],'ObjectPolarity','dark','Sensitivity',0.9)
%  [centers13, radii13] = imfindcircles(cell13,[2
12],'ObjectPolarity','bright')
 figure,imshow(cell13);
 h13 = viscircles(centers13,radii13);
 count13=size(radii13,1);


cell14=image_rot(round(c2+3*550):round(c2+length+3*550),round(c1+550):round(l
ength+c1+550));
 figure,imshow(cell14);
 cell14=imadjust(cell14);
 figure,imshow(cell14);
 [centers14, radii14] = imfindcircles(cell14,[1
6],'ObjectPolarity','dark','Sensitivity',0.9)
%  [centers14, radii14] = imfindcircles(cell14,[2
12],'ObjectPolarity','bright')
 figure,imshow(cell14);
 h14 = viscircles(centers14,radii14);
 count14=size(radii14,1);


cell15=image_rot(round(c2+3*550):round(c2+length+3*550),round(c1+2*550):round
(length+c1+2*550));
figure,imshow(cell15);
 cell15=imadjust(cell15);
figure,imshow(cell15);
 [centers15, radii15] = imfindcircles(cell15,[1
6],'ObjectPolarity','dark','Sensitivity',0.9)
%  [centers15, radii15] = imfindcircles(cell15,[2
12],'ObjectPolarity','bright')
 figure,imshow(cell15);
 h15 = viscircles(centers15,radii15);
```

```
 count15=size(radii15,1);


cell16=image_rot(round(c2+3*550):round(c2+length+3*550),round(c1+3*550):round
(length+c1+3*550));
 figure,imshow(cell16);
 cell16=imadjust(cell16);
 figure,imshow(cell16);
 [centers16, radii16] = imfindcircles(cell16,[1
6],'ObjectPolarity','dark','Sensitivity',0.9)
%  [centers16, radii16] = imfindcircles(cell16,[2
12],'ObjectPolarity','bright')
 figure,imshow(cell16);
 h16 = viscircles(centers16,radii16);
 count16=size(radii16,1);


total_cells=count1+count2+count3+count4+count5+count6+count7+count8+count9+co
unt10+count11+count12+count13+count14+count15+count16;

% %  cell17=image_rot_orig;
% %  figure,imshow(cell17);
% %  cell17=imadjust(cell17);
% %  figure,imshow(cell17);
% % %  cell17 = imsharpen(cell17);
% % %  figure,imshow(cell17);
% % % %correction for blur
% % %  [centers2, radii2] = imfindcircles(cell2,[2
12],'ObjectPolarity','dark','Sensitivity',0.9)
% %  [centers17, radii17] = imfindcircles(cell17,[2
12],'ObjectPolarity','bright','Method','twostage')
% %  figure,imshow(cell17);
% %  h17 = viscircles(centers17,radii17);
% %  count17=size(radii17,1);

% title('Selected ROI of Radius 100um form original image');
% imwrite(image_rot,'cellc_image_WBC1_151_6_best','bmp');
```

Appendix D

Fabrication Process Flow of MEMS X-Ray Pressure Sensor

There are 3 masks design for X-Ray readable pressure sensor. Overall details is descripted in 6.3.2 Microfabrication of X-Ray readable pressure sensor.

A

B

Figure D1: A Mask 1, Microreservoir and Microfluidic gauge including connection neck, B Mask 2, Microreservoir and Microfluidic gauge

Fabrication Process Flow

1 Silicon wafer (400μm thick)

2 Grow masking oxide 2500Å

   a. Prefurnace Clean

   b. Thermal Oxidation for 2500 Å

      i. Dry/Wet/Dry for 10min/35 min/10 min at 1100°C

3 Pattern Mask #1 Opening microreservoir and microfluidic gauge including connection neck

   Lithography with photoresist 1813

      i. Note: SPR220 can be used in place of 1813 however, you need to be careful with very hydrophobic surface of SPR220, so descum process is a must before wet etch)

      ii. HMDS/ Spin PR at @4krpm

      iii. Soft bake at 90°C hotplate for 1 min

      iv. Exposure for 6sec at 20mW/cm^2

      v. Develop in MF319 for 1min/ rinse 2 min spin/ dry

      vi. Hard bake at 110°C for 2 min

4 Descum in O_2 plasma at 50 mW for 2 min.

5 BHF etch oxide 2:45 min Etch rate ~ 900-1000Å/min

6 Inspect with nanospec (or ellipsometer) to see if all SiO_2 film on Si is gone. The surface should look gray and nanospec should show ~10Å

7 Strip PR in hot PRS2000 for 5 min/ rinse 5 min/ spin/dry

8 Pattern Mask #2 Recess for microreservoir and microfluidic gauge, blocking connection neck

Lithography with SPR 220

i. HMDS/ Spin SPR220 for 5 µm using ACS automatic coating tool
ii. Soft bake at 90°C for 1:30 min
iii. Exposure for 10.5 sec at 20mW/cm^2
iv. Wait for 10 min
v. Post exposure bake at 115°C for 2 min
vi. Develop in MF319 for 1min/ rinse 2 min spin/ dry
vii. Check thickness of PR using Dektek

9 DRIE in Pegasus tool, using recipe #3

i. Ar descum for 20 sec
ii. Etch down 230 µm
iii. Using Dektek to check the etch rate

10 Strip PR

a. O2 RIE in Plasma therm
   i. 100 W, O_2 100 sccm, 10 min
b. put in Hot PRS2000 for 15 min/ rinse 5 min/ spin/dry

11 DRIE in Pegasus tool, using recipe #3

i. Ar descum for 20 sec
ii. Etch down 20 µm (this will form the neck connection)
iii. Using Dektek to check the total depth in microreservoir and neck

12 Using Zygo surface profilometer (or dekteck) to check surface roughness

13 Grow oxide 1µm to smooth the micro-reservoir surface

a. PFC

b. Thermal Oxidation for 1µm

i. Dry/Wet/Dry for 10min/4 hour/10 min at 1100°C

14 Strip SiO_2 in HF for 10 min

15 Using Zygo surface profilometer (or dekteck) to check surface roughness

16 LPCVD deposit 2000Å SiO_2 and 5000Å low stress SiN

a. PFC

b. LPCVD 2000Å SiO_2 in S2T3 tube

c. LPCVD low stress 5000Å SiN in S2T4 tube

Note: This LPCVD deposition will coated bothsides of the wafer.

17 Anodic bonding process Si (400µm)and Glass (200µm) at 350Volt.

18 Pattern Mask #3 Pattern opening reservoir mask (Backside of Silicon wafer)

Lithography with SPR 220

i. HMDS/ Spin SPR220 for 5 µm using ACS automatic coating tool

ii. Soft bake at 90°C for 1:30 min

iii. Exposure for 10.5 sec at 20mW/cm^2

iv. Wait for 10 min

v. Post exposure bake at 115°C for 2 min

vi. Develop in MF319 for 1min/ rinse 2 min spin/ dry

vii. Check thickness of PR using Dektek

19 DRIE in Pegasus tool, using recipe: oxide and nitride etch

i. Ar descum for 20 sec

ii. Etch LPCVD low stress 5000Å SiN and LPCVD 2000Å SiO_2 Films

20 Strip PR

a. O2 RIE in Plasma therm

i. 100 W, O_2 100 sccm, 10 min

b. put in Hot PRS2000 for 15 min/ rinse 5 min/ spin/dry

21 Dice wafer according to the size of individual chip

22 Prepare to etch Silicon to open low stress SiN film.

a. Bond individual X-BP chip to Silicon wafer using conductive wax

23 DRIE in Pegasus tool, using recipe #1 (high selectivity Si over SiO_2)

i. Ar descum for 20 sec

ii. Etch down ~150 μm until see the reservoir diaphragm is cleared of Si

iii. Rinse in Acetone/IPA Store devices in IPA

Appendix E

Matlab code for removing background noise (Morphological Reconstruction) which applied on the X-Ray image (Figure 5.9)

```
%%
[file, path] = uigetfile('*.bmp', 'Select the image' );
im = imread([path, file]);
%%
im2 = im2double(im);
im2 = rgb2gray(im2);
figure, imshow(im2); %original grayscale image
%% grayscale image after background removal
se = strel('disk', 20);
im3 = im2 - imopen(im2, se);
figure, imshow(im3);
colormap(jet);
colorbar

%% black-white image
im4 = im2bw(im3, 0.1);
figure, imshow(im4);
```

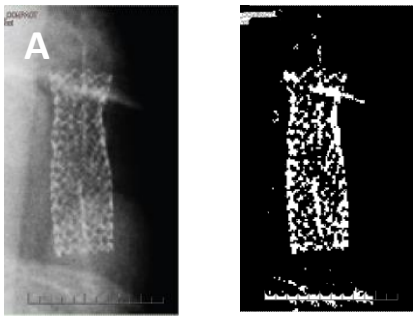

Figure D.1: (A) X-ray snapshots of two X-BP microsensors attached at the both ends of a stent. (B) Post image processing of image A using Morphological Reconstruction in Matlab to remove the background noise and obtain true image of stent and X-BP

BIBLIOGRAPHY

BIBLIOGRAPHY

[1] J. Stokes, "Classic.Ars: Understanding Moore's Law | Ars Technica." [Online]. Available: http://arstechnica.com/gadgets/2008/09/moore/. [Accessed: 13-Nov-2014].

[2] S. A. Vittorio, "MicroElectroMechanical Systems (MEMS)." [Online]. Available: http://www.nytimes.com/2006/06/07/technology/circuits/07essay.html. [Accessed: 13-Nov-2014].

[3] K. E. Petersen, "Silicon as a mechanical material," *Proc. IEEE*, vol. 70, no. 5, pp. 420–457, 1982.

[4] D. Qin, Y. Xia, J. A. Rogers, R. J. Jackman, and G. M. Whitesides, *Part: Microfabrication , Microstructures and Microsystems*, vol. 194. Springer-Verlag Berlin Heidelberg, New York Library, 1998, p. 20.

[5] V. Kaajakari, *Practical MEMS: Design of microsystems, accelerometers, gyroscopes, RF MEMS, optical MEMS, and microfluidic systems: Ville Kaajakari: 9780982299104: Amazon.com: Books*. Small Gear Publishing, 2009, p. 455.

[6] R.C.Anderson, A. van den Berg, J.Cheng, C.S.Effenhauser, W. Ehrfeld, G. Fuhr, V.Hessel, R. J. Jackman, L. J. K. G. Jobst, T.S.J.Lammerink, H. Lehr, R. J. Lipshutz, G.McGall, J.-U.Meyer, D. Qin, J.A.Rogers, S. G. Shirley, S. Shoji, T. Stieglitz, G.A.Urban, G.M.Whitesides, P.Wilding, Y.Xia, and X.-M. Zhao, *Microsystem Technology in Chemistry and Life Sciences*. Springer-Verlag Berlin Heidelberg, New York Library, 1998, p. 262.

[7] G. Lambertus, A. Elstro, K. Sensenig, J. Potkay, M. Agah, S. Scheuering, K. Wise, F. Dorman, R. Sacks, J. College, and B. Circle, "Design , Fabrication , and Evaluation of Microfabricated Columns for Gas Chromatography," vol. 76, no. 9, pp. 2629–2637, 2004.

[8] N. A. Lacher, K. E. Garrison, R. S. Martin, and S. M. Lunte, "Review Microchip capillary electrophoresis / electrochemistry," *Electrophoresis*, vol. 22, no. 12, pp. 2526–2536, 2001.

[9] J. Tian, H. Gong, N. Sheng, X. Zhou, E. Gulari, X. Gao, and G. Church, "Accurate multiplex gene synthesis from programmable DNA microchips," *Nature*, vol. 432, no. 23/30 December, pp. 1050–1053, 2004.

[10] S. Shiohara, Y. Ukita, H. Ushijima, Y. Fukumura, T. Takamura, and Y. Takamura, "RAPID ASSAY SYSTEM FOR INSULIN AND GLUCOSE IN WHOLE BLOOD BY USING A FULL AUTOMATED POSTAGE-STAMP-SIZE CHIP : POSSIBLE APPLICATION FOR A REALTIME FITNESS INDEX IN PEOPLE WITH METABOLIC," pp. 1372–1374, 2012.

[11] C. D. Chin, V. Linder, and S. K. Sia, "Commercialization of microfluidic point-of-care diagnostic devices.," *Lab Chip*, vol. 12, no. 12, pp. 2118–34, Jun. 2012.

[12] S. Lindström and H. Andersson-Svahn, "Overview of single-cell analyses: microdevices and applications.," *Lab Chip*, vol. 10, no. 24, pp. 3363–72, Dec. 2010.

[13] N. Chronis, M. Zimmer, and C. I. Bargmann, "Microfluidics for in vivo imaging of neuronal and behavioral activity in Caenorhabditis elegans.," *Nat. Methods*, vol. 4, no. 9, pp. 727–31, Sep. 2007.

[14] C. D. Chin, S. Y. Chin, T. Laksanasopin, and S. K. Sia, "Point-of-Care Diagnostics on a Chip," pp. 3–22, 2013.

[15] P. Yager, G. J. Domingo, and J. Gerdes, "Point-of-care diagnostics for global health.," *Annu. Rev. Biomed. Eng.*, vol. 10, pp. 107–44, Jan. 2008.

[16] M. Toner and D. Irimia, "Blood-on-a-chip.," *Annu. Rev. Biomed. Eng.*, vol. 7, pp. 77–103, Jan. 2005.

[17] A. Sekizawa, T. Kondo, M. Iwasaki, A. Watanabe, M. Jimbo, H. Saito, and T. Okai, "Accuracy of Fetal Gender Determination by Analysis of DNA in Maternal Plasma," *Clin. C*, vol. 10, pp. 1856–1858, 2001.

[18] F. B. Myers and L. P. Lee, "Innovations in optical microfluidic technologies for point-of-care diagnostics.," *Lab Chip*, vol. 8, no. 12, pp. 2015–31, Dec. 2008.

[19] A. W. Martinez, S. T. Phillips, G. M. Whitesides, and E. Carrilho, "Diagnostics for the developing world: microfluidic paper-based analytical devices.," *Anal. Chem.*, vol. 82, no. 1, pp. 3–10, Jan. 2010.

[20] Y. Zhao, Z. S. Stratton, F. Guo, M. I. Lapsley, C. Y. Chan, S.-C. S. Lin, and T. J. Huang, "Optofluidic imaging: now and beyond.," *Lab Chip*, vol. 13, no. 1, pp. 17–24, Jan. 2013.

[21] Y. Zhao, Z. S. Stratton, F. Guo, M. I. Lapsley, C. Y. Chan, S.-C. S. Lin, and T. J. Huang, "Optofluidic imaging: now and beyond.," *Lab Chip*, vol. 13, no. 1, pp. 17–24, Jan. 2013.

[22] Z. D. Popovic, R. A. Sprague, and G. A. N. Connell, "Technique for monolithic fabrication of microlens arrays," *Appl. Opt.*, vol. 27, no. 7, p. 1281, Apr. 1988.

[23] A. Orth and K. Crozier, “Microscopy with microlens arrays: high throughput, high resolution and light-field imaging.,” *Opt. Express*, vol. 20, no. 12, pp. 13522–31, Jun. 2012.

[24] A. Tripathi and N. Chronis, “A doublet microlens array for imaging micron-sized objects.,” *J. Micromech. Microeng.*, vol. 21, no. 10, Sep. 2011.

[25] L. Yu, B. J. Kim, and E. Meng, “Chronically implanted pressure sensors: challenges and state of the field.,” *Sensors (Basel).*, vol. 14, no. 11, pp. 20620–44, Jan. 2014.

[26] A. M. J. Amy C. Richards Grayson, Rebecca Scheidt Shawgo, N. T. Flynn, Y. Li, M. J. Cima, and R. S. Langer, “A BioMEMS Review: MEMS Technology for Physiologically Integrated Devices,” *Proc. IEEE*, vol. 92, no. 1, pp. 6–21, Jan. 2004.

[27] C. Hierold, B. Clasbrumme, D. Behrend, T. Scheiter, M. Steger, K. Oppermann, H. Kapels, E. Landgra, D. Wenze, and D. Etzrodt, “Implantable Low Power Integrated Pressure Sensor For Minimal Invasive Telemetric Patient Monitoring,” *Proc. 11th Annu. Int. Work. Micro Electro Mech. Syst.*, pp. 568–573, 1998.

[28] J. A. Potkay, “Long term, implantable blood pressure monitoring systems.,” *Biomed. Microdevices*, vol. 10, no. 3, pp. 379–92, Jun. 2008.

[29] A. D. DeHennis and K. D. Wise, “A Fully Integrated Multisite Pressure Sensor for Wireless Arterial Flow Characterization,” *J. Microelectromechanical Syst.*, vol. 15, no. 3, pp. 678–685, Jun. 2006.

[30] E. Cibula and D. Donlagić, “Miniature fiber-optic pressure sensor with a polymer diaphragm.,” *Appl. Opt.*, vol. 44, no. 14, pp. 2736–44, May 2005.

[31] E. Y. Chow, A. L. Chlebowski, S. Chakraborty, W. J. Chappell, and P. P. Irazoqui, “Fully wireless implantable cardiovascular pressure monitor integrated with a medical stent.,” *IEEE Trans. Biomed. Eng.*, vol. 57, no. 6, pp. 1487–96, Jun. 2010.

[32] W. T. Abraham, P. B. Adamson, R. C. Bourge, M. F. Aaron, M. R. Costanzo, L. W. Stevenson, W. Strickland, S. Neelagaru, N. Raval, S. Krueger, S. Weiner, D. Shavelle, B. Jeffries, and J. S. Yadav, “Wireless pulmonary artery haemodynamic monitoring in chronic heart failure: a randomised controlled trial.,” *Lancet*, vol. 377, no. 9766, pp. 658–66, Feb. 2011.

[33] M. Ghannad-Rezaie, M. N. Gulari, R. D. M. Franco, S. I. Mian, and N. Chronis, “A powerless optical microsensor for monitoring intraocular pressure with keratoprostheses,” *2013 Transducers Eurosensors XXVII 17th Int. Conf. Solid-State Sensors, Actuators Microsystems (TRANSDUCERS EUROSENSORS XXVII)*, no. June, pp. 2708–2711, 2013.

[34] R. M. Haque and K. D. Wise, “A 3D Implantable Microsystem for Intraocular Pressure Monitoring using a Glass-In-Silicon Reflow Process,” *Micro Electro Mech. Syst. (MEMS), 2011 IEEE 24th Int. Conf.*, pp. 995–998, 2011.

[35] G. Chen, H. Ghaed, R. Haque, M. Wieckowski, Y. Kim, G. Kim, D. Fick, D. Kim, M. Seok, K. Wise, D. Blaauw, and D. Sylvester, “17.6 A Cubic-Millimeter Energy-Autonomous Wireless Intraocular Pressure Monitor,” *Proc. IEEE Int. Solid-State Circuits Conf.*, pp. 138–139, 2011.

[36] M. Ghannad-Rezaie, L. J.-S. Yang, H. J. L. Garton, and N. Chronis, “A Near-Infrared Optomechanical Intracranial Pressure Microsensor,” *J. Microelectromechanical Syst.*, vol. 21, no. 1, pp. 23–33, Feb. 2012.

[37] S. B. Johansson, A. Eklund, J. Malm, G. Stemme, and N. Roxhed, “A MEMS-based passive hydrocephalus shunt for body position controlled intracranial pressure regulation.,” *Biomed. Microdevices*, vol. 16, no. 4, pp. 529–36, Aug. 2014.

[38] W. Rosamond, K. Flegal, G. Friday, K. Furie, A. Go, K. Greenlund, N. Haase, M. Ho, V. Howard, B. Kissela, B. Kissela, S. Kittner, D. Lloyd-Jones, M. McDermott, J. Meigs, C. Moy, G. Nichol, C. J. O’Donnell, V. Roger, J. Rumsfeld, P. Sorlie, J. Steinberger, T. Thom, S. Wasserthiel-Smoller, and Y. Hong, *Heart disease and stroke statistics--2007 update: a report from the American Heart Association Statistics Committee and Stroke Statistics Subcommittee.*, vol. 115, no. 5. 2007, pp. e69–171.

[39] G. Dangas, “Restenosis: Repeat Narrowing of a Coronary Artery: Prevention and Treatment,” *Circulation*, vol. 105, no. 22, pp. 2586–2587, Jun. 2002.

[40] A. Caixeta, M. B. Leon, A. J. Lansky, E. Nikolsky, J. Aoki, J. W. Moses, J. Schofer, M.-C. Morice, E. Schampaert, A. J. Kirtane, J. J. Popma, H. Parise, M. Fahy, and R. Mehran, “5-Year Clinical Outcomes After Sirolimus-Eluting Stent Implantation Insights From a Patient-Level Pooled Analysis of 4 Randomized Trials Comparing Sirolimus-Eluting Stents With Bare-Metal Stents.,” *J. Am. Coll. Cardiol.*, vol. 54, no. 10, pp. 894–902, Sep. 2009.

[41] H. Staff, “Coronary Stent,” 2014. [Online]. Available: http://www.webmd.com/heart-disease/coronary-stent. [Accessed: 13-Dec-2014].

[42] N. H. Pijls, B. De Bruyne, K. Peels, P. H. Van Der Voort, H. J. Bonnier, J. J. Bartunek J Koolen, and J. J. Koolen, “Measurement of fractional flow reserve to assess the functional severity of coronary-artery stenoses.,” *N. Engl. J. Med.*, vol. 334, no. 26, pp. 1703–8, Jun. 1996.

[43] M. G. Allen, “Micromachined endovascularly-implantable wireless aneurysm pressure sensors: from concept to clinic,” in *The 13th International Conference on Solid-State*

Sensors, Actuators and Microsystems, 2005. Digest of Technical Papers. TRANSDUCERS '05., 2005, vol. 1, pp. 275–278.

[44] "Welcome to CardioMEMS." [Online]. Available: http://www.cardiomems.com/.

[45] "Issys Home." [Online]. Available: http://www.mems-issys.com/.

[46] D. N. Ku, "Blood Flow in Arteries," *Annu. Rev. Fluid Mech.*, vol. 29, no. 1, pp. 399–434, Jan. 1997.

[47] D. Wu, A. Sherwood, J. R. Fromm, S. S. Winter, K. P. Dunsmore, M. L. Loh, H. a Greisman, D. E. Sabath, B. L. Wood, and H. Robins, "High-throughput sequencing detects minimal residual disease in acute T lymphoblastic leukemia.," *Sci. Transl. Med.*, vol. 4, no. 134, p. 134ra63, May 2012.

[48] M. T. Glynn, D. J. Kinahan, and J. Ducrée, "CD4 counting technologies for HIV therapy monitoring in resource-poor settings--state-of-the-art and emerging microtechnologies.," *Lab Chip*, vol. 13, no. 14, pp. 2731–48, Jul. 2013.

[49] L. Bonetta, "Flow cytometry smaller and better," *Nat. Methods*, vol. 2, no. 10, pp. 785–795, 2005.

[50] B. Biosciences, "BD Flow Cytometry," 2008.

[51] W. a. Bonner, "Fluorescence Activated Cell Sorting," *Rev. Sci. Instrum.*, vol. 43, no. 3, p. 404, 1972.

[52] S. Sabban, "Development of an in vitro model system for studying the interaction of Equus caballus IgE with its high- affinity Fc ε RI receptor By Sari Sabban," 1988.

[53] M. Brown and C. Wittwer, "Flow cytometry: principles and clinical applications in hematology.," *Clin. Chem.*, vol. 46, no. 8 Pt 2, pp. 1221–9, Aug. 2000.

[54] The IsoRaft System, "Cell Microsystems." [Online]. Available: http://www.cellmicrosystems.com/. [Accessed: 18-Dec-2014].

[55] G. Medoro, S. Gross, N. Manaresi, M. Sergio, F. Fontana, S. Gianni, A. Calanca, E. Peruzzi, M. Banzi, G. Signorini, C. Rao, J. Patel, J. Karkera, G. Giorgini, M. Mata, and M. C. Connelly, "Use of the DEPArray platform to detect , isolate , and molecularly characterize pure tumor cells from peripheral blood samples enriched using the CellSearch system," *Clin Oncol*, vol. 29, no. June, 2011.

[56] "Miltenyi Biotec - Biomedical instruments, reagents, and services." [Online]. Available: http://www.miltenyibiotec.com/en/. [Accessed: 18-Dec-2014].

[57] T. Ito, H. Fujita, T. Tani, and N. Ohte, “Fractional flow reserve-guided endovascular therapy for common iliac artery stenosis; a comparison with the exercise ankle brachial index: A case report,” *IJC Hear. Vessel.*, vol. 4, pp. 208–210, Sep. 2014.

[58] T. Misaka, H. Kunii, H. Mizukami, N. Sakamoto, K. Nakazato, and Y. Takeishi, “Long-term clinical outcomes after deferral of percutaneous coronary intervention of intermediate coronary stenoses based on coronary pressure-derived fractional flow reserve.,” *J. Cardiol.*, vol. 58, no. 1, pp. 32–7, Jul. 2011.

[59] E. A. Magnuson, M. E. Farkouh, V. Fuster, K. Wang, K. Vilain, H. Li, J. Appelwick, V. Muratov, L. A. Sleeper, R. Boineau, M. Abdallah, and D. J. Cohen, “Cost-Effectiveness of Percutaneous Coronary Intervention With Drug Eluting Stents Versus Bypass Surgery for Patients With Diabetes Mellitus and Multivessel Coronary Artery Disease.”

[60] D. Mabey, R. W. Peeling, A. Ustianowski, and M. D. Perkins, “Diagnostics for the developing world.,” *Nat. Rev. Microbiol.*, vol. 2, no. 3, pp. 231–40, Mar. 2004.

[61] X. Mao and T. J. Huang, “Microfluidic diagnostics for the developing world.,” *Lab Chip*, vol. 12, no. 8, pp. 1412–6, Apr. 2012.

[62] B. Kuswandi, Nuriman, J. Huskens, and W. Verboom, “Optical sensing systems for microfluidic devices: a review.,” *Anal. Chim. Acta*, vol. 601, no. 2, pp. 141–55, Oct. 2007.

[63] T. Krupenkin, S. Yang, and P. Mach, “Tunable liquid microlens,” *Appl. Phys. Lett.*, vol. 82, no. 3, p. 316, 2003.

[64] V. J. Cadarso, A. Llobera, G. Villanueva, C. Dominguez, and J. A. Plaza, “3-D modulable PDMS-based microlens system.,” *Opt. Express*, vol. 16, pp. 4918–4929, 2008.

[65] L. Dong, A. K. Agarwal, D. J. Beebe, and H. Jiang, “Adaptive liquid microlenses activated by stimuli-responsive hydrogels.,” *Nature*, vol. 442, no. 7102, pp. 551–4, Aug. 2006.

[66] J. Chen, W. Wang, J. Fang, and K. Varahramyan, “Variable-focusing microlens with microfluidic chip,” *J. Micromechanics Microengineering*, vol. 14, no. 5, pp. 675–680, May 2004.

[67] N. Chronis, G. Liu, K.-H. Jeong, and L. Lee, “Tunable liquid-filled microlens array integrated with microfluidic network.,” *Opt. Express*, vol. 11, no. 19, pp. 2370–8, Sep. 2003.

[68] M. He, X.-C. Yuan, N. Ngo, J. Bu, and S. Tao, “Low-cost and efficient coupling technique using reflowed sol-gel microlens.,” *Opt. Express*, vol. 11, no. 14, pp. 1621–7, Jul. 2003.

[69] P. Nussbaum, R. Volkrl, H. P. Herzig, M. Eisner, and S. Haselbeck, “Design , fabrication and testing of microlens arrays for sensors and microsystems,” *Pure Appl. Opt.*, vol. 6, pp. 617–636, 1996.

[70] S. L. Aristizabal, G. A. Cirino, A. N. Montagnoli, A. A. Sobrinho, J. B. Rubert, M. Hospital, and R. D. Mansano, “Microlens array fabricated by a low-cost grayscale lithography maskless system,” *Opt. Eng.*, vol. 52, no. 12, pp. 125101–1 – 125101–8, Dec. 2013.

[71] P. Kozma, a Lehmann, K. Wunderlich, D. Michel, S. Schumacher, E. Ehrentreich-Förster, and F. F. Bier, “A novel handheld fluorescent microarray reader for point-of-care diagnostic.,” *Biosens. Bioelectron.*, vol. 47, pp. 415–20, Sep. 2013.

[72] J. Y. Kim, K. Pfeiffer, A. Voigt, G. Gruetzner, and J. Brugger, “Directly fabricated multi-scale microlens arrays on a hydrophobic flat surface by a simple ink-jet printing technique,” *J. Mater. Chem.*, vol. 22, no. 7, p. 3053, 2012.

[73] R. Volkel, H. P. Herzig, P. Nussbaum, R. Dandliker, and W. B. Hugle, “Microlens array imaging system for photolithography,” *Soc. Photo-Optical Instrum. Eng.*, vol. 35, no. 11, pp. 3323–3330, 1996.

[74] B. Aldalali, A. Kanhere, J. Fernandes, C.-C. Huang, and H. Jiang, “Fabrication of Polydimethylsiloxane Microlenses Utilizing Hydrogel Shrinkage and a Single Molding Step,” *Micromachines*, vol. 5, no. 2, pp. 275–288, May 2014.

[75] M. N. Gulari, A. Tripathi, and N. Chronis, “Microfluidic-based Oil-Immersion Lenses for High Resolution Microscopy,” *Sixt. Int. Conf. Miniaturized Syst. Chem. Life Sci. (μTAS 2012)*, pp. 49–51, 2012.

[76] A. Brückner, J. Duparre, F. Wippermann, R. Leitel, P. Dannberg, and A. Brauer, “Ultra-compact close-up microoptical imaging system,” *Proc. SPIE*, vol. 7786, pp. 77860A–1–77860A–8, 2010.

[77] T. Knieling, M. Shaf, W. Lang, and W. Benecke, “Microlens array production in a microtechnological dry etch and reflow process for display applications,” *J. Eur. Opt. Soc. Rap. Public*, vol. 12007, pp. 1–4, 2012.

[78] A. Tripathi, T. V. Chokshi, and N. Chronis, “A high numerical aperture, polymer-based, planar microlens array,” *Appl. Opt.*, vol. 17, no. 22, p. 19908, 2009.

[79] S. Pang, C. Han, J. Erath, A. Rodriguez, and C. Yang, “Wide field-of-view Talbot grid-based microscopy for multicolor fluorescence imaging,” *Opt. Express*, vol. 21, no. 12, pp. 14555–14565, 2013.

[80] E. Schonbrun, S. S. Gorthi, and D. Schaak, “Microfabricated multiple field of view imaging flow cytometry.,” *Lab Chip*, vol. 12, no. 2, pp. 268–73, Jan. 2012.

[81] X. Cui, L. M. Lee, X. Heng, W. Zhong, P. W. Sternberg, D. Psaltis, and C. Yang, “Lensless high-resolution on-chip optofluidic microscopes for Caenorhabditis elegans and cell imaging.,” *Proc. Natl. Acad. Sci. U. S. A.*, vol. 105, no. 31, pp. 10670–5, Aug. 2008.

[82] J. Wu, G. Zheng, and L. M. Lee, “Optical imaging techniques in microfluidics and their applications,” *Lab Chip*, vol. 12, pp. 3566–3575, 2012.

[83] J. Itatani, J. Levesque, D. Zeidler, H. Niikura, H. Pépin, J. C. Kieffer, P. B. Corkum, and D. M. Villeneuve, “Tomographic imaging of molecular orbitals.,” *Nature*, vol. 432, no. 7019, pp. 867–71, Dec. 2004.

[84] Z. Chen, T. E. Milner, D. Dave, and J. S. Nelson, “Optical Doppler tomographic imaging of fluid flow velocity in highly scattering media.,” *Opt. Lett.*, vol. 22, no. 1, pp. 64–6, Jan. 1997.

[85] D. Lange, C. W. Storment, C. a. Conley, and G. T. a. Kovacs, “A microfluidic shadow imaging system for the study of the nematode Caenorhabditis elegans in space,” *Sensors Actuators B Chem.*, vol. 107, no. 2, pp. 904–914, Jun. 2005.

[86] S. Moon, H. O. Keles, A. Ozcan, A. Khademhosseini, E. Haeggstrom, D. Kuritzkes, and U. Demirci, “Integrating microfluidics and lensless imaging for point-of-care testing.,” *Biosens. Bioelectron.*, vol. 24, no. 11, pp. 3208–14, Jul. 2009.

[87] A. Ozcan and U. Demirci, “Ultra wide-field lens-free monitoring of cells on-chip.,” *Lab Chip*, vol. 8, no. 1, pp. 98–106, Jan. 2008.

[88] U. A. Gurkan, S. Moon, H. Geckil, F. Xu, S. Wang, T. J. Lu, and U. Demirci, “Miniaturized lensless imaging systems for cell and microorganism visualization in point-of-care testing.,” *Biotechnol. J.*, vol. 6, no. 2, pp. 138–49, Feb. 2011.

[89] H. Zhu, S. O. Isikman, O. Mudanyali, A. Greenbaum, and A. Ozcan, “Optical imaging techniques for point-of-care diagnostics.,” *Lab Chip*, Oct. 2012.

[90] X. Heng, D. Erickson, L. R. Baugh, Z. Yaqoob, P. W. Sternberg, D. Psaltis, and C. Yang, “Optofluidic microscopy--a method for implementing a high resolution optical microscope on a chip.,” *Lab Chip*, vol. 6, no. 10, pp. 1274–6, Oct. 2006.

[91] S. A. Lee, G. Zheng, N. Mukherjee, and C. Yang, “On-chip continuous monitoring of motile microorganisms on an ePetri platform.,” *Lab Chip*, vol. 12, no. 13, pp. 2385–90, Jul. 2012.

[92] X. Cui, L. M. Lee, X. Heng, W. Zhong, P. W. Sternberg, D. Psaltis, and C. Yang, "Microscopes for Caenorhabditis elegans and cell imaging," *PNAS*, vol. 105, no. 31, pp. 10670–10675, 2008.

[93] D. Gabor, "A New Microscopic Principle," *Nature*, vol. 161, pp. 777–778, 1948.

[94] G. Zheng, "Chip-scale microscopy imaging.," *J. Biophotonics*, vol. 649, no. 8, pp. 639–649, May 2012.

[95] S. Seo, T.-W. Su, D. K. Tseng, A. Erlinger, and A. Ozcan, "Lensfree holographic imaging for on-chip cytometry and diagnostics.," *Lab Chip*, vol. 9, no. 6, pp. 777–87, Mar. 2009.

[96] O. Mudanyali, D. Tseng, C. Oh, S. O. Isikman, I. Sencan, W. Bishara, C. Oztoprak, S. Seo, B. Khademhosseini, and A. Ozcan, "Compact, light-weight and cost-effective microscope based on lensless incoherent holography for telemedicine applications.," *Lab Chip*, vol. 10, no. 11, pp. 1417–28, Jun. 2010.

[97] O. Mudanyali, S. Dimitrov, U. Sikora, S. Padmanabhan, I. Navruz, and A. Ozcan, "Integrated rapid-diagnostic-test reader platform on a cellphone.," *Lab Chip*, vol. 12, no. 15, pp. 2678–86, Aug. 2012.

[98] D. Tseng, O. Mudanyali, C. Oztoprak, S. O. Isikman, I. Sencan, O. Yaglidere, and A. Ozcan, "Lensfree microscopy on a cellphone.," *Lab Chip*, vol. 10, no. 14, pp. 1787–92, Jul. 2010.

[99] P. Allier and A. Ozcan, "Wide-field optical detection of nanoparticles using on-chip microscopy and self-assembled nanolenses," *Nat. Photonics*, vol. 7, no. March, pp. 247–254, 2013.

[100] D. N. Breslauer, R. N. Maamari, N. a Switz, W. a Lam, and D. a Fletcher, "Mobile phone based clinical microscopy for global health applications.," *PLoS One*, vol. 4, no. 7, p. e6320, Jan. 2009.

[101] K. K. Ghosh, L. D. Burns, E. D. Cocker, A. Nimmerjahn, Y. Ziv, A. El Gamal, and M. J. Schnitzer, "miniaturized integration of a fluorescence microscope," *Nat. Methods*, vol. 8, no. 10, 2011.

[102] "Inscopix." [Online]. Available: http://www.inscopix.com/. [Accessed: 06-Nov-2014].

[103] H. Zhu, U. Sikora, and A. Ozcan, "Quantum dot enabled detection of Escherichia coli using a cell-phone.," *Analyst*, vol. 137, no. 11, pp. 2541–4, Jul. 2012.

[104] H. Zhu, O. Yaglidere, T.-W. Su, D. Tseng, and A. Ozcan, "Cost-effective and compact wide-field fluorescent imaging on a cell-phone.," *Lab Chip*, vol. 11, no. 2, pp. 315–22, Jan. 2011.

[105] H. Zhu, I. Sencan, J. Wong, S. Dimitrov, D. Tseng, K. Nagashima, and A. Ozcan, "Cost-effective and rapid blood analysis on a cell-phone.," *Lab Chip*, vol. 13, no. 7, pp. 1282–8, Apr. 2013.

[106] S. A. Lee, R. Leitao, G. Zheng, S. Yang, A. Rodriguez, and C. Yang, "Color capable sub-pixel resolving optofluidic microscope and its application to blood cell imaging for malaria diagnosis.," *PLoS One*, vol. 6, no. 10, p. e26127, Jan. 2011.

[107] L. M. Lee, X. Cui, and C. Yang, "The application of on-chip optofluidic microscopy for imaging Giardia lamblia trophozoites and cysts.," *Biomed. Microdevices*, vol. 11, no. 5, pp. 951–8, Oct. 2009.

[108] "Anurag Tripathi Thesis," University of Michigan, 2012.

[109] M. N. Gulari, A. Tripathi, M. Ghannad-Rezaie, and N. Chronis, "An Optofluidic Lens Array Microchip for High Resolution Stereo Microscopy," *Micromachines*, vol. 5, no. 3, pp. 607–621, Aug. 2014.

[110] J. Kim, K.-H. Jeong, and L. P. Lee, "Artificial ommatidia by self-aligned microlenses and waveguides," *Opt. Lett.*, vol. 30, no. 1, p. 5, 2005.

[111] R. Guo, D. Yuan, and S. Das, "Large-area microlens arrays fabricated on flexible polycarbonate sheets via single-step laser interference ablation," *J. Micromechanics Microengineering*, vol. 21, no. 1, p. 015010, Jan. 2011.

[112] "Microfabricated silicon solid immersion lens," *J. Microelectromech. Syst.*, vol. 10, no. 3, p. 450, 2001.

[113] H. Toshiyoshi, J. LaCosse, and M. C. Wu, "A surface micromachined optical scanner array using photoresist lenses fabricated by a thermal reflow process," *J. Light. Technol.*, vol. 21, no. 7, pp. 1700–1708, Jul. 2003.

[114] X.-C. Yuan, W. X. Yu, M. He, J. Bu, W. C. Cheong, H. B. Niu, and X. Peng, "Soft-lithography-enabled fabrication of large numerical aperture refractive microlens array in hybrid SiO 2 –TiO 2 sol-gel glass," *Appl. Phys. Lett.*, vol. 86, no. 11, p. 114102, 2005.

[115] "micro resist technology GmbH | Products | Hybrid Polymers | ORMOCER®s |." [Online]. Available: http://www.microresist.de/products/ormocers/overview_ormocers_en.htm. [Accessed: 19-Nov-2014].

[116] "Fabrication of spherical microlenses by a combination of isotropic wet etching of silicon and molding techniques," *Opt. Express*, vol. 17, no. 8, p. 6283, 2009.

[117] S. Biehl, R. Danzebrink, P. Oliveira, and M. A. Aegerter, “Refractive microlens fabrication by ink-jet process,” *J. Sol-Gel Sci. Technol.*, vol. 13, no. 1/3, p. 177, 1998.

[118] J. Y. Kim, N. B. Brauer, V. Fakhfouri, D. L. Boiko, E. Charbon, G. Grutzner, and J. Brugger, “Hybrid polymer microlens arrays with high numerical apertures fabricated using simple ink-jet printing technique,” *Opt. Mater. Express*, vol. 1, no. 2, p. 259, 2011.

[119] X. Mao, J. R. Waldeisen, B. K. Juluri, and T. J. Huang, “Hydrodynamically tunable optofluidic cylindrical microlens.,” *Lab Chip*, vol. 7, no. 10, pp. 1303–8, Oct. 2007.

[120] H. Ren, Y.-H. Fan, and S.-T. Wu, “Liquid-crystal microlens arrays using patterned polymer networks.,” *Opt. Lett.*, vol. 29, no. 14, pp. 1608–10, Jul. 2004.

[121] X. Mao, Z. I. Stratton, A. A. Nawaz, S.-C. S. Lin, and T. J. Huang, “Optofluidic tunable microlens by manipulating the liquid meniscus using a flared microfluidic structure.,” *Biomicrofluidics*, vol. 4, no. 4, p. 43007, Jan. 2010.

[122] P. Fei, Z. He, C. Zheng, T. Chen, Y. Men, and Y. Huang, “Discretely tunable optofluidic compound microlenses.,” *Lab Chip*, vol. 11, no. 17, pp. 2835–41, Sep. 2011.

[123] X. Mao, S.-C. S. Lin, M. I. Lapsley, J. Shi, B. K. Juluri, and T. J. Huang, “Tunable Liquid Gradient Refractive Index (L-GRIN) lens with two degrees of freedom.,” *Lab Chip*, vol. 9, no. 14, pp. 2050–8, Jul. 2009.

[124] J. Shi, Z. Stratton, S.-C. S. Lin, H. Huang, and T. J. Huang, “Tunable optofluidic microlens through active pressure control of an air–liquid interface,” *Microfluid. Nanofluidics*, vol. 9, no. 2–3, pp. 313–318, Dec. 2009.

[125] “Arterial Line Placement.” [Online]. Available: http://emedicine.medscape.com/article/1999586-overview. [Accessed: 06-Nov-2014].

[126] K. A. Townsend, J. W. Haslett, T. K. K. Tsang, M. N. El-Gamal, and K. Iniewski, “Recent advances and future trends in low power wireless systems for medical applications,” in *Fifth International Workshop on System-on-Chip for Real-Time Applications (IWSOC’05)*, 2005, pp. 476–481.

[127] J. Krejza, M. Arkuszewski, S. E. Kasner, J. Weigele, A. Ustymowicz, R. W. Hurst, B. L. Cucchiara, and S. R. Messe, “Carotid artery diameter in men and women and the relation to body and neck size.,” *Stroke.*, vol. 37, no. 4, pp. 1103–5, May 2006.

[128] S. J. Frank L. Pedrotti, L. M. Pedrotti, and Leno S. Pedrotti, *Introduction to Optics*. Pearson Education, 2008, p. Oil immersion p. 97, Thick lens p.412.

[129] M. J. Riedl, *Optical Design Fundamentals for Infrared Systems*. SPIE Press, 2001, p. 182.

[130] J. E. Greivenkamp, *Field Guide to Geometrical Optics*. Society of Photo Optical, 2004, p. 117.

[131] S. Bradbury and D. B. Bracegirdle, *Introduction To Light Microscopy*. BIOS Scientific Publishers Limited, 1998, p. 123.

[132] F. R. Spellman, *Microbiology for Water and Wastewater Operators (Revised Reprint)*. CRC Press, 1999, p. Chapter 2 Microscope.

[133] G. A. Peyman, J. E. Koziol, W. I. Fried, and D. R. Sanders, "Operating microscope with two pairs of stereo eye-piece lenses," 06-Feb-1979.

[134] O. Muller, K. Biber, H. Jakubowski, and G. Hanemann, "Operation microscope," 15-May-1984.

[135] T. Fukaya, M. Hamada, S. Nakamura, T. Hanzawa, M. Kinukawa, T. Ishikawa, H. Fujiwara, and S. Tokunaga, "Stereomicroscope," 03-Sep-1996.

[136] L. Woolnough, "Starting with stereomicroscopes – Quekett Microscopical Club." [Online]. Available: http://www.quekett.org/starting/stereo-microscopes/stereo-microscopes. [Accessed: 08-May-2014].

[137] "Conversation with William Solinski - Microscopy Sales Representative Olympus Scientific Solutions Americas- Stereo Microscopes SZ61." .

[138] "Nikon MicroscopyU | Concepts and Formulas | Resolution." [Online]. Available: http://www.microscopyu.com/articles/formulas/formulasresolution.html. [Accessed: 22-May-2014].

[139] H. W. Hubers, J. Schubert, A. Krabbe, M. Birk, G. Wagner, A. Semenov, G. Goltsman, B. Voronov, and E. Gershenzon, "Parylene anti-reflection coating of a quasi-optical hot-electron- bolometric mixer at terahertz frequencies," *Infrared Phys. Technol.*, vol. 42, pp. 41–47, 2001.

[140] V. R. Horowitz, D. D. Awschalom, and S. Pennathur, "Optofluidics: field or technique?," *Lab Chip*, vol. 8, no. 11, pp. 1856–63, Nov. 2008.

[141] Y. Zhao, Z. S. Stratton, F. Guo, M. I. Lapsley, C. Y. Chan, S.-C. S. Lin, and T. J. Huang, "Optofluidic imaging: now and beyond.," *Lab Chip*, vol. 13, no. 1, pp. 17–24, Jan. 2013.

[142] W. Bishara, S. Isikman, H. Zhu, A. Ozcan, and L. Angeles, "OPTO-FLUIDIC TOMOGRAPHY," pp. 1986–1988, 2011.

[143] X. Zhang, I. Khimji, U. A. Gurkan, H. Safaee, P. N. Catalano, H. O. Keles, E. Kayaalp, and U. Demirci, "Lensless imaging for simultaneous microfluidic sperm monitoring and sorting.," *Lab Chip*, vol. 11, no. 15, pp. 2535–40, Aug. 2011.

[144] X. Heng, D. Erickson, L. R. Baugh, Z. Yaqoob, P. W. Sternberg, D. Psaltis, and C. Yang, "Optofluidic microscopy--a method for implementing a high resolution optical microscope on a chip.," *Lab Chip*, vol. 6, no. 10, pp. 1274–6, Oct. 2006.

[145] Z. Göröcs, A. Ozcan, and S. Member, "On-Chip Biomedical Imaging," vol. 6, pp. 29–46, 2013.

[146] S. Pang, X. Cui, J. DeModena, Y. M. Wang, P. Sternberg, and C. Yang, "Implementation of a color-capable optofluidic microscope on a RGB CMOS color sensor chip substrate.," *Lab Chip*, vol. 10, no. 4, pp. 411–4, Feb. 2010.

[147] M. N. Gulari, N. Chronis, and M. Ghannad-rezaie, "A compact, Optofluidic Microsystem for Measuring Red Blood Cell Concentration," *Solid-State Sensors, Actuators Microsystems (TRANSDUCERS EUROSENSORS XXVII), 2013 Transducers Eurosensors XXVII 17th Int. Conf.*, no. June, pp. 2552–2555, 2013.

[148] M. C. Phelan1 and G. Lawler, "Cell Counting - Current Protocols," *Curr. Protoc. Cytom.*, 2001.

[149] "Spatial Resolution." [Online]. Available: http://oftankonyv.reak.bme.hu/tiki-index.php?page=Spatial+Resolution. [Accessed: 11-Nov-2014].

[150] P. Grieshaber, W. A. Lagrèze, C. Noack, D. Boehringer, and J. Biermann, "Staining of fluorogold-prelabeled retinal ganglion cells with calcein-AM: A new method for assessing cell vitality.," *J. Neurosci. Methods*, vol. 192, no. 2, pp. 233–9, Oct. 2010.

[151] P. A. Heidenreich, J. G. Trogdon, O. A. Khavjou, J. Butler, K. Dracup, M. D. Ezekowitz, E. A. Finkelstein, Y. Hong, S. C. Johnston, A. Khera, D. M. Lloyd-Jones, S. A. Nelson, G. Nichol, D. Orenstein, P. W. F. Wilson, and Y. J. Woo, "Forecasting the future of cardiovascular disease in the United States: a policy statement from the American Heart Association.," *Circulation*, vol. 123, no. 8, pp. 933–44, Mar. 2011.

[152] V. L. Roger, A. S. Go, D. M. Lloyd-Jones, E. J. Benjamin, J. D. Berry, W. B. Borden, D. M. Bravata, S. Dai, E. S. Ford, C. S. Fox, H. J. Fullerton, C. Gillespie, S. M. Hailpern, J. A. Heit, V. J. Howard, B. M. Kissela, S. J. Kittner, D. T. Lackland, J. H. Lichtman, L. D. Lisabeth, D. M. Makuc, G. M. Marcus, A. Marelli, D. B. Matchar, C. S. Moy, D. Mozaffarian, M. E. Mussolino, G. Nichol, N. P. Paynter, E. Z. Soliman, P. D. Sorlie, N. Sotoodehnia, T. N. Turan, S. S. Virani, N. D. Wong, D. Woo, and M. B. Turner, "Heart disease and stroke statistics--2012 update: a report from the American Heart Association.," *Circulation*, vol. 125, no. 1, pp. e2–e220, Jan. 2012.

[153] L. Lilly, *Pathophysiology of Heart disease: A Collaborative Project of Medical Students and Faculty. 5*. Lippincott Williams & Wilkins, 2011, p. 461.

[154] N. H. J. Pijls, P. van Schaardenburgh, G. Manoharan, E. Boersma, J.-W. Bech, M. van't Veer, F. Bär, J. Hoorntje, J. Koolen, W. Wijns, and B. de Bruyne, "Percutaneous coronary intervention of functionally nonsignificant stenosis: 5-year follow-up of the DEFER Study.," *J. Am. Coll. Cardiol.*, vol. 49, no. 21, pp. 2105–11, May 2007.

[155] D. Alexopoulos, I. Xanthopoulou, P. Davlouros, A. Damelou, A. Mazarakis, J. Chiladakis, and G. Hahalis, "Mechanisms of nonfatal acute myocardial infarction late after stent implantation: the relative impact of disease progression, stent restenosis, and stent thrombosis.," *Am. Heart J.*, vol. 159, no. 3, pp. 439–45, Mar. 2010.

[156] M.-C. Morice, P. W. Serruys, P. Barragan, C. Bode, G.-A. Van Es, H.-P. Stoll, D. Snead, L. Mauri, D. E. Cutlip, and E. Sousa, "Long-term clinical outcomes with sirolimus-eluting coronary stents: five-year results of the RAVEL trial.," *J. Am. Coll. Cardiol.*, vol. 50, no. 14, pp. 1299–304, Oct. 2007.

[157] C. Briguori, C. Sarais, P. Pagnotta, F. Liistro, M. Montorfano, A. Chieffo, F. Sgura, N. Corvaja, R. Albiero, G. Stankovic, C. Toutoutzas, E. Bonizzoni, C. Di Mario, and A. Colombo, "In-stent restenosis in small coronary arteries: impact of strut thickness.," *J. Am. Coll. Cardiol.*, vol. 40, no. 3, pp. 403–9, Aug. 2002.

[158] A. A. Bavry, D. J. Kumbhani, T. J. Helton, P. P. Borek, G. R. Mood, and D. L. Bhatt, "Late thrombosis of drug-eluting stents: a meta-analysis of randomized clinical trials.," *Am. J. Med.*, vol. 119, no. 12, pp. 1056–61, Dec. 2006.

[159] S. G. Ellis, G. W. Stone, D. a Cox, J. Hermiller, C. O'Shaughnessy, T. Mann, M. Turco, R. Caputo, P. J. Bergin, T. S. Bowman, and D. S. Baim, "Long-term safety and efficacy with paclitaxel-eluting stents: 5-year final results of the TAXUS IV clinical trial (TAXUS IV-SR: Treatment of De Novo Coronary Disease Using a Single Paclitaxel-Eluting Stent).," *JACC. Cardiovasc. Interv.*, vol. 2, no. 12, pp. 1248–59, Dec. 2009.

[160] J. G. Chubbuck and Melvin H. Epstein, "X-ray readable implantable pressure sensor," 09-Dec-1986.

[161] F. R. de Graaf, J. D. Schuijf, J. E. van Velzen, M. J. Boogers, L. J. Kroft, A. de Roos, J. H. C. Reiber, A. Sieders, F. Spanó, J. W. Jukema, M. J. Schalij, E. E. van der Wall, and J. J. Bax, "Diagnostic accuracy of 320-row multidetector computed tomography coronary angiography to noninvasively assess in-stent restenosis.," *Invest. Radiol.*, vol. 45, no. 6, pp. 331–40, Jun. 2010.

[162] J. Piek and P. Raes, "Pressure-controlled drainage of cerebrospinal fluid: clinical experience with a new type of ventricular catheter (Ventcontrol MTC) and an integrated piezo-resistive," *Neurosurgery*, 1996.

[163] B. Bae, B. R. Flachsbart, K. Park, and M. A. Shannon, “Design optimization of a piezoresistive pressure sensor considering the output signal-to-noise ratio,” *J. Micromechanics Microengineering*, vol. 14, no. 12, pp. 1597–1607, Dec. 2004.

[164] K. W. Hsiung, J. Hynecek, and S. F. Boettcher, “Development of a Miniature Pressure Transducer for BiomediclaI Applications,” *J. Micromech. Microeng.*, vol. ED-26, no. 12, pp. 1896–1905, 1979.

[165] M. Tanimotol, F. Arail, T. Fukuda, H. Iwata, K. Itoigawa, Y. G. M. Hashimoto, and M. Negoro, “Micro force sensor for intravascular neurosurgery and in vivo experiment,” *Proc. 11th Annu. Int. Work. Micro Electro Mech. Syst.*, pp. 504–509, 1998.

[166] C. S. Sander, J. W. Knutti, and J. D. Meindl, “A monolithic capacitive pressure sensor with pulse-period output,” *IEEE Trans. Electron Devices*, vol. 27, no. 5, pp. 927–930, May 1980.

[167] M. G. Allen, “Microfabricated implantable wireless microsystems: Permanent and biodegradable implementations,” *Micro Electro Mech. Syst. (MEMS), 2014 IEEE 27th Int. Conf.*, pp. 3–6, 2014.

[168] R. Schlierf, M. Gortz, T. S. Rode, W. Mokwa, U. Schnakenberg, and K. Trieu, “Pressure sensor capsule to control the treatmnent of abdominal aorta aneurisms,” in *The 13th International Conference on Solid-State Sensors, Actuators and Microsystems, 2005. Digest of Technical Papers. TRANSDUCERS ’05.*, 2005, vol. 2, pp. 1656–1659.

[169] M. Fonseca, “Development of Implantable Wireless Pressure Sensors for Chronic Disease Management,” 2008. [Online]. Available: http://smartech.gatech.edu/handle/1853/21768. [Accessed: 31-Mar-2014].

[170] M. N. Gulari, M. Ghannad-rezaie, P. Novelli, N. Chronis, and T. C. Marentis, “An X-Ray Detectable Pressure Microsensor for Monitoring Coronary In-stent Restenosis,” *Micro Electro Mech. Syst. (MEMS), 2014 IEEE 27th Int. Conf.*, pp. 893–896, 2014.

[171] M. Sadeghi, H. Kim, and K. Najafi, “Electrostatically driven micro-hydraulic actuator arrays,” *2010 IEEE 23rd Int. Conf. Micro Electro Mech. Syst.*, pp. 15–18, Jan. 2010.

[172] M. M. Sadeghi, R. L. Peterson, and K. Najafi, “High-speed electrostatic micro-hydraulics for sensing and actuation,” *2013 IEEE 26th Int. Conf. Micro Electro Mech. Syst.*, pp. 1191–1194, Jan. 2013.

[173] M. M. Sadeghi, R. L. Peterson, and K. Najafi, “A 2-D directional air flow sensor array made using stereolithography and MEMS micro-hydraulic structures,” *2013 Transducers Eurosensors XXVII 17th Int. Conf. Solid-State Sensors, Actuators Microsystems (TRANSDUCERS EUROSENSORS XXVII)*, no. June, pp. 722–725, 2013.

[174] “Lurie Nanofabrication Facility — microfabrication nanofabrication services.” [Online]. Available: http://lnf.umich.edu/. [Accessed: 01-Apr-2014].

[175] A. Macovski, *Medical imaging systems*. Englewood Cliffs N.J.: Prentice-Hall, 1983, p. 256.

[176] O. Tabata, K. Kawahata, S. Susumu, and I. Igarashi, “Mechanical Property Measurements of Thin Films Using Load-Deflection of Composite Rectangular Membranes,” *Sensors and Actuators*, vol. 20, pp. 135–141, 1989.

[177] R. L. Edwards, G. Coles, and W. N. Sharpe, “Comparison of Tensile and Bulge Tests for Thin-Film Silicon Nitride,” *Exp. Mech.*, vol. 44, no. 1, pp. 49–54, Feb. 2004.

[178] B. Merle and M. Göken, “Fracture toughness of silicon nitride thin films of different thicknesses as measured by bulge tests,” *Acta Materialia*, vol. 59, no. 4. pp. 1772–1779, Feb-2011.

[179] J. J. J. Vlassak, W. D. D. Nix, and I. Introduction, “A new bulge test technique for the determination of Young’s modulus and Poisson's ratio of thin films,” *J. Mater. Res.*, vol. 7, no. 12, pp. 3242–3249, Jan. 2011.

[180] “The Bosch Process for Etching Micro-Mechanical Systems (MEMS) - Principles, Advances and Applications by Oxford Instruments Plasma Technology.” [Online]. Available: http://www.azonano.com/article.aspx?ArticleID=2738. [Accessed: 09-Apr-2014].

[181] B. Merle and M. Göken, “Fracture toughness of silicon nitride thin films of different thicknesses as measured by bulge tests,” *Acta Mater.*, vol. 59, no. 4, pp. 1772–1779, Feb. 2011.

[182] A. Kaushik, H. Kahn, and A. H. Heuer, “Wafer-level mechanical characterization of silicon nitride MEMS,” *J. Microelectromechanical Syst.*, vol. 14, no. 2, pp. 359–367, Apr. 2005.

[183] B. Ziaie, J. A. Von Arx, M. R. Dokmeci, and K. Najafi, “A Hermetic Glass-Silicon Micropack h-Density On-Chip Feedthro for Sensors and Actuators,” vol. 5, no. 3, pp. 166–179, 1996.

[184] J. Y. Pan, “Reliability Considerations for the BioMEMS Designer,” *Proc. IEEE*, vol. 92, no. 1, pp. 174–184, Jan. 2004.

[185] R. C. Gonzalez and R. E. Woods, *Digital Image Processing*, vol. 21. Pearson Education, 2011, p. 976.

[186] C. A. Steeves, Y. L. Young, Z. Liu, A. Bapat, K. Bhalerao, A. B. O. Soboyejo, and W. O. Soboyejo, “Membrane thickness design of implantable bio-MEMS sensors for the in-situ monitoring of blood flow.,” *J. Mater. Sci. Mater. Med.*, vol. 18, no. 1, pp. 25–37, Jan. 2007.

[187] D. Kim, S. Park, J. H. Lee, Y. Y. Jeong, and S. Jon, “Antibiofouling polymer-coated gold nanoparticles as a contrast agent for in vivo X-ray computed tomography imaging.,” *J. Am. Chem. Soc.*, vol. 129, no. 24, pp. 7661–5, Jun. 2007.

[188] J. F. Hainfeld, D. N. Slatkin, T. M. Focella, and H. M. Smilowitz, “Gold nanoparticles: a new X-ray contrast agent.,” *Br. J. Radiol.*, vol. 79, no. 939, pp. 248–53, Mar. 2006.

[189] RadiologyInfo.org, “Radiation Dose in X-Ray and CT Exams What are x-rays and what do they do ?,” 2014. [Online]. Available: http://www.radiologyinfo.org/en/pdf/sfty_xray.pdf.

[190] AAPM Science Council, “AAPM Announcements - AAPM Response in Regards to CT Radiation Dose and its Effects,” 2009. [Online]. Available: http://www.aapm.org/publicgeneral/CTDoseResponse.asp. [Accessed: 20-Oct-2014].

[191] J. F. Hainfeld, D. N. Slatkin, T. M. Focella, and H. M. Smilowitz, “Gold nanoparticles: a new X-ray contrast agent.,” *Br. J. Radiol.*, vol. 79, no. 939, pp. 248–53, Mar. 2006.